The Thesis Committee for Benjamin Kurt Weaver Certifies that this is the approved version of the following thesis:

Evaluation of Multilayered Elastostatic Backcalculation using In-situ Measurements in Geosynthetic-reinforced Asphalt Pavement

SUPERVISING COMMITTEE:

Jorge G. Zornberg, Supervisor

Ellen M. Rathje

Evaluation of Multilayered Elastostatic Backcalculation using In-situ Measurements in Geosynthetic-reinforced Asphalt Pavement

by

Benjamin Kurt Weaver

Thesis

Presented to the Faculty of the Graduate School

of The University of Texas at Austin

in Partial Fulfillment

of the Requirements

for the Degree of

Master of Science in Engineering

The University of Texas at Austin
December 2021

Dedication

To My Family

Acknowledgements

I would like to extend my deepest gratitude to Dr. Jorge Zornberg for his indispensable guidance and mentorship, both during this research study and throughout the entirety of my Master's program. I was consistently challenged but was always provided the necessary feedback and support required to overcome those challenges and continue to learn and grow as an Engineer.

I would also like to thank Dr. Ellen Rathje for reviewing this manuscript and sharing her extensive knowledge in the field of geotechnical earthquake engineering and interpretation of geophone data. I am also grateful to all the faculty in the Geotechnical engineering and Transportation engineering departments for the excellent coursework and for creating the best possible learning environment, even through the most difficult of circumstances, including Dr. El Mohtar, Dr. Gilbert, Dr. Kumar, Dr. Stokoe, and Dr. Bhasin.

I also want to acknowledge several others from Dr. Zornberg's research group, including Subu Sankaranarayanan for his immense patience and willingness to work with me on a regular basis and help me learn the basics of coding and signal processing which were necessary for completion of this project, as well as for developing and sharing the Python program with me for forward calculation of theoretical deflections using layered elastic analysis which saved a considerable amount of time in completing this analysis. Additionally, I would like to thank Vinay Kumar for bringing me up to speed on the project background and answering the many questions I had, and each of them for sharing their immense knowledge and experience regarding the interpretation of the data generated as part of this study.

Lastly, I owe my deepest gratitude to my wife, Kristen and daughters, Maeve and Ellie for their unconditional love and support, as well as to my parents, Kurt and Annie, for instilling me with a life-long love of learning, in addition to teaching me the value of persistent hard work and dedication. This would not have been possible without you.

Evaluation of Multilayered Elastostatic Backcalculation using In-situ Measurements in Geosynthetic-reinforced Asphalt Pavement

by

Benjamin Kurt Weaver, M.S.E

The University of Texas at Austin, 2021

SUPERVISOR: Jorge G. Zornberg

Raw output data from geophones embedded in an instrumented pavement section with six different geosynthetic reinforcements used as interlayers in the hot mix asphalt (HMA) were processed to determine deflections occurring at several depths within the pavement under falling weight deflectometer (FWD) testing. This testing took place during loading campaigns that were conducted over the first two years of the rehabilitated pavement design life. The intent of the study was to use these measured deflections to assess the accuracy of elastostatic backcalculation, by comparing predicted deflections occurring within the pavement using backcalculated moduli and layered elastic theory to measured ones under similar loading.

Deflection Basin Parameters (DBPs) obtained from consideration of surface deflections only which included the Surface Curvature Index (SCI), Base Damage Index (BDI), outermost deflection (W7), and spreadability were first used to qualitatively compare the change in performance of the seven test sections over the first two years of rehabilitated pavement life. When deflections were load and temperature normalized, the spreadability decreased while the SCI increased in each section over time, which are both indicative of the start of damage accumulation. The overlays appeared to be performing similarly in each section, except for in Section 7 which seemed to be deteriorating at a more rapid rate. Additionally, the baseline spreadability of the Old HMA and overlay in the control section immediately following rehabilitation was highest but

compared more closely with the spreadability of several of the reinforced sections two years following rehabilitation, which may provide early indication of a possible effect of geosynthetic reinforcement in slowing the degradation of pavement flexural rigidity. Each of these effects should continue to be investigated over the course of the overlay design life through nondestructive testing and and/or routine PCI surveys.

Taking the geophone measured depth deflections into consideration and assessing the agreement between theoretical and in situ depth deflections under FWD loading, it was found that during the first two loading campaigns the overall agreement between the two was acceptable, with 75 percent of all observations having a relative error of less than 9 percent, and with the absolute error occurring within a range of -1.2 to +1.0 mils. This apparent range in absolute error was fairly consistent across all load levels and maximum deflections, which suggests that the error is most likely due to a combination of the signal to noise ratio of the geophones as well as slight imprecision in the location of FWD drops as opposed to being a function of nonlinear behavior of unbound pavement materials. When the effect of anomalous readings during the first loading campaign in Section 3 and second loading campaign in Section 4 were ignored, the presence of a geosynthetic reinforcement in the HMA did not seem to affect the overall accuracy of elastostatic backcalculation, with overall average relative errors per sensor in each section being approximately 4.0 to 6.5 percent. The exception to this was in Section 7, which was also the section that appeared to be deteriorating more quickly than the others and had an average relative error per sensor in excess of 11 percent between the two loading campaigns. However, the average absolute error per sensor increased significantly in all sections over time, with the largest errors observed during the last two loading campaigns included in the analysis. It is unknown if this effect is primarily attributable to degradation of the pavement or to degradation in performance of the instrumentation, since a relatively large number of sensors used in this analysis (19 percent) malfunctioned causing the data to become unusable within the time incorporated in this study. The exact cause of the malfunctioning geophones is still under review but lends to the importance of careful installation techniques and planning for redundancy and possible sensor loss if geophones are to be used to provide in-situ measurements for long-term field monitoring programs. Engineers should be wary of the possibility for non-uniqueness of solution in deflection basin fitting, and if pavement layers need to be combined, they should consist of the materials with as close of a match as possible in engineering properties.

Table of Contents

List of Tables

List of Figures

Chapter 1: Introduction

1.1 Background and Motivation:

With the increased implementation of the Mechanistic- Empirical Design Guide (MEPDG) at state highway agencies throughout the country, the need for accurate characterization of layer properties of existing pavements is more crucial than ever. In the mechanistic-empirical design process, the time, temperature, load (magnitude and frequency), and moisture-dependent layer moduli are used in static layered-elastic analyses to predict the tensile and compressive strains at specific points of interest within pavement sections under expected loading conditions. The strains predicted through such mechanistic analyses are then used to estimate damage to the pavement over a specific design period through empirical models that relate compressive and tensile strains to rutting, top-down, and bottom-up fatigue cracking. Ultimately, new and rehabilitated pavement sections are designed such that the expected damage accumulated over the life of the pavement does not exceed prescribed limits. The success of this method in predicting total accumulated damage over a specific design period is dependent on the accuracy of assumptions made at the time of design regarding the properties of the specific pavement layers (thickness, Poisson's ratio, moduli) and how well static layered elastic theory can predict the behavior of nonlinear pavement materials under a dynamic loading condition.

Falling Weight Deflectometer (FWD) testing is a nondestructive method that is commonly used to characterize the layer moduli and structural condition of existing pavements. FWD devices are typically trailer-mounted and towed behind a pickup truck and generate load pulses by dropping a weight from variable heights that transmits load to a circular plate in contact with the surface of the road. The impact force is measured through a load cell, and an array of sensors (typically velocity transducers) placed at certain radial distances away from the load plate are used to define a "deflection basin," or the depressed shape of the of the pavement surface under the applied loading (Schmalzer, 2006). Even though the loading is dynamic in nature with the peak velocity measured by each sensor occurring at different times, the traditional FWD interpretation assumes the pavement response to be static, with the static deflection basin defined using the maximum deflections obtained by each sensor (Magnuson, 1988; Guzina and Osburn, 2002; Fu et al. 2020). The premise of FWD backcalculation is that if the load, deflection basin, and layer thicknesses are known (with Poisson's ratios assumed), the stiffness of individual pavement layers in the system can be backcalculated through a number of available computational methods.

In the MEPDG, Level 1 analysis is the first of three levels that are differentiated between in the guide for both new pavement construction and rehabilitation design. Level 2 and Level 3 are comparatively less rigorous in terms of the testing procedures used and assumptions made for characterization of the site, construction material properties, traffic, climate, and other factors. FWD backcalculation results can provide direct inputs into mechanistic-empirical design for characterization of hot mix asphalt (HMA) and unbound materials using Level 1 analysis for rehabilitation design according to the process outlined below from NCHRP Project 1-37A (AASHTO, 2004):

HMA Materials:

Step 1: The damaged modulus E_i of the existing HMA is determined for the rehabilitation project by obtaining the mean FWD backcalculated modulus along the outer wheel path of the project area.

Step 2: The volumetric mix parameters of the existing HMA are determined from evaluation of core samples obtained in the field.

Step 3: The modified Witczak equation is used along with data collected in Step 2 to define the undamaged dynamic modulus master curve of the existing HMA.

Step 4: The damage factor, d_j is estimated as $d_j = \frac{E_i}{E^*}$ where E_i is the FWD backcalculated modulus at the pavement temperature and frequency of FWD excitation corresponding to the testing conditions, and E* is the predicted modulus at the same temperature and load frequency obtained from the Witczak equation.

Step 5: Since the Witczak equation defines the dynamic modulus master curve using a sigmoidal model, the fitting coefficient in the numerator of the model, α, is penalized by the damage factor by defining $\alpha' = (1 - d_j)\alpha$.

Step 6: The field damaged master curve is then defined for input into the MEPDG, essentially as a shifted undamaged master curve by using the α' factor in the modified Witczak equation instead of α.

Unbound Materials:

> The resilient modulus, M_r for each unbound layer is either determined in the laboratory through cyclic triaxial testing of collected samples according to the AASHTO T307 method, or through direct backcalculation results from FWD testing.

Based on this discussion, it may be concluded that the data generated from FWD testing can play a significant role in rehabilitation design using the MEPDG. This is because, in Level 1 analysis, FWD testing may be used to define the required material inputs of the dynamic modulus master curve for the HMA layer(s) and the resilient moduli of the base, subbase, and subgrade layers, and since these moduli are then used to directly predict strains – and hence damage – occurring within the pavement section.

The primary aim of this research is to assess the accuracy of FWD elastostatic backcalculation procedure. FWD tests were conducted at a test site located along SH 21 east of Bastrop, TX. The layer moduli at the test locations were determined through traditional static FWD backcalculation involving only surface deflections. The sub-surface deflections within the pavement structure were assessed using layered elastic analysis (LEA) with the moduli backcalculated from the FWD tests. These predicted deflections were then compared to the actual in-situ deflections measured using geophones embedded within the pavement section. Additionally, the pavement temperature, magnitude of force application, presence of a geosynthetic interlayer reinforcement in the HMA, and user input into backcalculation conducted using MODULUS 7.0 (Scullion et al. 1990) were assessed in terms of their impact on the adequacy of theoretical deflections to predict the measured deflection values. This would allow either validating currently adopted assumptions made for input of material parameters into the MEPDG or identifying such assumptions as factors that warrant additional refinement when determining the best approach for characterizing layer properties.

1.2 Thesis Outline:

The following key tasks were used as a roadmap in achieving the desired research objectives: 1) characterization of the rehabilitated pavement test section, 2) determination of in-situ sub-surface deflections under FWD loading using embedded geophones, 3) backcalculation using the MODULUS 7.0 program to determine layer moduli, 4) forward calculation using a Python program developed for layered elastic analysis to determine theoretical sub-surface deflections, 5) comparison of predicted and in-situ measured deflections to assess the accuracy of FWD backcalculation.

This thesis is organized into six chapters. Chapter 1 contains an introduction to FWD input into the MEPDG approach and explains the motivation behind researching the accuracy of the conventional backcalculation approach.

Chapter 2 provides a review of existing literature pertaining to subjects involving measurement of deflections using velocity transducers (geophones), verification of layered elastic theory using instrumented pavement sections, and studies focused on assessing the consistency and accuracy of backcalculation.

Chapter 3 includes a description of the test section at SH 21 and discusses how material collected from pavement cores and auger boring samples were utilized to effectively characterize the pavement profile. This chapter also includes a description of the instrumentation embedded within the pavement section, as well as a description of the Dynatest FWD utilized to generate the data used in the study.

Chapter 4 provides detailed information regarding the data reduction and signal processing techniques that were utilized to determine accurate pavement deflections from the geophones. This included considering the effect of the geophones in attenuating lower frequency components of the FWD excitation. This chapter also contains a description of the MODULUS 7.0 program, and the backcalculation technique employed by that program to obtain layer moduli. This chapter finally describes the procedure for forward calculation using layered elastic theory to determine predicted deflections at points of interest within the pavement section.

Chapter 5 initially provides with a qualitative assessment of test section performance over the first two years after rehabilitation using deflection basin parameters, and then includes a comparative analysis between the deflections predicted through backcalculation and layered elastic theory and the measured deflections obtained using the geophones. The effects of temperature, load magnitude, user input into MODULUS 7.0, and the presence of a geosynthetic layer are evaluated to quantify their effect on the agreement between predicted and measured values.

Finally, Chapter 6 summarizes conclusions that were drawn from the results of this study. The Python codes used in determining geophone deflections as well as backcalculation results are included in the appendices.

Chapter 2: Literature Review

The literature review contained in this chapter aims at providing sufficient context for the subsequent chapters, by first introducing prior studies pertaining to the use of geophones for obtaining deflections, accuracy of backcalculation, and the use of field instrumentation for the verification of layered elastic theory.

2.1 Measurement of Deflections using Geophones:

2.1.1 Response of Geophone

A velocity transducer (geophone) is a sensor commonly used in various engineering disciplines, and generally consists of a wire coiled around a spring-suspended mass that surrounds a fixed magnet. When subjected to vibration or other excitation, the suspended wire mass moves relative to the magnet, creating an induced current in the wire that is proportional to the rate of change of magnetic flux, according to Faraday's Law (Brincker et al. 2006). If the constant of proportionality between the induced voltage and the rate of change is determined (in terms of volts per unit velocity) through calibration, the sensor can be taken to provide a direct measurement of the velocity of the suspended wire coil relative to the fixed magnetic field. It might seem plausible to simply integrate the discrete voltage-time signal of the geophone and multiply by the calibration constant of the geophone in the time domain to obtain measurement of displacement. However, it is important to note that geophones provide a direct measurement of the "raw" particle velocity of the spring-suspended mass inside the geophone and, depending on the frequency range of excitation, this may not correspond to the velocity of the surface upon which the geophone is placed, which is typically the parameter of interest (Graves and Drnevich, 1991; Tandon and Nazarian, 1990). Determining the latter requires signal correction to account for the limited frequency response of the geophones, which are known to attenuate low frequency components of signals below the natural frequency of the system.

2.1.2 Signal Processing Techniques

The importance of employing sound digital correction and signal processing techniques in determining deflections from geophones has been highlighted by many (Duong et al. 2018; Brincker et al. 2006; Brandt and Brincker, 2014; Nazarian and Bush, 1989; Chai, 1990; Tandon and Nazarian, 1990; Graves and Drnevich, 1991). Several techniques have been employed to process geophone signals. To obtain accurate deflection measurements under actual vehicular loading, Duong et al. (2018) and Bahrani et al. (2020) first used a filter with a cutoff frequency, set according to the transfer function of the geophone, to decompose the voltage signal into its high and low frequency components. Then, the low frequency component of the signal was amplified, both components were integrated in the time domain, a Hilbert transform was applied to remove oscillations and to extract the "envelope" of the signal, and finally the two corrected signal components were combined to obtain a corrected displacement-time history of the geophone. The results obtained by the authors showed good agreement between geophone measured deflections and an embedded linear variable differential transformer (LVDT), which indicated that geophones can provide good estimations of maximum deflections under actual traffic loading, provided that the low-frequency component of the signal is appropriately amplified.

An alternative method that has been reported in the literature for processing of geophone data to determine deflections is a frequency domain method that makes use of the concept of "inverse filtering" (Brincker et al. 2006). A geophone can be considered a damped single degree of freedom (SDOF) system (Nazarian and Bush, 1989; Chai, 1990; Graves and Drnevich, 1991). As such, a particular geophone will have a unique impulse response, or response to a unit delta function, that is governed by the natural frequency and damping characteristics of the system. The way in which the input ground velocity signal is blended with the unit impulse of the geophone to produce the geophone output signal is described by the mathematical operation of convolution. If the discrete input signal can be decomposed into a set of scaled and shifted delta functions, then it follows that the output resulting from each impulse is a scaled and shifted impulse response (Smith, 1997). Convolution describes the process of determining the overall output signal by adding these scaled and shifted impulse responses. The method of inverse filtering relies on the equivalence of convolution to multiplication in the frequency domain. Similarly, deconvolution in the time domain is the equivalent of division in the frequency domain (Nazarian and Bush, 1989; Graves and Drnevich, 1991). The raw voltage-time history of the geophone can be transformed into the frequency spectrum through the Fast Fourier Transform (FFT) to obtain a velocity spectrum. The system's impulse response can also be transformed into the frequency domain through the same process, which produces what is known as the frequency response function. The method of inverse filtering involves deconvolving the geophone output signal with the frequency response of the geophone through division in the frequency domain, which recovers low frequency components of the displacement signal that are attenuated by the geophone. To accomplish this, the raw velocity spectrum obtained through the FFT of the geophone voltage-time history is divided by the frequency response function (both magnitude and phase) of the geophone, which yields the actual velocity spectrum of the ground (Bentsen et al. 1989; Graves and Drnevich, 1991; Nazarian and Bush, 1989; Nazarian and Chai, 1992; Chai, 1990; Brincker et al. 2006). Integration is then performed in the frequency domain by dividing the displacement spectrum by $1/j\omega$, where ω is the circular frequency $(2\pi f)$ of each corresponding frequency bin of the FFT to obtain an actual displacement spectrum. Finally, the displacement spectrum is inverse transformed back into the time domain to obtain the displacement-time history of the ground.

2.1.3 Precision and Accuracy of Measurement

Bentsen et al. (1989) reported that based on past experience, the frequency domain method described in the previous subsection, when employed with a properly calibrated geophone, typically measures deflections that are within 5 percent or 0.1 mils of actual deflections (whichever is greater). Tandon and Nazarian (1990) further investigated the accuracy of geophone deflection measurements obtained using this method by evaluating the precision and accuracy of five sensors commonly used in pavement engineering for measurement of deflections. They compared deflections determined using these sensors to those obtained by a proximeter probe, which is non-contact in nature and is known to be one of the most accurate means of measuring deflections in laboratory environment (Chai, 1990). It was found that under half-sine impulse motion imparted through a shake table, deflections measured with geophones were generally within 2.5 percent of those measured with a proximeter, with variances among tests typically under 2.5 percent as well, and with particularly low variances observed for impulse motion frequencies exceeding 10 Hz. The authors also concluded that, despite the relatively complex data processing required to obtain accurate deflection measurements, geophones were likely the most practical of the five sensors evaluated in that study due to their very low cost, ruggedness/field worthiness, ease of installation, lack of mounting problems, and good precision and accuracy of measured deflections under both steady state and impulse motions. Graves and Drnevich (1991) employed similar laboratory calibration procedures and used a dynamic signal analyzer to compare shake table displacements to geophone displacements obtained through the frequency response method. The study found that peak displacement values differed by less than 1 percent. Potential sources of inaccuracy that have been highlighted in the literature include background noise, leakage errors, and receiver placement.

2.2 Instrumented Pavement Sections for Verification of Layered Elastic Theory:

Scullion et al. (1989) attempted to verify existing modulus backcalculation procedures by instrumenting two pavement sections at TTI’s research annex with multi-depth deflectometers (MDDs), which are essentially a system of LVDTs that are placed into a borehole within the pavement and are set up to measure displacement at various depths relative to a common datum at the bottom of the borehole. Both pavement sections were evaluated under FWD loading with a fixed distance from the edge of the FWD load plate to the center of the MDD borehole, and both FWD maximum surface deflections and MDD depth deflections were recorded. An independent method for determining in-situ layer moduli from MDD results based on the deformations between two successive sensors of the MDD relative to a fixed datum was employed. The results were then compared to backcalculation results using only FWD surface deflection data. The FWD backcalculation procedures produced a similar base and subgrade stiffness to that obtained with MDD analysis, which supports the concept of using surface deflections and layered elastic theory as a means of predicting the pavement stress-strain behavior at depth.

Nazarian and Chai (1992) employed seven non-destructive testing (NDT) devices on a site instrumented with embedded geophones. The objective was to assess the adequacy of using layered elastic theory in conjunction with NDT devices to predict the behavior of pavements, as well as to determine the effects that load level (i.e., potential nonlinear material response), sensor locations, and number of sensors have on backcalculated moduli. Four rows of three geophone units, each consisting of a horizontal and vertical geophone, were installed at different depths within the pavement: two rows within the base, and two rows within the subgrade. Prior to installation, the geophone units were assembled by carefully placing them in a PVC pipe and encapsulating them with an epoxy resin mix to prevent corrosion and moisture damage once installed. Several different NDT devices were then employed at varying positions above the embedded geophones and at different load levels to generate deflection data under controlled loading. Voltage output of embedded and surface geophones were captured. To assess the adequacy of layered elastic theory in conjunction with NDT devices to predict the behavior of pavements, the researchers compared deflection contour lines generated by the layered elastic analysis program BISAR, using backcalculated moduli from surface deflection data only, to contours produced using measured deflection data from embedded geophones. The BISAR-predicted and measured deflections varied significantly. However, improvements were obtained for agreement between predicted and measured deflections when data from other sensors were incorporated into the backcalculation procedure, even though this often led to poor basin fitting results in terms of absolute error per sensor. The observed improvement for the latter case supports the notion that backcalculation accuracy cannot be measured based on the success of basin fitting, but by the accuracy of stresses and strains within the pavement section. At times, a comparatively poor basin fit may actually result in adequate backcalculation accuracy. Researchers also assessed the effect of load-induced non-linearity, by assuming linear response of materials for strain levels below 0.003 percent, quasi-linear response for strains between 0.003 and 0.01 percent, and nonlinear response for strains exceeding 0.01 percent. It was concluded that predicted depth deflections from backcalculated NDT moduli using only surface deflections were not representative of actual measured deflections at these subsurface points, but that predicted deflections obtained from backcalculated NDT moduli, incorporating measured deflections away from the load, provided they fall within the linear range of unbound layer materials, may match reasonably well with measured deflections.

Akram et al. (1994) instrumented pavement sections with MDDs and collected surface and depth deflection data under both FWD and controlled truck loadings. Linear elastic analyses were performed using MODULUS 4.0 to compare layer moduli backcalculation using only surface deflections obtained by the FWD to moduli obtained when considering both surface and depth deflections, Layer moduli obtained from both of these cases were also subsequently compared to moduli obtained through laboratory testing. These backcalculated moduli were then used to predict pavement response under known truck loads, and such predictions were compared to in-situ strains measured under the controlled truck loading using the MDDs. A key finding of the study was that backcalculated moduli did not compare well with laboratory data, likely due to the fact that the laboratory tests were conducted under stress conditions that may not necessarily be representative of field conditions. The authors found that the moduli backcalculated through a consideration of both surface and MDD depth deflections produced the best match between predicted and measured subgrade strains under controlled truck loading. In contrast, using FWD moduli alone resulted in underestimation of truck induced vertical compressive strains at the top of the subgrade by 15 to 18 percent.

Appea et al. (2002) compared actual pavement responses measured at the Virginia Smart Road under varying FWD load levels using embedded pressure cells and strain gages to predicted responses obtained through backcalculated moduli. A robust instrumentation array was implemented, which consisted of thermocouples, moisture sensors, and frost probes in the different pavement sublayers for determination of the moisture and temperature at the time of testing. It was found that the measured stresses in the pressure cells closely matched those predicted using the linear elastic model KENLAYER. However, even better agreement was obtained when the subbase resilient modulus was characterized in the KENLAYER model considering a nonlinear constitutive model that was a function of the first stress invariant, or bulk stress which is equal to the sum of the principal stresses. Predicted tensile strains at the bottom of the HMA layer were also in good agreement with those measured by strain gages (+7 to +15 percent), and the fact that the predicted strains exceeded the measured strains as evidenced by the positive relative errors suggests that the model predicted strains were conservative.

Bahrani et al. (2020) focused on the use of geophones and accelerometers as a means of measuring surface deflections under actual traffic loading, with the goal of using these measurements to analyze field behavior and backcalculate layer properties. Geophones and accelerometers were tested for this application in a full-scale accelerated test using Carrousel APT at IFSTTAR. Surface deflection measurements collected with the geophones and accelerometers for tests at different speeds and vehicle loads were compared with a reference anchored sensor. Signal processing and filtering of sensor responses were conducted following the process outlined in Duong et al. (2020). A good match was obtained between displacements measured with geophones and those measured with reference anchored LVDT. Deflection basins obtained through accelerometer and geophone measurements were also used to backcalculate pavement layer moduli using Alize linear elastic pavement design software. The backcalculation process resulted in realistic moduli, indicating that the measured deflection basins using the geophones and accelerometers were appropriate for use in backcalculation analysis.

Chapter 3: Site Characterization, Device Description, and Data Collection

3.1 SH 21 Site Characterization:

3.1.1 Location and Description of Test Section

The data used in this study were generated at an instrumented field test section located near Bastrop, Texas, which involves the outside lane of eastbound State Highway (SH) 21. The data were generated as part of a research project conducted for the Texas Department of Transportation (TxDOT), which involves evaluation of the performance of instrumented test sections that include geosynthetic-reinforced asphaltic layers. While the focus of the investigation conducted in this thesis is on the evaluation of FWD and geophone data, an overview of the field test sections is provided herein to facilitate the context of the data analyzed subsequently in Chapters 4 and 5.

The 1,575 feet long site is bounded by the intersection of SH 21 and U.S. Route 77 to the west, and the intersection of SH 21 and Country Road 440 to the east, as shown in Figure 1. The instrumentation was installed in conjunction with a mill-and-overlay pavement rehabilitation project conducted by TxDOT. Within the test section, six different types of geogrids were installed as interlayer reinforcement within the HMA overlay as a part of the project, with the goal of monitoring the long-term performance of the different subsections in terms of degradation over time, as a means of evaluating this relatively new application for geosynthetics in roadways as structural reinforcement in HMA layers.

Figure 1: Test Section Location

The site of the test section is relatively flat, with an average slope of approximately +0.36 percent when travelling in the eastbound direction. Wide drainage swales are located beyond the north and south roadway shoulders, which serve to convey stormwater to an outlet ditch located outside the western limits of the project area, which eventually sheds into West Yegua Creek to the southeast. Based on visual observation, the roadway dewatering and drainage systems appear to be efficient, an important consideration to avoid negative performance of the new overlay. A view of the test site is provided in Figure 2 (a) and (b) looking in the westbound and eastbound directions, respectively.

Figure 2: SH 21 Test Site: (a) View in Westbound Direction (b) View in Eastbound Direction

The USDA Web Soil Survey indicates that the site of interest is represented by the Kurten series (KgC), typically consisting of gravelly fine sandy loam within the first 0 to 7 inches underlain by eighty or more inches of high plasticity, stiff clay. The saturated hydraulic conductivity representative of the site is in the range of very low to moderately low (0.00 to 0.06 in/hr.), which is indicative of a high potential for overland flow. A total of seven auger samples were collected from the test section to depths of 80 to 100 inches, and sieve/hydrometer analysis as well as Atterberg limit tests were performed to classify the soil. Of the samples evaluated, liquid limits ranged from 50 to 85, and plasticity indexes ranged from 30 to 60. The USCS classification for the soil was CH (fat clay) or G-CH (gravelly fat clay). Bedrock was not encountered in any of the soil borings. The AASHTO soil classification representative of the subgrade at the site is A-7-6.

3.1.2 Pavement Profile and Rehabilitated Cross-section

Table 1 summarizes the representative HMA lift thicknesses as well as the total thickness of two core samples taken from the outside lane, outer wheel path in each of the test sections, which were averaged to determine the representative layer thicknesses in each section. The previously described auger borings were also used to determine the characteristics and thicknesses of the base and subbase materials, which are included in Table 1 as well. However, it should be noted that the accuracy of this auger sampling technique in determining representative layer thicknesses is likely not better than one inch near the surface and decreases with depth. The generalized profile of the rehabilitated pavement in the outside lane, outer wheel path where instrumentation was installed consists of high plasticity clay subgrade to depths exceeding 6.5 feet, a 9 to 12 inch flexible subbase, a 6 to 7.5 inch cement-treated base, old HMA 3.0 to 5.5 inches thick, a 1 to 1.75 inch leveling course (Levelup), a geosynthetic interlayer (except for Section 4), a 2.25 to 2.5 inch thick TxDOT Type D binder course (TY D), and a 0.5 to 1 inch thick Thin Overlay Mix (TOM) surface course.

Table 1: Representative Pavement Layer Thicknesses (Zornberg J.G. et.al. TxDOT Project 0-7002 – Tech Memo 3, January 31, 2021)

Section	Core Sample	TOM (in.)	TY D (in.)	Levelup (in.)	Old HMA (in.)	Total Thickness (in.)	Base Thickness (in.)	Subbase Thickness (in.)
1	1.1	0.69	2.38	1.00	5.00	9.06	6	9
	1.3	1.00	2.13	1.13	5.50	9.75		
	AVG	0.84	2.25	1.06	5.25	9.41		
2	2.1	0.75	2.50	1.75	3.50	8.50	6	9
	2.3	0.75	2.25	1.75	3.13	7.88		
	AVG	0.75	2.38	1.75	3.31	8.19		
3	3.1	1.06	2.25	1.50	3.88	8.69	6.5	9
	3.3	0.75	2.50	1.24	3.75	8.24		
	AVG	0.91	2.38	1.37	3.81	8.46		
4	4.1	0.56	2.25	1.00	5.50	9.31	6	10
	4.3	0.56	2.31	1.69	3.50	8.06		
	AVG	0.56	2.28	1.34	4.50	8.69		
5	5.1	0.56	2.44	2.00	3.50	8.50	7	9
	5.3	0.56	2.50	1.75	3.75	8.56		
	AVG	0.56	2.47	1.88	3.63	8.53		
6	6.1	0.63	2.50	1.50	3.75	8.38	7	12
	6.3	0.56	2.13	1.50	3.25	7.44		
	AVG	0.59	2.31	1.50	3.50	7.91		
7	7.1	0.63	1.75	1.50	3.50	7.38	7.5	12
	7.3	0.50	2.25	1.75	3.25	7.75		
	AVG	0.56	2.00	1.63	3.38	7.56		

As previously mentioned, the full 1,575-foot test section was divided into 7 subsections, each with a different type of geogrid installed as an interlayer in the HMA overlay, with the exception of Section 4 which was the control section and did not have a geosynthetic reinforcement. Of the sections with a geosynthetic, each of the products except for that installed in Section 6 could be classified as a geogrid composite, consisting of a biaxial geogrid attached to a nonwoven geotextile. The product installed in Section 6 is classified as a biaxial geogrid and does not have a geotextile backing. The products vary significantly in the type of polymer making up the geogrid and geotextile, tensile strength and stiffness, mesh size, and coating. The application of tack coat also varied section to section but conformed to manufacturer's recommendation for each specific product. A summary of the type and engineering properties of the geosynthetics installed in each section is included in Table 2, with a view of the installation of the geosynthetic taking place in two of the test sections included in Figure 3.

Table 2: Engineering Properties of Geosynthetic Reinforcement (Zornberg J.G. et.al. TxDOT Project 0-7002 – Tech Memo 3, January 31, 2021)

Geosynthetic Material composition	GT Type	Tensile strength (lbs/in)		Elongation at break (%)		Mesh size (in)	Mesh size (mm)	Coating
		MD	TD	MD	TD			
Polyester	thick nonwoven	339	333	<12	<13	1.2	30.5	Bitumen
Polyester	ultra-thin nonwoven	286	286	<12	<12	1.576	40	Bitumen
Polyvinyl Alcohol	ultra-thin nonwoven	286	286	<6	<6	1.576	40	Bitumen
Control	N/a	N/a	N/a	N/a	N/a	N/a	N/a	N/a
Fiberglass	ultra-thin nonwoven	571	571	<3	<3	1.182	30	Bitumen
Fiberglass	N/a	571	571	<3	<3	0.985	25	Elastomeric
Fiberglass	very thick nonwoven	655	655	<3	<3	1.4972	38	No Coating

Figure 3: Installation of Geosynthetic Reinforcement in Test Sections

3.2 Instrumentation:

3.2.1 HGS Geophones

The geophones used in this study were HGS (India) Limited HG-6 low-frequency geophones, with a rated natural frequency and damping ratio of 4.5 Hz, and 0.70, respectively. The operating temperature range for these geophones is -40 to 212 degrees Fahrenheit. The two assemblies used in this project consisted of either a single HG-6 geophone encased in a HL-5 Land Case (1D), or 3 HG-6 geophones encased in a HL-6B Land Case oriented perpendicular to one another (3D). The cases are waterproof with an IP67 rating and are constructed with impact modified polymers for enhanced durability. The two complete assemblies along with associated wiring are as shown in Figure 4.

Figure 4: Installation of HG-6 Geophones in (a) HL-5 Land Case (1D) and (b) HL-6B Land Case (3D) Assemblies

3.2.2 Installation Methodology

The installation of geophones took place after milling of the existing HMA and subsequent construction of the leveling course, but prior to installation of the geosynthetic, Type D binder course, and TOM. In each section, geophones were installed in the array configuration as shown in Figure 5. Figure 5 (a) shows a plan view of the geophone array, with geophones differentiated into three locations based on the longitudinal spacing. Figure 5 (b) provides a sectional view of the geophones installed in Location 1 viewed in the longitudinal direction. Figure 5 (c) shows a similar sectional view of geophone Location 1, but in the transverse direction (perpendicular to the direction of traffic).

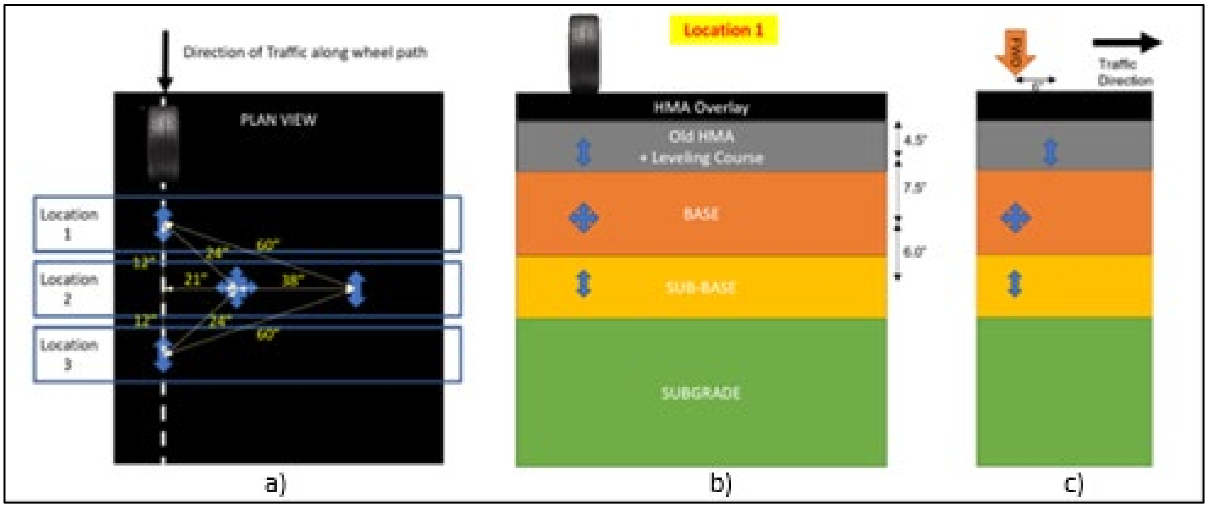

Figure 5: Geophone Arrays in SH 21 Test Sections: (a) Plan View of Geophone Array , (b) Sectional View of Geophone Location 1 in Longitudinal Direction, (c) Sectional View of Geophone Location 1 in Transverse Direction

Location 1 corresponds to the first set of geophones in the direction of traffic and is located in the outside wheel path of the outer lane. Immediately preceding the installation of the first two geophones, the existing asphalt was cored to reach the underlying pavement layers. An auger was then used to remove material down to a depth of approximately 6.5 feet below the top of the leveling course. The excavated material was sorted according to depth, so that it could eventually be backfilled to approximately the same depth from where it was collected. Sensors were placed at a depth of 6.5 feet to provide continuous monitoring of subgrade moisture conditions, and a sand-bentonite mixture was placed on top to prevent the sensor measurements from being compromised due to downward infiltration of water. Two geophones were installed along a vertical axis. The subgrade and subbase material were infilled and compacted within the boring, and the bottom 1D geophone was installed within the subbase at a depth of eighteen inches from the top of the leveling course. The assigned location descriptor associated with this particular geophone in each section is GPH_WP_SB_0_V1, where the "GPH" stands for geophone, "WP" indicates that the sensor is located in the outer wheel path of the outside lane, "SB" indicates the sensor is installed in the subbase, "0" represents the radial distance (ft) from geophone Location 1 to the sensor, and "V1" indicates a 1D geophone oriented vertically. The HL-5 and HL-6B case assemblies come with 75 mm trivalent plated steel spike bases, but the spikes were removed prior to installation of the case assemblies to minimize disturbance of the underlying compacted material in the borehole. A bubble level was used to ensure the case was vertically oriented, and then suitable material that had been previously excavated from the borehole was infilled around the geophone assembly and compacted to in-situ density.

The next geophone at this location was a 3D geophone installed within the base course using the same methodology as previously described, located six inches above the lower most geophone. The naming convention for this geophone is similar to the first, with an assigned descriptor of GPH_WP_BC_0_V3. In this case, all attributes are the same with the exception of the "BC" term which indicates that this geophone is installed in the base course and the "V3" term which indicates a 3D geophone with the deflection of interest oriented in the vertical direction. The wiring from the geophones and moisture sensor was routed to the data acquisition system located in a handhole adjacent to the shoulder of the road through a transverse notch that was cut in the HMA to connect the two locations. Base material was then placed and compacted above the location of the case up to the bottom of the HMA, and the hole where the core was taken and wiring channel were filled in with a cold patch material. Several weeks later, an additional 1D geophone with naming convention GPH_WP_HM_0_V1 was installed within the existing HMA at Location 1 in conjunction with the installation of other sensors embedded in the HMA at Locations 2 and 3. However, this geophone was installed at 6 inches off the vertical axis of the other two geophones in the direction of traffic for constructability purposes, to avoid damaging the wiring from the previously installed sensors, since the exact depth and location of the wiring within the previous borehole was unknown. The installation of these geophones along with a separate wiring channel that was cut to route these additional wires to the data acquisition system is pictured in Figure 6.

Figure 6: Geophone Installation in HMA

Although the full geophone array consisted of those embedded in the subbase, base, and HMA at Location 1, as well as additional geophones located in the HMA at Locations 2 and 3 as shown in Figure 5, for the analysis of the agreement between predicted and geophone measured deflections, only deflection measurements obtained from the three geophones corresponding to Location 1 with an FWD drop immediately over the axis of subbase and base installed geophones were considered in this study.

This approach was adopted for several reasons. First, the roadway encompassing the site was only a single lane in each direction at some point in the past and was subsequently widened to two lanes during a prior rehabilitation project. For this reason, the pavement profile is not homogeneous, and the old HMA becomes thicker towards the center of the outside lane and towards the inside lane as evidenced by two additional core samples that were taken in each section from the center of the outside lane, as well as from GPR surveys that were conducted prior to rehabilitation. This makes it difficult to compare deflections obtained by the geophones corresponding to Location 2 with the deflections corresponding to other geophones in the outside wheel path. Second, a sensitivity analysis was performed to account for one potential source of error: the precision of the location of FWD drops. Since the FWD is trailer-mounted and testing involved a total of sixteen drop locations in each section that must be tested during a given loading campaign, it was often not feasible to ensure that the load plate was perfectly centered over the required drop location for each test. The layered elastic analysis software WinJULEA was used along with the representative pavement profile and geophone locations corresponding to Section 1 to determine the sensitivity of the predicted deflections. Specifically, differences in predicted deflections for the three geophones corresponding to Location 1 if the center of the load application were shifted three inches in the direction of traffic, versus being oriented directly over top of the vertical axis of the geophones installed in the base and subbase. It was found that a difference on the order of 1 percent would be predicted for the subbase deflections, 1.5 to 2.0 percent for the base deflections, and approximately 9 percent for the HMA deflections. These are likely overpredictions of the actual differences, since WinJULEA assumes a flexible plate (representative of a vehicle tire loading) while the FWD loading mechanism consists of a rigid plate which would lead to more uniform settlements at all locations beneath the loading plate. However, for measurements taken at increasing radial distances from the center of loading application, particularly for those which are not beneath the 300 mm loading plate of the FWD, the difference in predicted deflections between the two cases is more significant, exceeding 10 percent at the depth of the geophone installed in the base at a radial distance of twenty-four inches. It was thus concluded that considering deflections measured by the geophones corresponding to Location 1 from FWD tests conducted at increasing radial distances away from the geophone axis as being representative of deflections measured at specific radial distances from an applied load would not be appropriate. The reason for this conclusion was that the difference in predicted deflections due to a relatively small imprecision in location of FWD drop location would likely lead to a percentage error of measurement in exceedance of a value which would be considered “good” agreement between predicted and in-situ measured deflections.

The one exception to this previously described conclusion is for the geophone embedded in the HMA at Location 1. Since this geophone is located at a 6 inch offset in the direction of traffic from the vertical axis of the other two geophones (which corresponds to the radius of the FWD load plate), it was found that if the deflection measured by this geophone were averaged with the deflection measured by an additional FWD drop centered 12 inches in the direction of traffic from the previous location, the percentage difference in predicted deflections due to the stated imprecision of load application is reduced from 8.8 percent to only 0.67 percent. For this reason, the deflection corresponding to the geophone located at a 6-inch radial distance embedded in the HMA was taken to be the average of the deflections measured by this geophone for two drops: one located over the vertical axis of the other two geophones, and the other centered an additional twelve inches in the direction of traffic.

3.3 Dynatest Falling Weight Deflectometer:

3.3.1 Description of FWD Device

For determination of in-situ stiffness of pavement layers for use in network level analysis or project specific design inputs into the design program FPS 21 (Liu and Scullion, 2011), TxDOT uses the Dynatest FWD. This device is trailer mounted and imparts a dynamic load to the pavement via a hydraulic load column which lifts a stack of weights that can be dropped from varying heights onto a set of rubber buffers mounted on a bracket that is connected to a 300 mm (11.8 in.) diameter load plate in contact with the pavement, as shown in Figure 7, sub-figures a) and b). A side and rear view of the row of seven geophones that can be moved to varying radial distances (with the exception of the center sensor, which is mounted in the center of the load plate) is shown in sub-figures c) and d), respectively. Prior to administering the test, these geophones are hydraulically lowered and are placed in contact with the pavement for monitoring of surface deflections of the pavement at the specific points of contact for each geophone when the load is applied. The device has an effective dynamic force range 1,500 to 27,000 lbf depending on the drop height (Bentsen et al. 1989). It also has the capability to measure ambient air temperature and pavement surface temperature at each drop location through a built-in thermocouple and infrared sensor. Accurate measurements of pavement surface temperature are necessary for prediction of pavement temperature with depth. Since the stiffness of asphalt decreases with increasing temperature, determining a representative pavement temperature is crucial in being able to apply correction factors to backcalculated HMA modulus values to bring measurements to a common reference temperature, if section performance comparisons are to be made across different seasons or times of day.

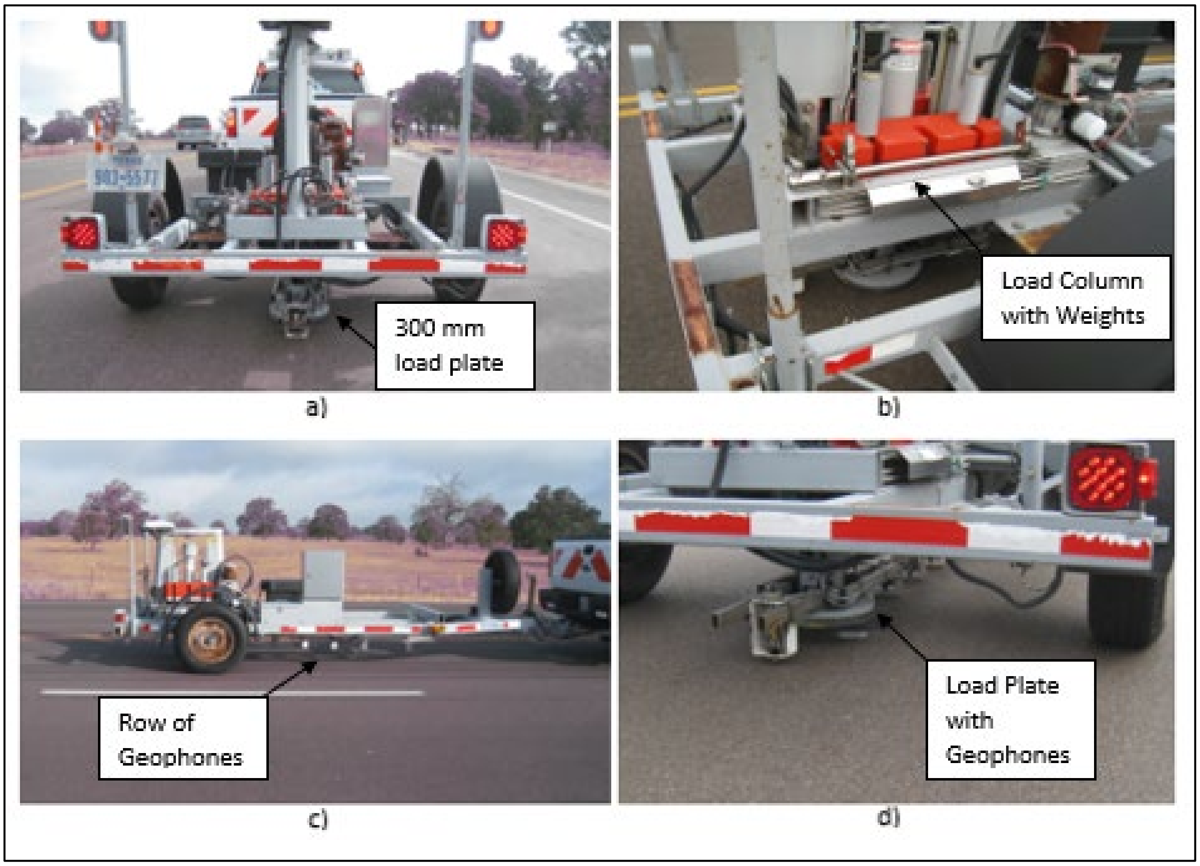

Figure 7: Dynatest FWD: (a) Rear View of Load Plate, (b) Hydraulic Load Column with Weights, (c) Side View of Trailer with Geophones, (d) Close up View of Load Plate with Geophones

For this project, the geophone radial spacing was set to increments of twelve inches (0 in, 12 in, 24 in, 36 in, 48 in, 60 in, 72 in). The typical testing sequence at each test location consisted of a total of five drops. The first was the 6,000 lbf seating load and was not considered in the analysis. This was followed by a single drop at 6,000 lbf, two 9,000 lbf drops (the second one was considered in this analysis), and single 12,000 lbf drop. An exception to this approach occurred during the fifth loading campaign, which took place on 09/16/2020, where only three drops were made, each at 9,000 lbf.

3.3.2 Load Campaign Summary

Throughout the course of the project, a total of eight loading campaigns were conducted where FWD data was generated by the research team. These consist of one day of testing on the old HMA plus the level-up (07/22/2019), one day of testing on the Type D (10/02/2019), and six visits for testing on the TOM layer after rehabilitation was complete (10/15/2019, 12/19/2019, 09/16/2020, 12/01/2020, 03/24/2021, 09/01/2021). Of these loading campaigns, the data considered for the FWD analysis used in this investigation consists of data from the load campaign on the old HMA, and the first, second, third, and sixth tests on the full rehabilitated pavement. These dates were chosen to get adequate information on the baseline performance of the pavement layers prior to rehabilitation and without geosynthetic (old HMA), performance shortly after completion of the rehabilitation on a hot day (TOM 1), performance shortly after completion of the rehabilitation on a cold day (TOM 2), and performance one year (TOM 3) and two years (TOM 6) after completion, both on hot days.

Figure 8 shows the location of all FWD tests that were conducted during each loading campaign at SH 21, with labeled star symbols representing the location of one FWD test. However, only a select few of these FWD tests were actually considered in this analysis. The right side of the figure provides an enlarged view of the tests conducted in the vicinity of pavement instrumentation, since a large number of tests were conducted in a relatively small area. For the backcalculation analysis and comparison of predicted and in-situ measured deflections using geophones, backcalculation of layer moduli were performed based on the FWD test at drop location 10, which corresponds to the location of the first set of geophones. Limited use of data corresponding to tests at drop location 11 was also made for the purpose of averaging the two deflection measurements for the HMA embedded geophone. Additional data from drop locations

1, 2 and 3 were incorporated for use in the deflection basin parameter analysis for comparison of performance of the different test sections over the first two years of the project.

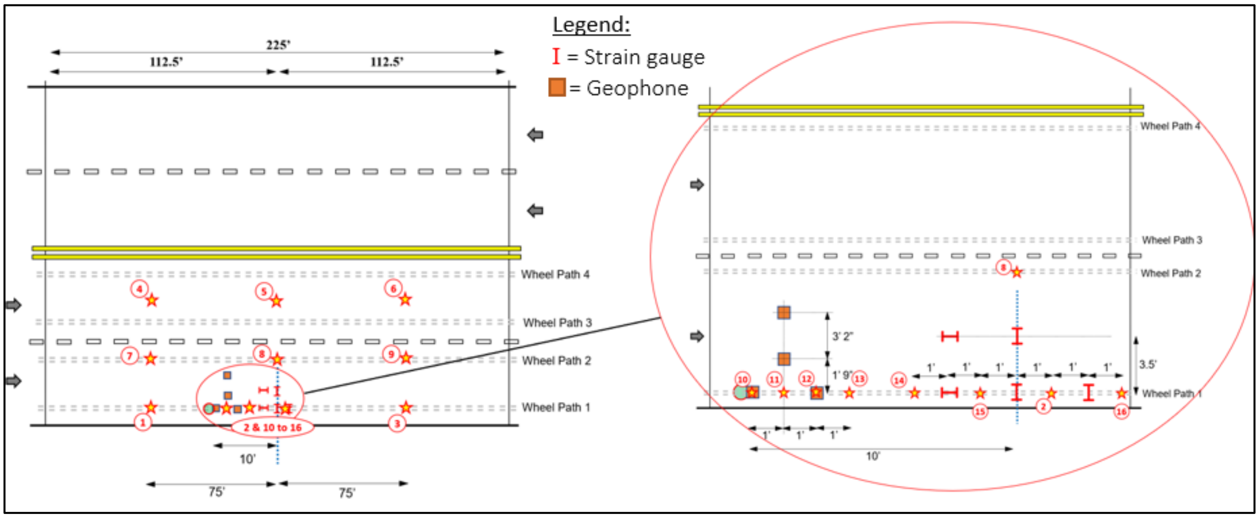

Figure 8: SH 21 FWD Drop Locations During Loading Campaigns

Chapter 4: Data Reduction and Processing

4.1 Determination of Depth Deflections using Geophones:

The procedure adopted in this study for determining in-situ pavement deflections using geophones is based on the frequency domain method discussed in Chapter 2 (Bentsen et al. 1988; Graves and Drnevich, 1991; Nazarian and Bush, 1989; Nazarian and Chai, 1992; Chai, 1990; Brincker et al. 2006). While the process could have been carried out in the time domain, such approach would be highly computationally inefficient. Accordingly, the approach was conducted in the frequency domain. A summary of this process in both the frequency and time domains is included in Figure 9. The general roadmap for the time domain approach involves starting with the known discrete sampled voltage-time history, *y(n),* deconvolving with the geophone unit impulse response, *h(n),* to obtain the velocity-time history of the ground, *v(n),* and then integrating to obtain the displacement time history of the ground, *x(n).* The frequency domain approach proceeds similarly except the Fast Fourier Transform (FFT) is first used to transform the voltage-time history into a raw voltage spectrum, *Y(k),* which is then deconvolved with the frequency response function of the geophone, *H(k),* to obtain the ground velocity spectrum*, V(k).* The velocity spectrum is then integrated in the frequency domain to obtain the ground displacement spectrum, *X(k),* which is finally transformed back into the time domain to obtain *x(n)*, The details of the frequency domain approach will be subsequently explained in detail.

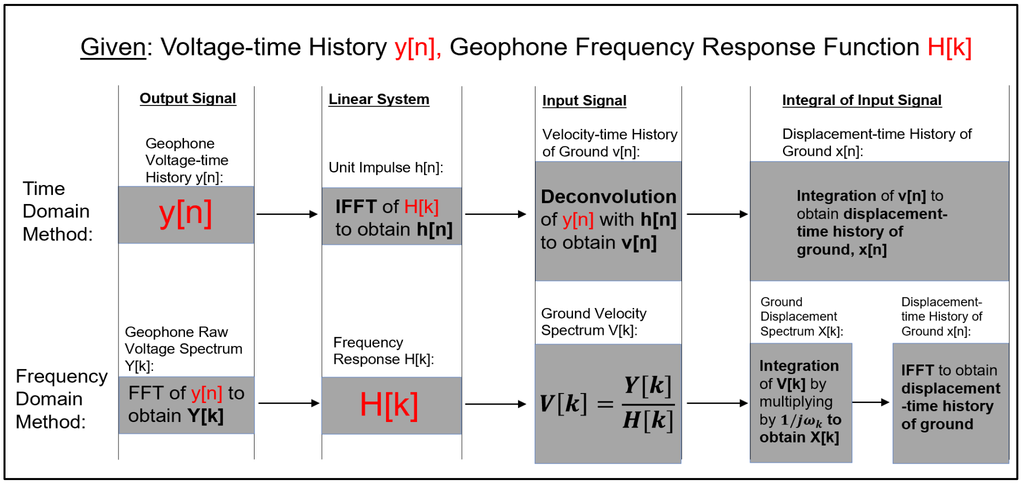

Figure 9: Time and Frequency Domain Methods for Determination of Ground Deflections using Geophones

For this project, the available data include the raw voltage-time history as measured by the geophones as well as the manufacturer's provided calibration data for each individual geophone (sensitivity, natural frequency, damping ratio). The first step in the process was to remove the non-zero average, or DC offset from the raw voltage signal, since this would lead to the appearance of a continuous constant of integration that would distort the shape of the integrated displacement signal (Duong et al. 2018). Next, the mean-corrected voltage-time history was zero-padded with a number of zeros equal to the length of the original signal to prevent aliasing due to circular convolution (Brandt and Brinckner, 2014). An example of a mean-corrected and zero-padded geophone voltage-time history signal is shown in Figure 10. The zero-padded signal was then transformed into the frequency domain using the FFT to obtain the raw voltage spectrum shown in Figure 11.

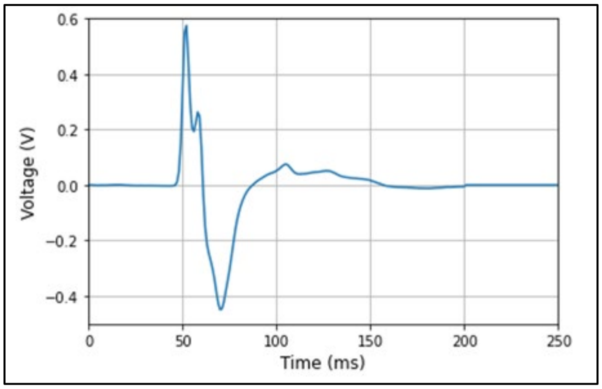

Figure 10: Voltage Time History

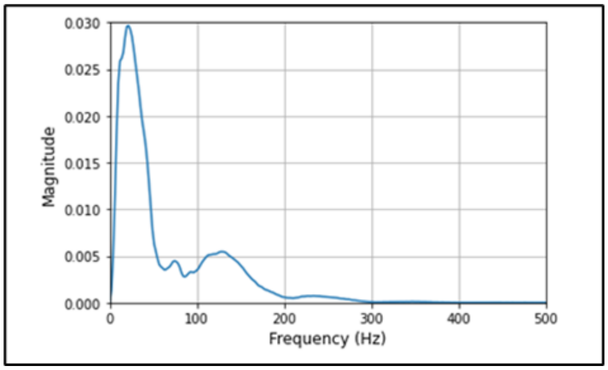

Figure 11: Voltage Spectrum

The next step is deconvolution, which equates to division in the frequency domain. As previously discussed, to deconvolve the geophone response from the original ground motion (to obtain the actual velocity spectrum of the ground), the voltage spectrum can be divided by the frequency response function of the geophone (magnitude and phase) in the frequency domain. However, doing so required definition of the geophone frequency response. Nazarian and Bush (1989) derived the dynamic frequency response function of a geophone by considering an idealized model of a geophone shown in Figure 12 involving a mass *m* suspended by a parallel spring with a spring constant *k*, and dashpot with a damping coefficient *c* affixed to the ground, with the ground subjected to a vertical harmonic excitation *u*(*t*). The subsequent movement of the mass is thus described by another function *y(t)* relative to the same fixed datum, and the relative movement between the coil and magnet is *z(t) = y(t) – u(t)*.

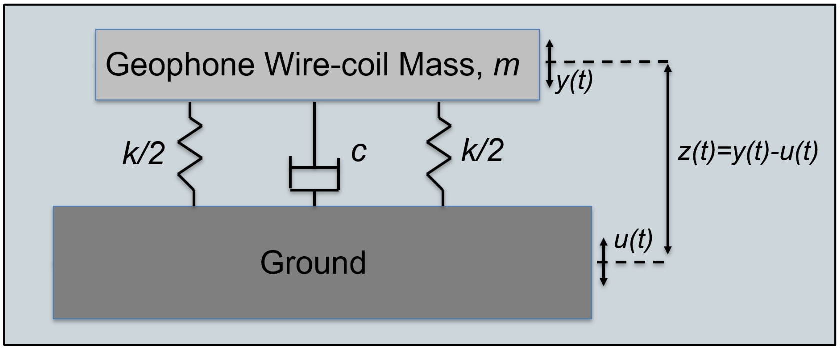

Figure 12: Idealized Model of Geophone

The differential equation of motion for the above model was written, and the solution was obtained as:

$$z(t) = z_o e^{i\,2\pi f t} \tag{1}$$

with

$$z_o = u_o * \frac{r^2}{[(1-r^2)+(i\,2Dr)]} \tag{2}$$

$$r = \frac{f}{f_n} = \frac{f}{\left[\frac{\sqrt{\frac{k}{m}}}{2\pi}\right]} \tag{3}$$

$$D = \frac{c}{c_c} = c/(2\sqrt{km}) \tag{4}$$

Where f_n is the natural frequency of the system, c_c is the critical damping, *D* is the damping ratio, and z_o represents the maximum deformation of the mass relative to the magnetic field. If both sides of the equation for z_o are divided by u_o which is the maximum movement of the ground, the resulting expression is the frequency response function of the geophone, *H(k)* given by

$$H(k) = \frac{r^2}{[(1-r^2)+(i\,2Dr)]} = \frac{f^2}{[f_n^2+i\,2f_n f D-f^2]} \tag{5}$$

This function is of the same form of a simple, SDOF system, differing only in that a high pass filter is described as opposed to a low pass filter (Brincker et al. 2006). With this formulation, the frequency response function of the geophone can be defined, provided that the natural frequency and damping ratio are known. In this case, these constants were provided by the manufacturer. However, the geophones used in this project had an average damping ratio of 0.706, with 68 percent of the sensors having a damping ratio within the narrow range of 0.671 to 0.729. For this reason, it was decided to approximate the frequency response of the geophones as a second-order high pass Butterworth filter, which is described by Equation 5 but has a damping ratio of 0.707. These filters are known as "maximally flat" filters because they have the sharpest possible roll-off from the linear frequency range without inducing peaking in the frequency response function, which would be expected at lower damping ratios (Ellis, 2012). This approach was adopted to simplify the programming and to increase the computational efficiency needed to determine a large number of deflections. This is because the only program inputs for the geophones needed to define the frequency response function would be the sensitivity and natural frequency. A comparison of frequency response functions of the geophone in terms of magnitude and phase as described by the transfer function in Equation 5 versus approximating the response as a second order high-pass Butterworth filter is made in Figure 13 for damping ratios of 0.707, 0.671, and 0.729. As shown by the results in the figure, the frequency response functions for a damping ratio of 0.707 are indistinguishable. Slight peaking is observed in the transfer function when compared to the Butterworth filter for a damping ratio of 0.671, while for a damping ratio of 0.729, the frequency drop-off from the linear range is slightly more gradual for the curve represented by the derived transfer function.

A trial integration using the remainder of the process that is to be described in this section was performed to determine the difference in results resulting by assuming a damping ratio of 0.707 for all geophones. When the actual damping ratio was one standard deviation below the mean (0.671), the actual ground deflection obtained through integration was overpredicted by 0.88

percent. When the actual damping ratio was one standard deviation above the mean (0.729), the actual ground deflection was underpredicted by 0.55 percent. The magnitude of these errors was deemed acceptable for this type of sensor measurement, particularly considering that the frequency response function was derived from an idealized model using manufacturer's calibration constants. The use of such model is also not a perfect representation of the system, so performing a frequency sweep of input motion using a shake table and measuring sensor response to different frequencies would be the most accurate means of defining a representative frequency response for each geophone.

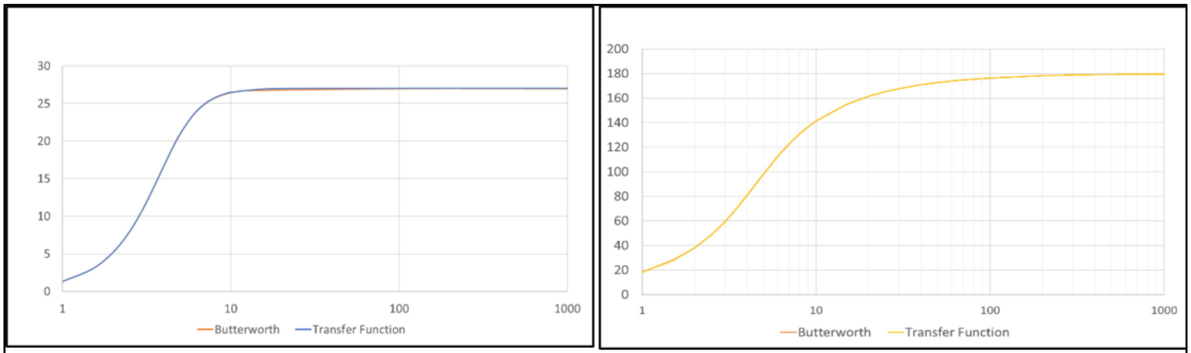

a) Sensitivity (V/m/s) – D=0.707 d) Phase Lag (deg.) – D=0.707

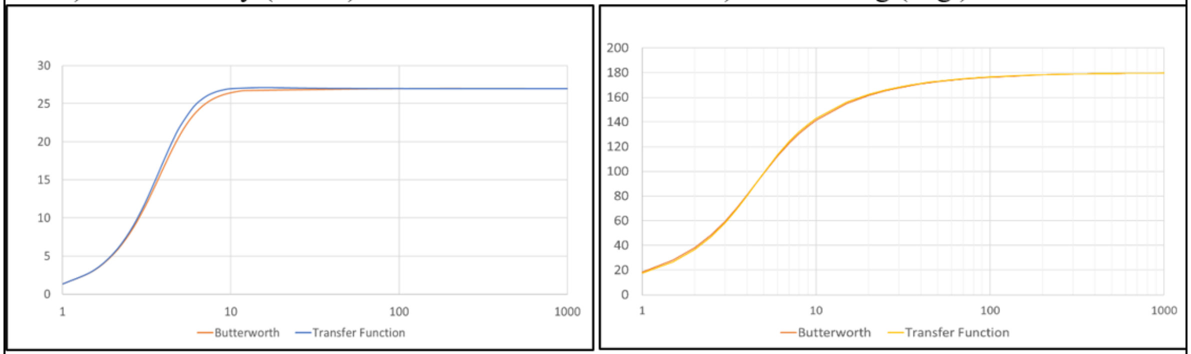

b) Sensitivity (V/m/s) – D=0.671 e) Phase Lag (deg.) – D=0.671

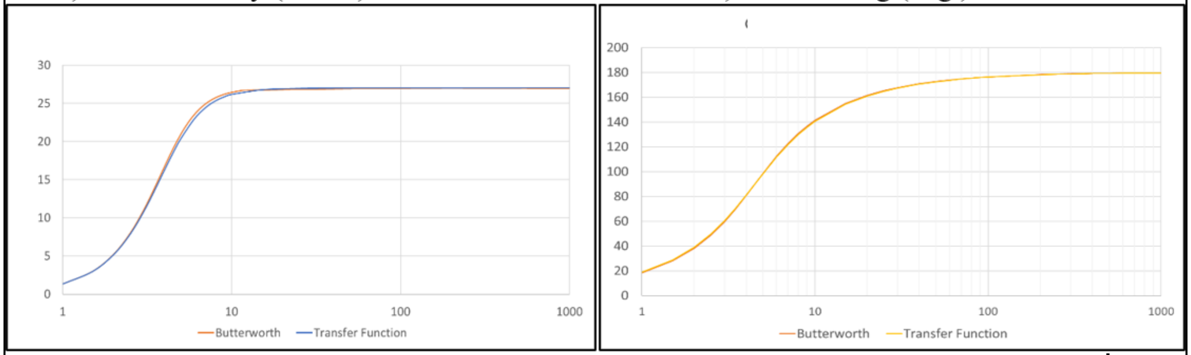

c) Sensitivity (V/m/s) – D=0.729 f) Phase Lag (deg.) – D=0.729

Figure 13: Comparison of Derived Transfer Function to Second Order Butterworth Filter: a) Sensitivity (D=0.707) b) Sensitivity (D=0.671), c) Sensitivity (D=0.729), d) Phase Lag (D=0.707), e) Phase Lag (D=0.671), f) Phase Lag (D=0.707)

Once the frequency response function of the geophone has been defined, shown in Figures 14 and 15 in terms of magnitude and phase, the actual velocity spectrum of the ground shown in Figure 16 was generated by dividing the voltage spectrum by the frequency response function for each corresponding bin frequency. The ground velocity spectrum was then integrated in the frequency domain to obtain the displacement spectrum of the ground as shown in Figure 17 by dividing each frequency bin by the integration operator, $j\omega_k$ (Brandt and Brincker, 2014).

Finally, the inverse of the FFT is performed to transform back into the time domain and ultimately obtain the actual displacement-time history of the ground, as shown in Figure 18. One issue was noted with the displacement-time history signal that was obtained for the ground motion. It is common practice to detrend an output signal (i.e., removing mean and slope) after FFT, integration, and IFFT to correct for leakage errors that may occur during the process (Brandt and Brincker, 2014). However, in this case the trend in the output data actually appears to be nonlinear, in the form of a low-frequency (2-3 Hz) sinusoid with an amplitude on the order of 0.1 to 0.5 mils depending on the magnitude of the applied load. The apparent frequency of this harmonic trend is approximately equal to the width of one frequency bin (equal to the sampling frequency of 600 Hz) divided by the number of data points in the original signal (256). Consequently, it appears that this nonlinear trend occurrs as a result of aliasing of high frequency noise attributable to very small magnitude fluctuations between individual measured data points at 600 Hz into apparent low frequencies during the FFT process. Even though the magnitude of the noise in the voltage-time signal is very small, the trend could be much more prevalent after deconvolution since the voltage spectrum is divided by the frequency response of the geophone prior to integration, which essentially amplifies the low frequency components of the signal that were attenuated by the geophone to recover the original output signal. For the purposes of this study, this nonlinear trend was simply removed from the output signal by fitting a sixth order polynomial to the portions of the signal that should be zero and subtracting such function from the entire signal to obtain a corrected displacement time history, as shown in Figure 19. This process was carried out for all three geophones (vertical deflections only) corresponding to geophone Location 1 in each section and at each FWD drop load level for the loading campaigns as indicated in Chapter 3, and the data were recorded for future comparison to predicted (theoretical) deflections.

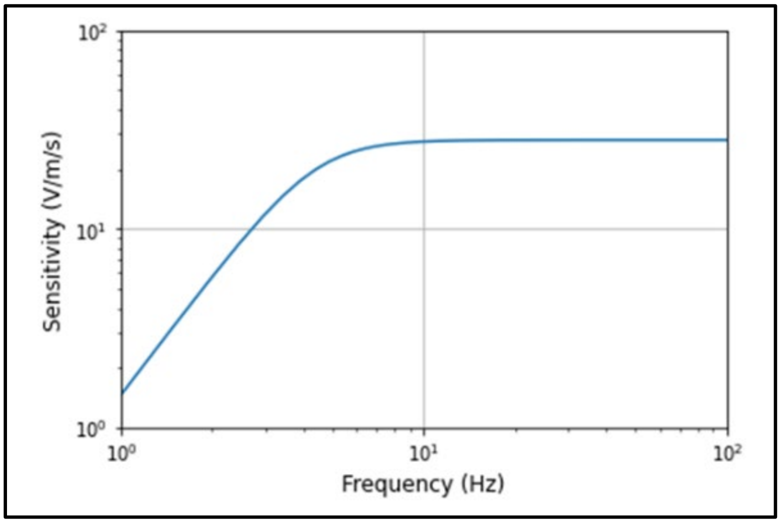

Figure 14: Geophone Frequency Response (Magnitude)

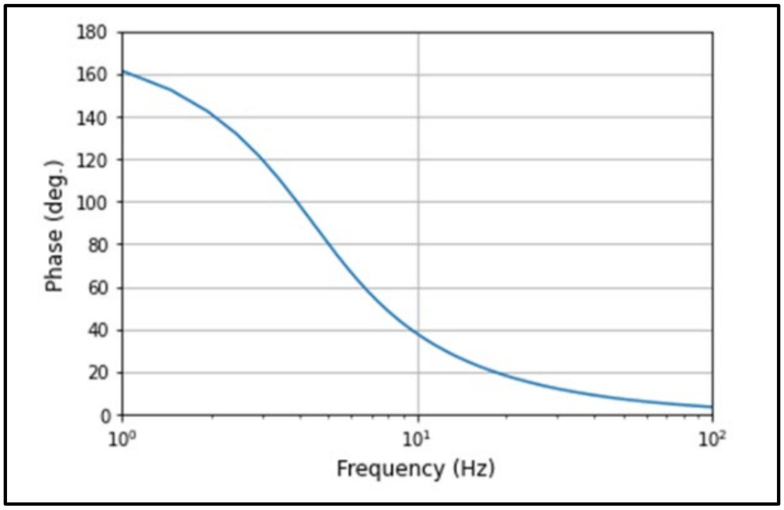

Figure 15: Geophone Frequency Response (Phase)

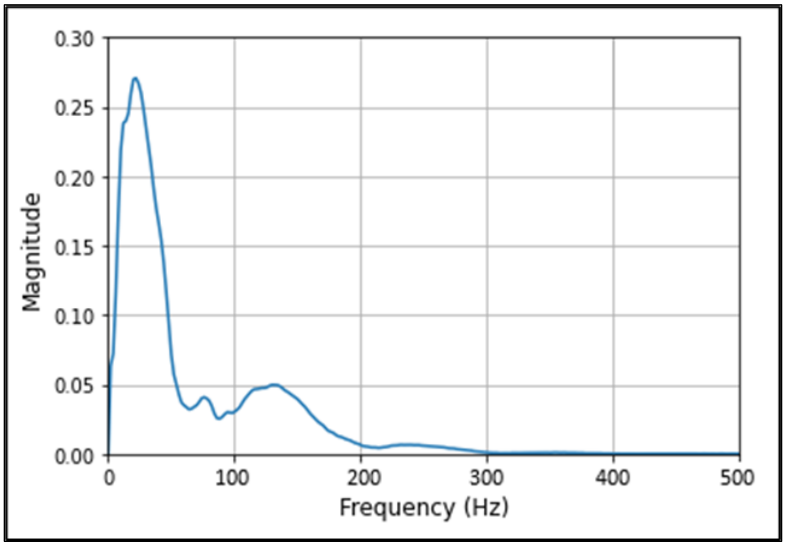

Figure 16: Actual Velocity Spectrum

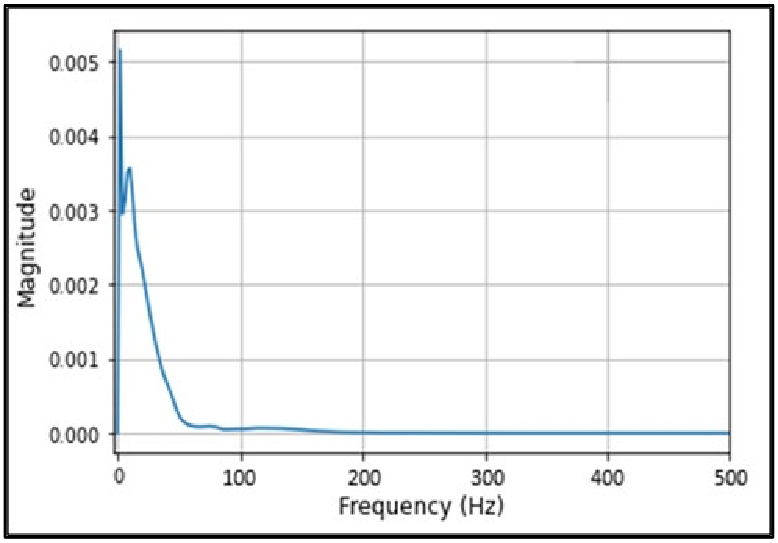

Figure 17: Actual Displacement Spectrum

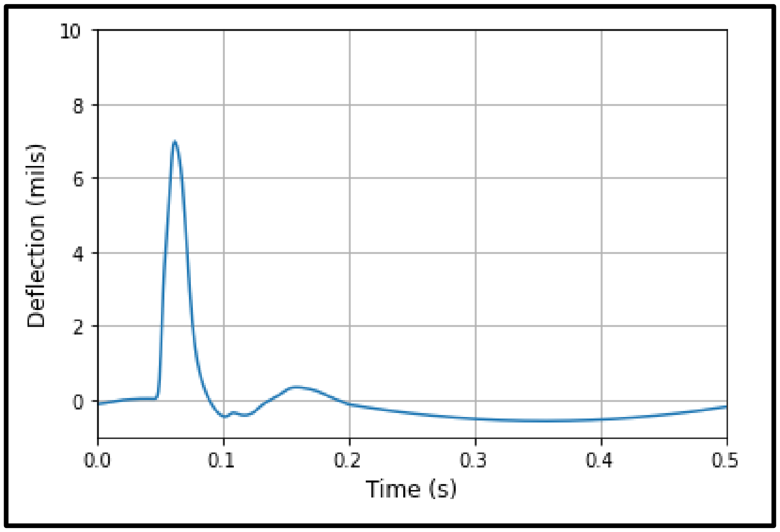

Figure 18: Ground Displacement time history

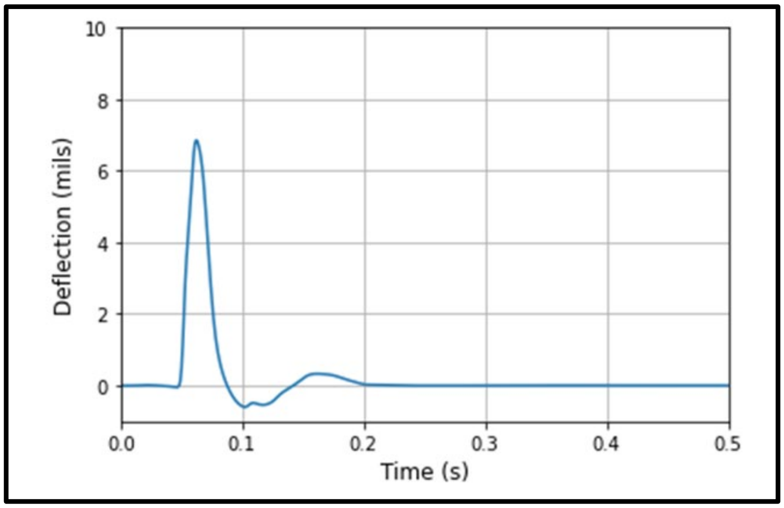

Figure 19: Detrended Displacement time history

4.2 Determination of Moduli:

4.2.1 MODULUS 7.0

The program used in this study for the backcalculation of layer moduli is the MODULUS 7.0 program developed by the Texas Transportation Institute at Texas A&M University (Scullion et al. 1990), which is also the program used by TxDOT for this purpose. As shown in Figure 20, the required user input into the program includes the raw deflection file, layer thicknesses, Poisson's ratios, and ranges of reasonable moduli for each pavement layer or "seed" moduli (Scullion et al. 1990). The program also assumes rough (non-slip) interface conditions between layers for the analysis.

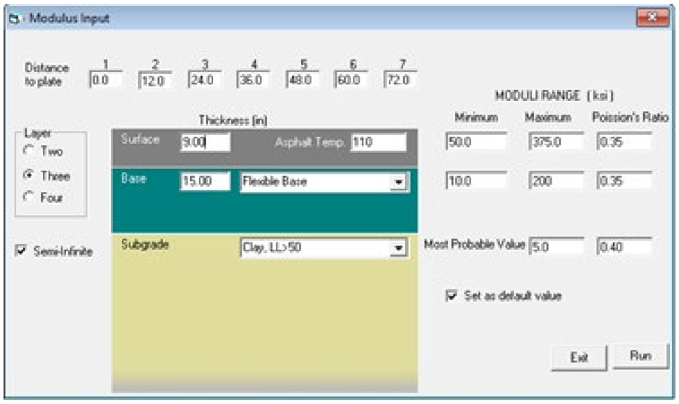

Distance to plate	1	2	3	4	5	6	7
	0.0	12.0	24.0	36.0	48.0	60.0	72.0

Layer: ○ Two ● Three ○ Four

☑ Semi-Infinite

	Thickness (in)		Minimum	Maximum	Poission's Ratio
Surface	9.00	Asphalt Temp. 110	50.0	375.0	0.35
Base	15.00	Flexible Base	10.0	200	0.35
Subgrade		Clay, LL>50	Most Probable Value	5.0	0.40

MODULI RANGE (ksi)

☑ Set as default value

Figure 20: MODULUS 7.0 Backcalculation Input Window

The program uses a static layered elastic analysis program WESLEA, which was developed by the U.S. Army Corps of Engineers Waterways Experiment Station (WES), in a forward calculation using the drop force recorded by the FWD load cell to generate a database of possible deflection bowls based on different combinations of layer moduli that fall within the user specified range. Since in a layered, linear elastic analysis if the Poisson's ratios and layer thicknesses are known, the deflection at a point can be said to be linearly related to load level, inversely proportional to the subgrade modulus, and a function of the ratio between moduli of the overlying layers (Scullion et al. 1990). The objective function to be minimized is the square root of the sum of relative errors between deflection measurements multiplied by a weighting factor for each sensor. The errors are the differences between the measured and predicted deflection bowls, and optimization is achieved using the Hookes-Jeeves pattern search algorithm to find combination of moduli values that minimizes the objective function (Scullion et al. 1990). A convexity test that evaluates the shape of the error surface is then used to determine the possibility of a local minimum. Once optimization is achieved, the resulting layer moduli, theoretical deflection basin, and average percentage error per sensor are recorded in the output file, and the backcalculation is complete.

An advantage of this database approach, as compared to iterative backcalculation procedures, is that only a fixed number of forward calculations are performed to generate a database of deflection basins, which can then be searched and interpolated by the optimization algorithm to find a deflection basin resembling the one that was actually measured. This is in contrast to the approach followed by programs using iterative backcalculation processes. In such programs, the number of forward calculations required to achieve a good match are highly dependent on how close the initial seed moduli inputs are to the actual representative layer moduli (Chou and Lytton, 1991). Even with the computing power of modern devices, the time required for an iterative backcalculation to converge may be prohibitive (on the order of several minutes per backcalculation as opposed to seconds), especially if analysis is required for a large number of deflection basins. One disadvantage of this type of method is that the optimized theoretical deflection basin obtained is interpolated in the database searching procedure based on the deflection basins obtained by a finite number of forward calculations. Therefore, the optimized solution is not completely accurate based on layered elastic theory. However, others have found good agreement between moduli backcalculated through the MODULUS program to those obtained through other iterative programs (Chou and Lytton, 1991).

The program can be used to analyze 2, 3, or 4-layer pavement systems, though based on personal experience and input from TxDOT, the backcalculation results become unreliable when a 4-layer system is analyzed due to non-uniqueness of the solution in the basin fitting. This was found to be the case for backcalculation results at SH 21. When a 4-layer analysis was considered, at many locations the most optimal basin fitting (in terms of least average error per sensor) was obtained by the backcalculation program when the modulus of the cement treated base was unreasonably low, often on the order of 20-30 ksi, while the subbase modulus was significantly higher, on the order of 100 ksi. Consequently, all backcalculation analyses in this study were performed considering a 3-layer system obtained by either a combined base and subbase, or a combined subbase and subgrade. Other features of the most recent program updates (Rohde and Scullion, 1990; Liu and Scullion, 2001) include a procedure to estimate the depth to an apparent rigid layer. Such procedure involves assuming the radial distance to the point where the deflection is zero (extrapolated from the shape of the deflection basin) is closely related to the depth of an apparent rigid layer. The program also optimizes the number of sensors incorporated into the backcalculation analysis by using the Boussinesq equation for deflection under a point load to determine the location on the surface of the pavement where the measured deflection is only due to deformation of the subgrade, and then only incorporating one sensor beyond that surface location, with the overriding factor being that the number of sensors must exceed the number of layer moduli to be determined by one. The backcalculation program also applies sensor weighting factors equal to δ_{mi}/δ_{1i} , where δ_{mi} is the deflection measured a given sensor and δ_{1i} is the maximum deflection measured directly beneath the load plate. This normalization with the maximum deflection for a given drop prevents excessive influence on the backcalculation result by either the deflections closer or further away from the point of load application (Rohde and Scullion, 1990).

4.2.2 SH 21 Backcalculation Routine

For the project site at SH 21, multiple backcalculations were performed for use in the forward calculation and eventual comparison between predicted and measured deflections. Section thickness properties for each section were taken to be those presented in Chapter 3, but only a 3-layer analysis was performed with two separate analyses for a given drop on a particular day to assess the impact of user input / assumptions in the backcalculation procedure: (1) considering a combined base and subbase, and (2) considering a combined subbase and subgrade. Backcalculation was performed in each section for the first (baseline, hot), second (cold), third (1-year, hot), and sixth (2-year, hot) loading campaigns for evaluation of the effect of pavement temperature and time on the agreement between predicted and measured deflections. A separate backcalculation was also performed for each nominal drop force (6,000 lbs, 9,000 lbs, 12,000 lbs) to evaluate the effect of load level. The Poisson's ratio was assumed to be 0.35 for the HMA, base, and subbase material, and was assumed to be 0.40 for the subgrade. The HMA seed modulus range was set to 50 – 375 ksi by the program based on the program default after inputting a mean pavement temperature. A seed modulus range of 10 – 200 ksi for the combined base/subbase was set, along with a most likely subgrade modulus of 5 ksi. The depth to the apparent stiff layer routine of the MODULUS program consistently estimated depths that were at or around the program maximum of 300 inches (25 feet), so in all cases the subgrade thickness was set to semi-infinite.

The average absolute error per sensor obtained after backcalculation when the section was characterized as having a combined base and subbase was 1.1 percent. Instead, such error was 1.9 percent when the section involved a combined subbase and subgrade. Consequently, both approaches would be well within the presumed range of acceptability of less than 10 percent. Due to the large volume of data, the complete results of this analysis have been included in Appendix B.

4.3 Forward Calculation using Backcalculated Moduli:

A forward calculation was performed based on the moduli obtained from each individual backcalculation scenario included in the second analysis as previously described using a Python program developed (and benchmarked against the layered elastic analysis program WinJULEA) by a fellow researcher at the university, to perform multi-layer linear elastic analysis (Sankaranarayanan, 2021). Layer interface conditions were assumed to be fixed in order to match assumptions made by the MODULUS program during backcalculation. Required inputs to the program for each separate backcalculation result included four separate csv files, as follows: (1) the theoretical load or loads to be applied to the pavement (i.e., 6,000 lbs, 9,000 lbs, 12,000 lbs), (2) the section properties to include layer thicknesses, moduli, and Poisson’s ratios, (3) the contact area (in^2) over which the load is to be applied (assumed to be circular), and (4) a spreadsheet with the three-dimensional coordinates (z coordinate corresponds to depth) of the specific locations of interest within the pavement section. In the evaluation conducted in this study, the depth coordinates represent the locations of the geophones in Geophone Location 1 with respect to the center of the load plate when placed at drop location 10. The program output included a separate .csv file in the same folder as the four input files which included the theoretical deflection in the z-direction (inches) for each loading condition and at each of the defined points of interest. These results were then tabulated for comparison to the actual measured deflections.

Chapter 5: Analysis and Discussion

5.1 Deflection Basin Parameters as Qualitative Indicators of Section Performance

5.1.1 Overview of Deflection Basin Parameters

Deflection basin parameters (DBPs) are algebraic expressions that describe the slope, normalized slope, or area underneath the deflection basin generated during non-destructive testing. DBPs can be used as indicators of the structural condition of individual pavement layers, both in geosynthetic-reinforced and non-reinforced pavement sections (Horak and Emery, 2006; Joshi 2010). DBPs are commonly employed for network level pavement assessment due to their simplicity and their suitability to rapidly assess the structural condition and degradation of individual layers within a pavement section. They can also be used to assess the reasonableness of moduli results obtained through a more rigorous backcalculation procedure, which would be necessary if the desire is to be able to actually predict stresses and strains within the pavement under the design loading.

A DBP analysis of the SH 21 site was initially performed to provide a preliminary comparison of the behavior of the seven different pavement test sections. The exact reasoning for observed differences in behavior among the different test sections (due to different geogrids) are beyond the scope of this study. The intent was to identify differences or trends in observed performance in particular sections and across different loading campaigns that may be useful to interpret results regarding the comparison of predicted and measured deflections in each section that will come later in this chapter (see Chapter 5.3). The analysis performed followed steps that were adopted from the initial part of the MODULUS 7.0 "Remaining Life" routine, as follows (Michilak and Scullion,1995):

1. A master file of FWD maximum deflection data (from the second 9,000 lbs drop only) from each geophone was generated for the specific dates and drop locations of interest
2. A linear correction was developed to normalize the deflections to a 9,000 lbs load
3. Temperature correction was applied to normalize all deflections to a 70F reference temperature

4. After obtaining the corrected deflections, The DBPs of interest were calculated for each drop

For generation of the DBP file, the drop locations of interest selected were Locations 1, 2, and 3, which corresponded to the outside lane, outer wheel path but not immediately on top of any of the installed instrumentation. The particular dates included in the analysis correspond to field testing conducted over the old HMA plus the level up course as a baseline prior to geosynthetic (08/20/2019), the first test on the fully rehabilitated pavement (10/15/2019), the fifth test on the full rehabilitated pavement (03/24/2021), and the sixth test on the full rehabilitated pavement (09/03/2021). For the latter dates, field testing was actually performed at the drop locations of interest twice: first thing in the morning, and again later in the afternoon, which provided an opportunity to validate the temperature correction procedure. The primary reason for choosing these drop location and dates is that the corresponding tests in each section were performed in rapid succession within a comparatively short time window, so the pavement temperature is very similar section-to-section, and therefore potential errors introduced due to assumptions made in temperature correction procedure are minimized (i.e. similar temperature correction factors would be applied to each section on a given day). In essence, the temperature correction is only serving to smooth the results. Figure 21 shows the mean pavement temperature during field testing in each of the seven SH21 sections for the four loading campaigns evaluated in the study. During TOM6, two tests were performed at each location: one in the morning, and one in the afternoon. These groups of tests are considered separately in the analysis and are designated as TOM6 (M) for the morning session and TOM6 (A) for the afternoon session. As shown in the figure, the temperature during the field tests conducted (in each section) are comparatively similar for any given loading campaign.

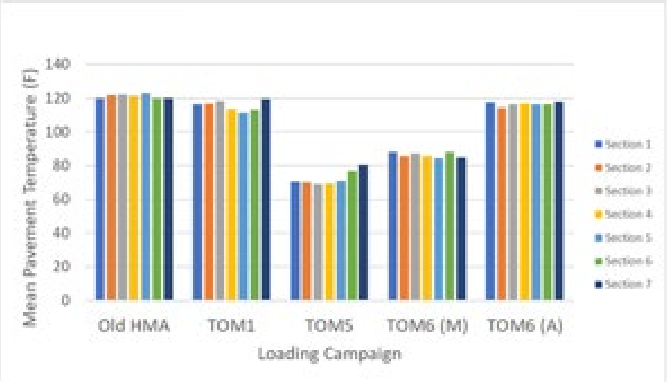

Figure 21: Mean Pavement Temperature (F)

Since for a given drop the dynamic force imparted to the pavement is not precisely equal to the nominal (i.e., target) drop force, all deflections were normalized to a 9,000 lbs load by dividing by the drop force recorded by the load cell for that particular drop, and then multiplying it by 9,000 to account for variations in the results due to applying a load that is slightly larger or smaller than the nominal loads.

Next, the deflections were corrected to a standard 70F reference temperature using procedures described by Bush (1987), who developed several correlations between correction factors and mean pavement temperature for different asphalt thicknesses. Employing a correction based on these correlations required definition of the mean pavement temperature in each section, taken to be the average of the infrared (IR) scanner recorded surface temperature and predicted temperature at the bottom of the HMA. The temperature at the bottom of the HMA was estimated using the Texas-LTTP equation, which is one of three options for predicting temperature with depth in the MODULUS Temperature Correction Program (MTCP) (Fernando and Liu, 2001). The equation uses the same variables as the BELLS2 and BELLS3 but was specifically calibrated using data from 1575 observations from Seasonal Monitoring Program sites in Texas, New Mexico, and Oklahoma. The Texas-LTTP equation was reported to improve the standard error of estimate to only 3.1 degrees Celsius when using data from these sites, from 4.1 degrees Celsius when the BELLS2 equation was used. The required inputs into the Texas LTTP equation include the IR scanner measured surface temperature (IR) in degrees Celsius, the depth to the location of interest in the pavement (d) in millimeters, the average of the high and low air temperatures of the prior day ($T_{(1-day)}$) in degrees Celsius, and the time of day (24-hour system in decimal format), but calculated using an 18-hour temperature rise and fall cycle (hr_{18}) (Details on assigning the hr_{18} number can be found in ASTM D7228 – 06a (2020)). The resulting equation for predicting the pavement temperature at a specific depth *d* is:

$$T_d = 6.460 + 0.199 * (IR + 2)^{1.5} + \log_{10}(d) * (\{-0.083 * (IR + 2)^{1.5} - 0.692 * \sin^2(hr_{18} - 15.5) + 1.874 * \sin^2(hr_{18} - 13.5) + 0.059 * \left[T_{(1-day)} + 6\right]^{1.5}\} - 6.783 * \sin^2(hr_{18} - 15.5) * \sin^2(hr_{18} - 13.5)) \tag{6}$$

Once the mean pavement temperature was estimated and correction factors for each drop were defined, these factors were then applied to the load-normalized deflection basins. Although the correlations developed by Bush (1987) specifically pertain to deflections beneath the center of the load plate, weighted correction factors (62%, 34%, 10%) were also applied to the second, third, and fourth deflection measurements (Michilak and Scullion, 1995).

Finally, the DBPs were calculated for each drop. The DBPs evaluated in this study included the deflection at the farthest sensor away from the load plate (W7), Surface Curvature Index (SCI), Spreadability (S), and Base Damage Index (BDI).

5.1.2 Outermost Deflection (W7)

The deflection of the outermost sensor is related to the strength of the subgrade, with larger deflections indicative of weaker subgrades. In the MODULUS program, when the "remaining life" routine is selected, the W7 measurements for each drop location are transformed into a qualitative strength classification based on correlations between FWD measured deflections and DCP strength. Specifically, W7 deflections less than 1 mil corresponding to "Very Good" deflections between 1 and 1.4 mils corresponding to "Good", 1.4 to 1.8 mils being "Moderate" or "Fair", between 1.8 and 2.2 mils being "Poor" and anything greater being classified as "Very Poor" (Michilak and Scullion, 1995). The deflections obtained in this analysis were classified according to these criteria, and the results are included in Table 3. From the results in this table, it can be seen that there is improvement from Fair to Good in several sections in most sections from the baseline test case on the loading campaigns identified as "Old HMA" to TOM 1 and TOM 5, but that the condition index in most sections drop from TOM 5 to TOM 6. The subgrade conditions in sections 3, 4, 5, and 7 are classified on a range from fair to good at the time of TOM 6, while the subgrade condition indices for sections 1, 2, and 6 are classified as poor.

Table 3: Subgrade Layer Classification

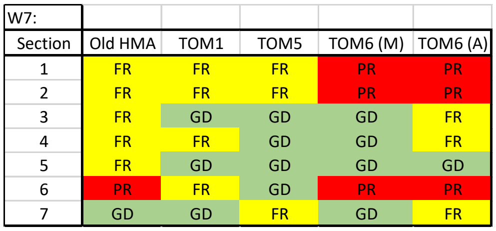

W7:					
Section	Old HMA	TOM1	TOM5	TOM6 (M)	TOM6 (A)
1	FR	FR	FR	PR	PR
2	FR	FR	FR	PR	PR
3	FR	GD	GD	GD	FR
4	FR	FR	GD	GD	FR
5	FR	GD	GD	GD	GD
6	PR	FR	GD	PR	PR
7	GD	GD	FR	GD	FR

Note: FR (yellow) = "Fair", GD (green) = "Good", PR (red) = "Poor"

Figures 22 and 23 describe the quantitative change in W7 over the different loading campaigns, with Figure 22 corresponding to the pavement sections classified in the "Fair" to "Good" range for all loading campaigns and Figure 23 corresponding to pavement sections classified as "Poor" for one or more loading campaigns (Note: Section 4 is the control section and was included in both figures for comparison). The trends observed in the results in this figure indicate that subgrade behavior over time appears similar in sections classified as fair or good, and remains fairly consistent over the loading campaigns considered, only varying on the order of 0.2 – 0.4 mils. In the sections classified as poor during TOM 6, larger fluctuations in subgrade stiffness are observed, varying on the order of 0.5 to 1.0 mils among observations. These sections also consistently appear to have weaker subgrades across all loading campaigns. These differences, particularly the observed increase between TOM 5 and TOM 6, may be primarily attributed to the moisture content of the subgrade and granular layers, although additional evaluation of subgrade conditions is needed to identify the subgrade conditions during the different loading campaigns.

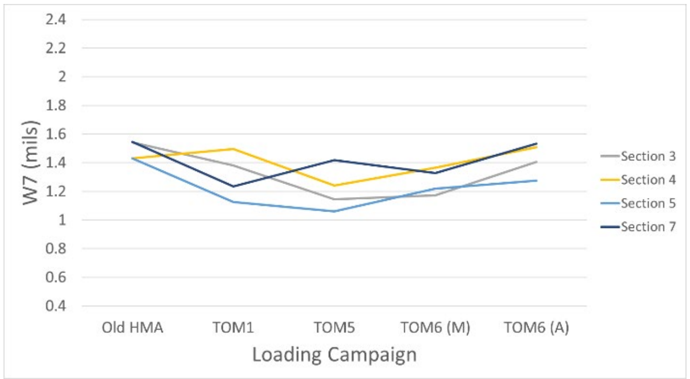

Figure 22: Average Outermost Deflection in Sections 3, 4, 5, and 7

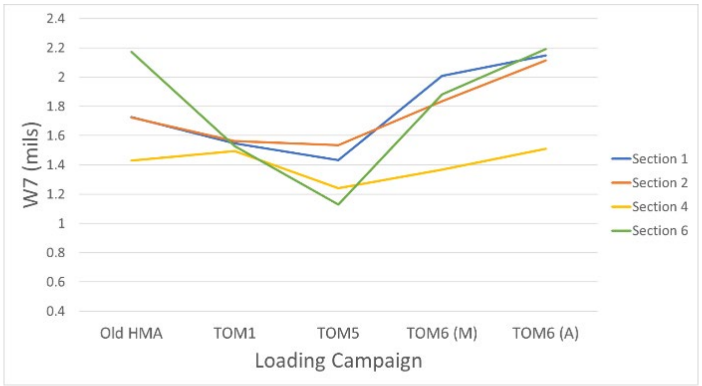

Figure 23: Average Outermost Deflection in Sections 1, 2, 4, and 6

With the exception of the control section (Section 4), all sections showed a reduction in W7 between the test on the Old HMA plus the level-up and the first test on the TOM. This trend can be explained by the fact that a larger pavement thickness leads to a reduction in the vertical compressive stress on the subgrade imposed by traffic loading. Since the W7 primarily relates to the performance of the subgrade, a reduction in vertical effective stress on the subgrade will result in a smaller W7. On the other hand, the observed increase in W7 between the morning and afternoon test sessions for TOM 6 can be explained by the increased vertical compressive stress on the subgrade due to a weaker surface layer at higher temperatures. Temperature correction factors are not applied to the W7, so it is not unexpected that different results would be obtained at different times on a given day.

5.1.3 Surface Curvature Index (SCI)

The surface curvature index (SCI) refers to the slope between the centermost deflection and first deflection outside of the loading plate. The SCI has been reported to serve as an indicator of the structural strength of the top eight inches of the pavement structure for a sensor spacing of 12 inches (Michilak and Scullion, 1995), which for the case of this project corresponds to the HMA layer. A comparatively high SCI is indicative of a weak surface layer. Based on similar correlations made for the subgrade material, surface structural condition indices have also been developed, with the classification of "Very Good" corresponding to SCIs less than 4 mils, "Good" for SCIs between 4 and 6 mils, "Moderate" or "Fair" for SCIs between 6 and 8 mils, "Poor" for SCIs between 8 and 10 mils, and "Very Poor" for greater values. Table 4 shows the SCI assigned to each section and during each loading campaign included in the analysis, which are all in the range of "Very Good".

Table 4: Surface Layer Classification

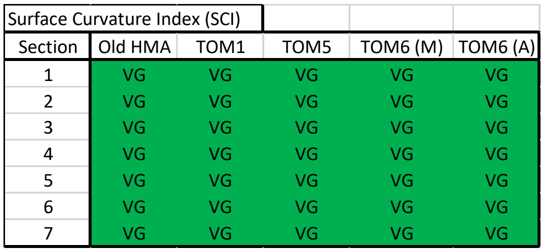

Surface Curvature Index (SCI)					
Section	Old HMA	TOM1	TOM5	TOM6 (M)	TOM6 (A)
1	VG	VG	VG	VG	VG
2	VG	VG	VG	VG	VG
3	VG	VG	VG	VG	VG
4	VG	VG	VG	VG	VG
5	VG	VG	VG	VG	VG
6	VG	VG	VG	VG	VG
7	VG	VG	VG	VG	VG

Note: VG (dark green) = "Very Good"

Figure 24 shows the temperature and load normalized SCI for each of the different sections during the load campaigns included in this analysis. The decreasing SCI from loading campaign "OLD HMA" to loading campaign TOM1 is consistent with a better performing surface layer in terms of distributing applied loads over a larger area. The increasing SCI in each subsequent loading campaign (TOM1 to TOM6) suggests that damage is beginning to accumulate in each section, though should be noted that it is still very early on in the rehabilitated pavement lifecycle, and the associated structural condition index remains very good in each section. Still, it is striking that in Sections 1 and 7, the rate of damage appears to be somewhat higher when compared to the rate obtained in other sections within the first two years of pavement life, with the SCI increasing between 1.25 and 1.75 mils (between TOM 1 and TOM 6), compared to the range of approximately 0.75 to 1 mil for the other sections. Also, while the effectiveness of the temperature correction is supported by the fact that corrected SCI is very consistent between the morning and afternoon sessions of TOM 6 in most sections, this is not the case for Sections 1 and 7, which both show significant increases in corrected SCI between the morning and afternoon. Interestingly, the difference in mean pavement temperature between the morning and afternoon sessions in these two sections does not appear to be any more significant than for the other sections. This suggests that there may be certain factors prevalent in these sections that are not adequately accounted for by the temperature correction factor correlations developed by Bush (1987) based on data from low volume airfield pavements, and these unexplained factors are causing the SCI to increase between tests at higher temperatures but on the same day.

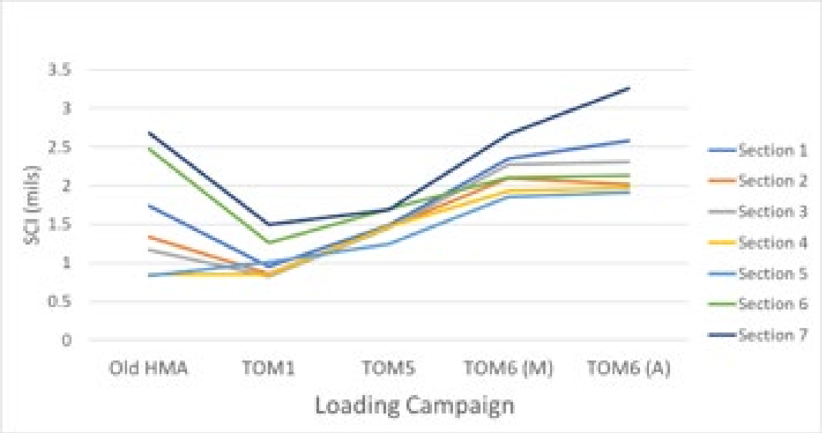

Figure 24: Surface Curvature Index (SCI) of Pavement Sections

5.1.4 Spreadability (S)

The spreadability (S) of a pavement system has been reported to be indicative of the bending stiffness, which pertains to the ability of the pavement to distribute load throughout the structure (Sargand et al. 2013). Its formula is given by:

$$S(\%) = 100\ x\ \frac{\sum_{i=1}^{7} W_i}{7W_1} \tag{7}$$

Where W_i corresponds to the deflection measured by a particular sensor of the FWD and W_1 corresponds to the maximum deflection which is measured by the sensor in the center of the load plate. A spreadability of 100 percent pertains to extremely high bending stiffness, while the theoretical minimum spreadability for a deflection bowl with a deflection of any value at the center of the load plate and zero everywhere else is 14.3 percent. Condition indices were assigned to sections based on spreadability, with values exceeding 65 percent deemed "Very Good", values between 55 and 65 percent determined to be "Good", values between 44 and 55 percent as "Fair" and anything lower than 44 percent taken to be "Poor" (Sargand et al. 2013). A summary of these condition indices is included in Table 5.

Table 5: Spreadability Condition Index

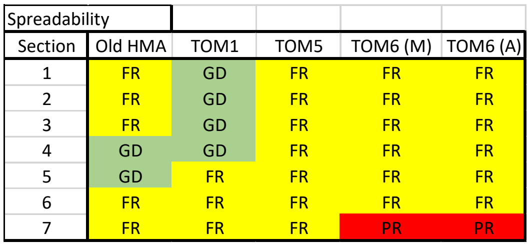

Spreadability					
Section	Old HMA	TOM1	TOM5	TOM6 (M)	TOM6 (A)
1	FR	GD	FR	FR	FR
2	FR	GD	FR	FR	FR
3	FR	GD	FR	FR	FR
4	GD	GD	FR	FR	FR
5	GD	FR	FR	FR	FR
6	FR	FR	FR	FR	FR
7	FR	FR	FR	PR	PR

Note: FR (yellow) = "Fair", GD (green) = "Good", PR (red) = "Poor"

Except for Section 5 (which is believed to involve erroneous measurement during the load campaign on the Old HMA), all sections were observed to have an increase in spreadability between the Old HMA and the rehabilitated pavement section. Figure 25 shows how the calculated spreadability in each pavement section changes among the loading campaigns included in this analysis. Based on the trends on S observed in this figure, it appears that the associated increase in spreadability due to the rehabilitation is minimal in Section 7. It is not unexpected that a Very Good spreadability rating was not achieved in any section following rehabilitation, since the spreadability is related to the combined flexural stiffness of all pavement layers and not simply the HMA that was rehabilitated. However, it is unexpected for the apparent increase in spreadability as a result of resurfacing to be as small as it was observed to be in Section 7. The spreadability in each section appeared to subsequently decrease with time, likely due to the accumulation of damage within the pavement section. Although decreasing with time, most sections remained within the "Fair" category for this parameter, with the exception of Section 7 which fell into the "Poor" category for the most recent loading campaign.

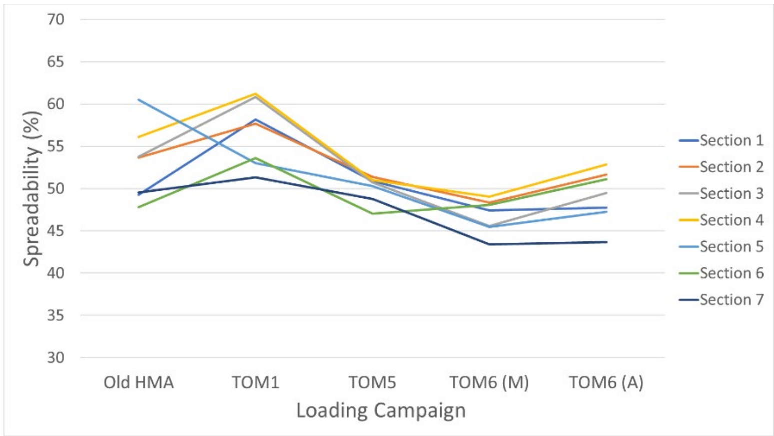

Figure 25: Spreadability Index of Pavement Sections

5.1.5 Base Damage Index (BDI)

Base Damage Index is computed as the slope between the third and fifth velocity transducer deflection measurement and pertains to the condition of the unbound pavement layers. A higher BDI is indicative of a comparatively weak base and subbase. Condition indices have not been reported based on this parameter, but Figure 26 shows the quantitative change in terms of BDI performance in each section over the first two years of the rehabilitated pavement life.

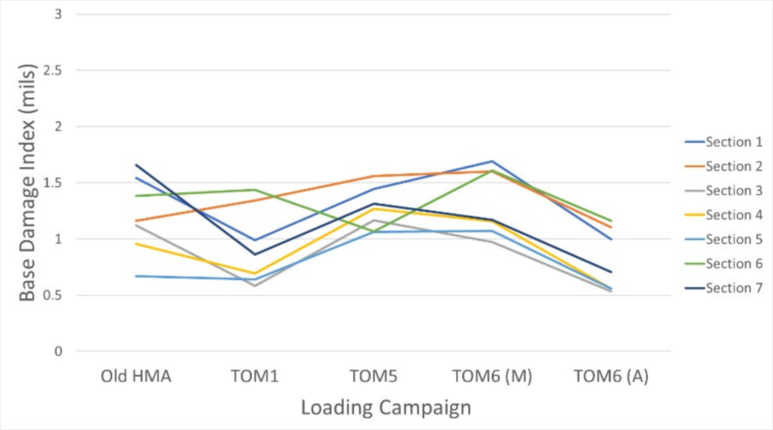

Figure 26: Base Damage Index (BDI) of Pavement Sections

Except for Sections 1, 2, and 6, the BDI appears fairly consistent across the different loading campaigns. The BDI does appear to be slightly lower in most sections during warmer pavement conditions, but it is not unexpected for slight variations in this parameter to be observed between loading campaigns, since it is primarily representative of the base and subbase stiffnesses which are both sensitive to changes in moisture content. Additionally, a temperature correction factor was applied to the first four deflection measurements, but not to the fifth, which could lead to some variation in this parameter with temperature as well. For Sections 1, 2, and 6, the BDI appears to increase slightly between TOM 5 and TOM 6, which is consistent with the weaker subgrade modulus in these sections in the last loading campaign as evidenced by the measured W7.

5.1.6 Summary of DBP Results

As discussed in section 5.1.2, Sections 1, 2, and 6 showed an apparent decrease in subgrade stiffness (likely due to moisture content of unbound materials) during the last loading campaign, as evidenced by increasing W7 and BDI. However, this did not seem to significantly affect the performance of the surface layer based on the SCI, or the overall flexural stiffness of the structure as measured through the Spreadability, since each of these parameters for Sections 1, 2 and 6 aligned closely with the behavior of the control section. The subgrade stiffness of other sections appeared to have decreased slightly during the last loading campaign, though not to the same degree as in these three sections. The BDI of sections other than 1, 2, and 6 appeared fairly consistent between the first and last loading campaigns on the rehabilitated pavement section. It is still too early in the life of the pavement to draw conclusions or make predictions on the future performance of the sections in terms of rate of damage accumulation at later stages in the pavement lifecycle. However, the fact that a larger increase in SCI was observed in Section 7 between first and last loading campaigns compared to other sections, coupled with the poor spreadability performance with minimal observed changes in BDI or W7 leaves the structural performance of the HMA in question and makes Section 7 a potential section of concern. Additional investigation is necessary to determine whether observations are similar at other locations in the outer lane of this test section, as well as to ascertain the reasoning behind this observed behavior.

5.2 Discussion of Sensor Malfunctions

One of the installed geophones appeared to have malfunctioned starting from the time of installation: The vertical sensor included in the 3D geophone assembly embedded in the base course at Section 7. Figure 27 shows the voltage-time history of this particular geophone for the duration of a single FWD test consisting of five drops, with the maximum deflections recorded by the geophones under the particular drop of interest (9,000 lbs) recorded in Table __. The deflection associated with the geophone embedded in the base course (2.995 mils) is highlighted in red in Table 6. This measurement is known to be errant due to the fact that it significantly less than the range of deflections measured by the geophone installed above in the HMA and below in the subgrade. Upon inspection of the raw voltage output of this particular geophone, it can be seen that the magnitude of the background noise is significantly higher than that observed in other geophones, which leads to inaccurate integration of the signal in the frequency domain. The source of this noise is unknown but may have been triggered by interaction between this particular geophone and the case assembly, or with other geophones inside the assembly. It is recommended that this case be removed and inspected to determine possible causes for this issue.

Table 6: Section 7 Maximum Deflections

Geophone Location Descriptor	Deflection (mils)
GPH_WP_HM_0_V1	9.726
GPH_WP_BC_0_V3	2.995
GPH_WP_SB_0_V1	7.173

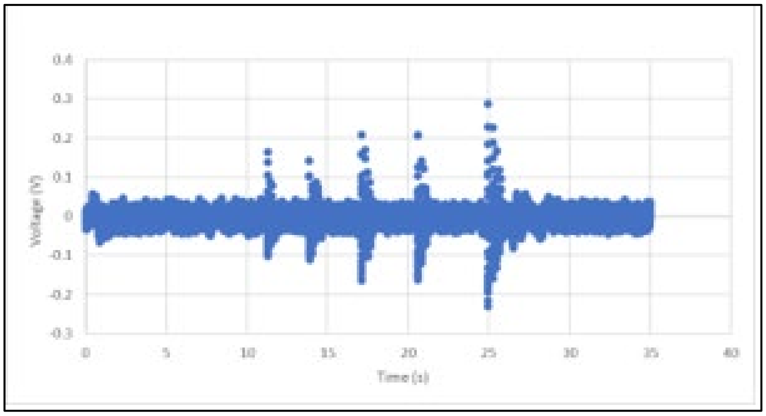

Figure 27: Malfunctioning 3D Geophone in Section 7

Several other geophones appeared to lose functionality over time. Figure 28 a) and b) shows the voltage-time histories of the geophones located in the base course and HMA in Section 4 during TOM 3. Figure 28 c) shows the voltage-time history of the geophone located in the base course in Section 2 during TOM 3.

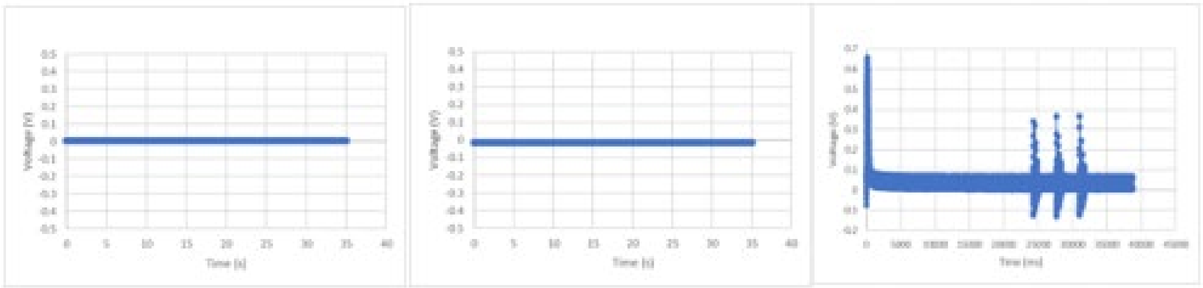

a) b) c)

Figure 28: Additional Malfunctioning Sensors in Sections 2 and 4; a) Section 4 Base Course, b) Section 4 HMA, c) Section 2 Base Course

In Section 4, the geophones are not even recording voltage measurements. It is unknown if this was caused by damage of the springs in the geophones due to torsional/twisting motions from free vibrations in the pavement, or if internal or external damage occurred to the wiring or external contacts. The issue with the sensor installed in the base material in Section 2 appears to be similar to that previously discussed for the geophone located in the base course in Section 7, with the magnitude of the background noise seemingly very large. There is also an abrupt jump in voltage prior to the actual FWD drops. It is also recommended that these geophones be removed and inspected at a later date to determine the cause of the issues experienced.

One additional anomalous measurement was identified in Section 3 during the first loading campaign. However, no issues were noticed from the voltage time history. In Table 7, The maximum deflections obtained by this geophone for an FWD drop location 10, which is supposed to be directly over the location of the three geophones is compared to the maximum deflections recorded at drop location 11, which is located one additional foot longitudinally in the direction of traffic from drop location 10. It is apparent that imprecision of FWD drop location is an issue in this case, since all of deflections recorded by these geophones are larger for the drop corresponding to location 11.

Table 7: Section 3 Maximum Deflections: a) Drop Location 10, b) Drop Location 11

Geophone Location Descriptor	Deflection (mils)
GPH_WP_HM_0_V1	5.067
GPH_WP_BC_0_V3	6.251
GPH_WP_SB_0_V1	5.779

a)

Geophone Location Descriptor	Deflection (mils)
GPH_WP_HM_0_V1	7.874
GPH_WP_BC_0_V3	8.519
GPH_WP_SB_0_V1	7.052

b)

The four malfunctioning geophones represent approximately 19 percent of all of the sensors used for this particular analysis as having failed within the two years of the life of the pavement. This suggests that the potential for loss of data and the need for redundancy are important factors to consider if geophones are to be used in future monitoring programs for the long-term in-situ evaluation of pavement performance.

5.3 Comparison between Predicted and Measured Deflections:

5.3.1 Overall Agreement of Predicted and Measured Deflections

As discussed in Chapter 4.2 and 4.3, separate backcalculations were performed in MODULUS 7.0 for each loading campaign, and with two separate section characterizations: one with a combined base and subbase, and one with a combined subbase and subgrade. The layer moduli corresponding to each individual backcalculation were then used in a forward calculation to generate a set of predicted depth deflections at the location of the geophones corresponding to each load campaign and section characterization. For the sake of brevity, these backcalculation and forward calculation results, as well as the predicted deflections, are included in the appendices. An analysis comparing the predicted deflections obtained through this process to the actual in-situ deflections measured by the geophones is presented in this section.

For the first two loading campaigns on the full rehabilitated pavement, the agreement between theoretical deflections predicted using layered elastic analysis with moduli obtained through FWD backcalculation to in-situ measured deflections was deemed to be good. Figure 29 a) represents the range of relative errors associated with all 114 individual sensor observations when a pavement section characterized by a combined base and subbase and at all load levels were considered. Figure 29 b) presents similar data but in terms of absolute error. From Figure 29, it can be seen that a relative error of less than 9 percent was measured for three quarters of the total observations. The several observed relative errors that were in excess of 16 percent corresponded to measurements in the base course of Section 3 and the subbase of Section 7 during TOM 1. Potential reasons for these occurrences are discussed in subsequent sections. The absolute error for 100 percent of observations (excluding a few statistical outliers) was also within a narrow range of -1.2 to +1.0 mils. This range of absolute error between predicted and measured deflections is significantly larger than the typical sensor accuracy of 5 percent or 0.1 mils reported by Bentsen et al. (1989), which suggests that the observed differences are due to either systematic error of the data collection process, or the inaccuracy of the elastostatic model in predicting the true behavior of pavements as opposed to inaccuracy of the sensors themselves. However, given the additional potential sources of error associated with the geophones being embedded in a pavement section as opposed to on a surface or shake table, these tolerances are deemed reasonable.

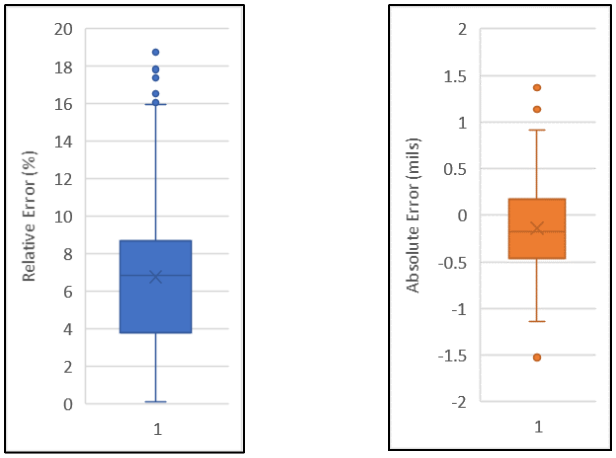

Figure 29: a) Relative Error of Predicted and Measured Deflections b) Absolute Error of Predicted and Measured Deflections

Figure 30 provides a further breakdown of the average absolute error results by load campaign and sensor location. The majority of the cases where the deflections are underpredicted (negative absolute error) involved the second loading campaign (Campaign TOM1), while the majority of cases where deflections were overpredicted correspond to the first loading campaign (Campaign Old HMA). This trend was generalized regardless of the sensor location. The largest discrepancy in either direction was observed in the sensors located in the HMA. This is consistent with the trends expected based on the previous discussion in Chapter 3.2 regarding the error associated with the precision of FWD drop location. This is because the HMA deflection is averaged between two drop locations and is also the most sensitive to the placement of the load plate due to the fact that for at least one of the drops, the sensor is located outside of the radial extents of the rigid plate.

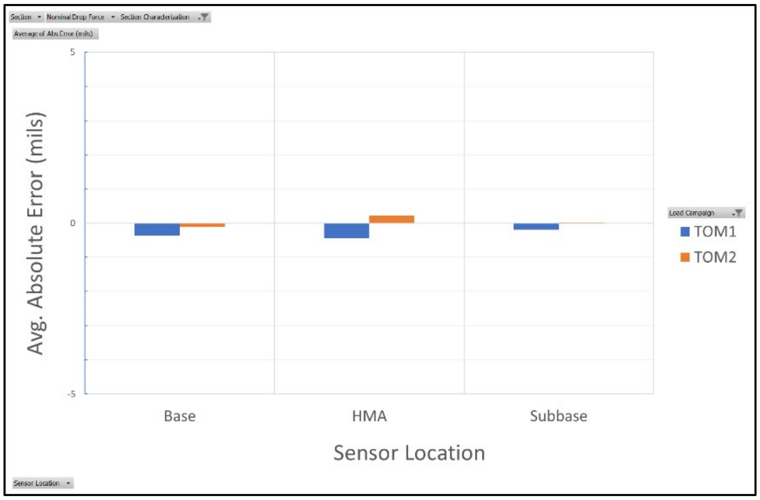

Figure 30: Average Sensor Error by Sensor Location

5.3.2 Effect of Force Magnitude

Figure 31 a) shows the average relative error per sensor as a function of drop force, and considering a section characterized by a combined base and subbase. During the first two loading campaigns on the full rehabilitated pavement section, the effect of increasing dynamic load imparted by the FWD was demonstrated to be a lower average relative error per sensor, as defined based on the equation below:

$$Avg.\ Relative\ Error\ per\ Sensor\ (\%) = \frac{\sum_{i=1}^{n}\left|100 * \frac{\delta_{pi}-\delta_{mi}}{\delta_{mi}}\right|}{n} = \frac{AASE}{n} \tag{8}$$

Where δ_{pi} is the predicted deflection obtained through layered elastic analysis, and δ_{mi} is the deflection measured by the geophone. The trend is consistent regardless of the section characterization. This is not the expected trend, as it was thought that increasing the dynamic drop force would heighten the effect of nonlinear response of unbound granular pavement layers and lead to backcalculation inaccuracy. Such trend was expected because the materials located immediately beneath the loading plate are subjected to larger vertical compressive loads than materials at increasing radial distances away, which also have an effect on the backcalculated moduli for these layers. However, it is now believed that the forces imparted by the FWD may not have been sufficient to induce nonlinear response from the unbound materials. In figure 31 b) the result for average relative error per sensor is further broken down by sensor location. The results in this figure show that the errors for the sensors located in the base and subbase layers do vary slightly with increasing load, but that the primary source of the overall observed reduction is due to measurements by the sensors in the HMA layer. While the reason for this reduction is unknown, it is possible that the observed reduction in average relative error per sensor with increasing load can primarily be attributed to the signal-to-noise ratio of the sensor. Since the magnitude of the background noise is constant, the ratio between the background noise picked up by the sensor and the actual measured deflection would be smaller under an increasingly large drop force. This might lead to more accurate backcalculation and thus better agreement between predicted and measured deflections.

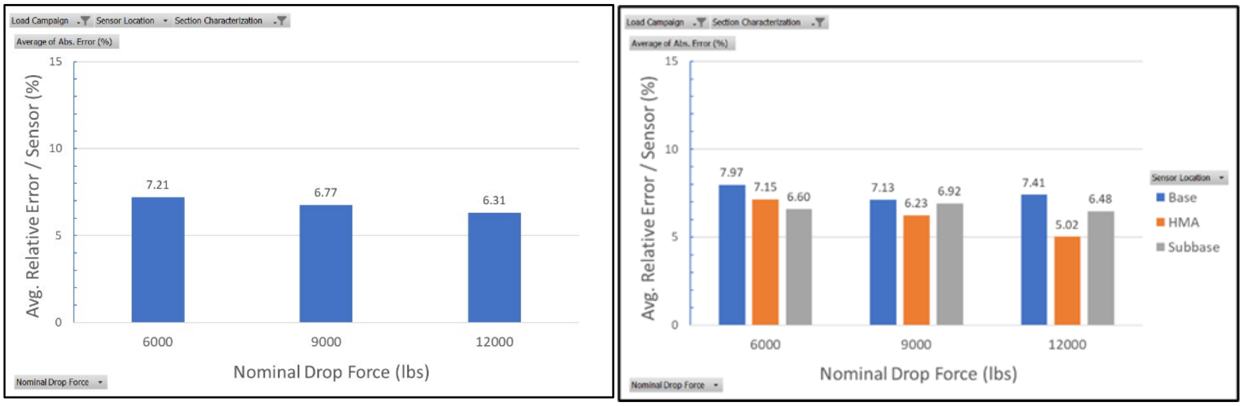

Figure 31: Effect of Force Magnitude on Deflection Prediction Accuracy: a) Average of All Sensor Locations, b) Broken Down by Sensor Location

At this point, the only conclusions that can be definitively drawn is that the average relative error per sensor decreased as a function of increasing load.

5.3.3 Effect of Temperature

Figure 32 a) compares the average relative error per sensor obtained during TOM 1 (avg. air temp of 91 degrees Fahrenheit) versus that obtained during TOM 2 (avg. air temp of 57 degrees Fahrenheit) for both section characterizations and for all nominal drop forces. Figure 32 b) further subdivides this into categories based on the section characterization and location of the sensor. Based on the results included in this figure, better agreement between predicted and measured deflections was obtained during hot conditions (TOM1) than during cold conditions (TOM2). However, an inspection of Figure 32 b) reveals that these overall results may be skewed by the observations made when considering a combined subbase and subgrade, where significant inaccuracies occurred between predicted and measure deflections (on the order of 15 to 20 percent) for sensors located in the HMA and Subbase. Still, the trend of better agreement between predicted and measured deflections at higher temperatures does seem to be generalized (with a few exceptions) across the different section characterizations and sensor locations. Similarly to the effect of increasing load, it is believed that the effect of increasing temperature might have a similar effect of causing better agreement between theoretical and measured deflections, since larger deflections are obtained at higher temperatures due to reduced HMA stiffness, which reduces the ratio between the background noise and velocity signal obtained by the geophone.

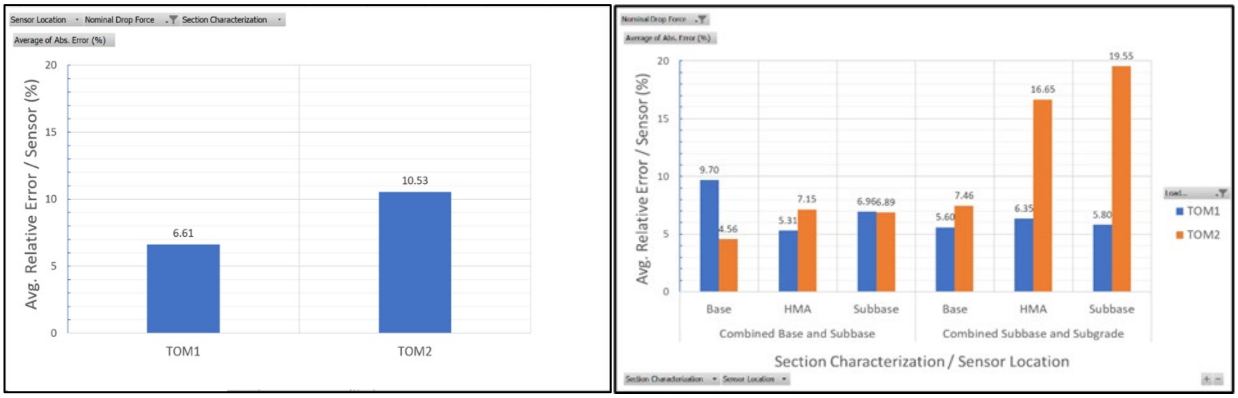

Figure 32: Effect of Pavement Temperature on Deflection Prediction Accuracy: a) Average of all Section Characterizations and Sensor Locations, b) Broken Down by Section Characterization and Sensor Location

5.3.4 Effect of Section Characterization (Combined Layers)

Figure 33 summarizes the effect of section characterization on the agreement between predicted and measured depth deflections with respect to two additional factors: sensor location and drop force. Other than a section characterized by a combined subbase and subgrade having a slight edge in terms of average relative error of the base sensors at all loading levels, it can be concluded from Figure 33 that combining the properties of the base and subbase in the backcalculation led to relative errors that were significantly better and within a more consistent range than when considering a combined subbase and subgrade. For the former case, average relative errors were consistently below 10 percent compared to averages exceeding 15 to 20 percent at times for the combined subbase and subgrade characterization. This is likely a situation where non-uniqueness of the deflection basin fitting optimization solution is an issue since both section characterizations yielded acceptable deflection basin fittings during the backcalculation process. These results suggest that even though an acceptable basin fitting was achieved in terms of low absolute error per sensor, deflections predicted using the moduli obtained do not necessarily predict representative strains and deformations adequately within the pavement under applied loading. Thus, the accuracy of backcalculation cannot be judged solely based on the goodness of fit between the theoretical and actual deflection basins.

It is plausible to assume that the reasoning behind the more consistent results being obtained for a section characterized by a combined base and subbase is that the cement treated base and flexible granular subbase are more closely related in material properties due to their course particle size distribution than the flexible granular base and high plasticity clay subgrade. Thus, if pavement layers need to be combined for a particular analysis, engineers should always choose to combine layers that consist of the materials with engineering properties that are as close of a match as possible.

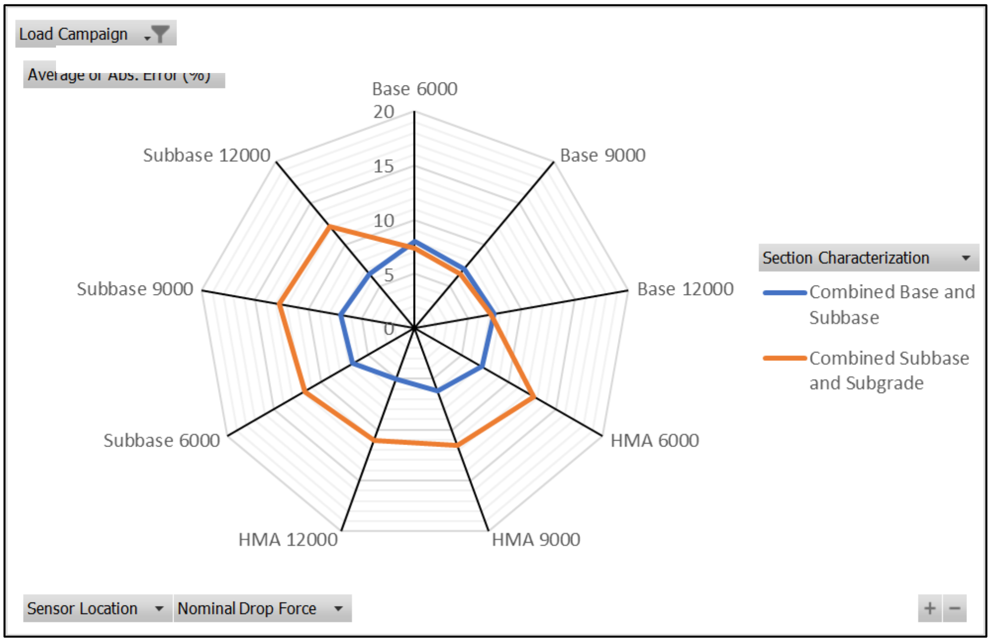

Figure 33: Effect of Pavement Section Characterization on Deflection Prediction Accuracy (Avg. Relative Error / Sensor)

5.3.5 Effect of the presence of Geosynthetic

The overall agreement between predicted and measured deflections as influenced by the geosynthetics reinforcements (or lack thereof) in each section is summarized in Figure 34 a) in terms of average relative error per sensor. Similar results are included in Figure 34 b), though the averages have been further broken out by loading campaign in addition to by section. From the overall results of the first two loading campaigns and assuming a section characterized by combined base and subbase properties as shown in Figure 34 a), there initially appears to be considerable differences between the average relative error between predicted and measured deflections within different sections. However, when the results are broken down between the two loading campaigns, it is evident that fairly similar overall averages would be obtained for all sections (approximately 4 to 6.5 percent), if it were not for the large discrepancies in Section 3 during TOM 1, Section 4 during TOM 2, and Section 7 during both loading campaigns. Based on the discussion of geophone malfunctions (Chapter 5.2) and observed anomalies in the deflection data, it is believed that the data corresponding to Section 3 and Section 4 on these days should be excluded from further analysis, since there is evidence that the drops at Location 10 in Section 3 were not in close enough proximity to the geophones, and since in the next subsequent loading campaign after TOM 2 the geophones located in the HMA and base of Section 4 stopped recording deflections altogether.

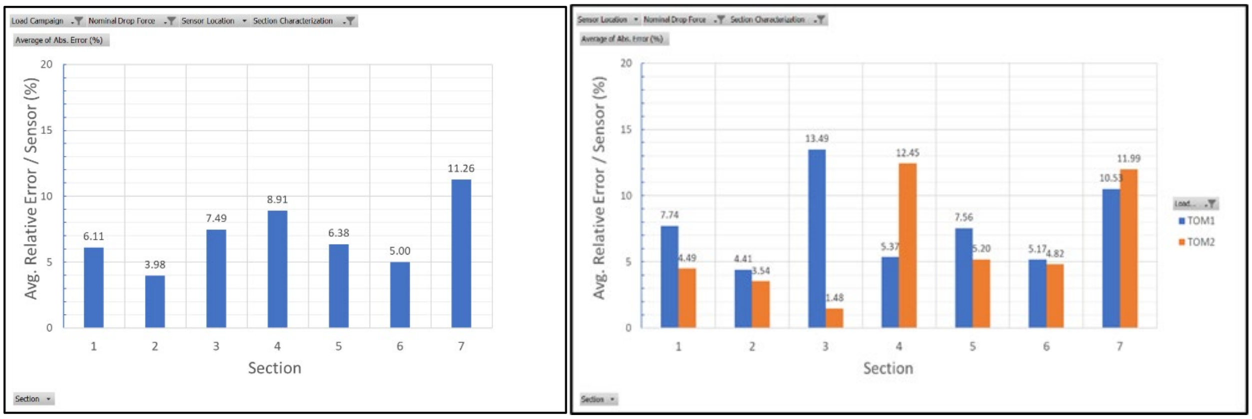

Figure 34: Effect of Geosynthetic Reinforcement on Deflection Prediction Accuracy: a) Average Relative Error per Sensor by Section, b) Section Results Broken Down between TOM 1 and TOM 2

Neglecting the anomalies associated with Section 3 and 4, the presence or absence of geosynthetics did not seem to significantly affect the overall accuracy in measurement of deflections from embedded geophones. The one exception to this may be in Section 7, where the average relative error per sensor exceeded 11 percent. From the DBP analysis, it is known that this also is the section where the largest SCI is and lowest spreadability were recorded during the first loading campaign. One hypothesis which ties the observed performance of this section in terms of deflection basin parameters to the lack of agreement between predicted and measured geophone deflections is the possibility of a significant departure from the non-zero slip condition in this section, since the backcalculation program assumes a rough (zero slip) interface condition between all pavement layers. The reason for the larger observed discrepancy in Section 7 should be further evaluated.

5.3.6 Effect of Time since Rehabilitation

Figure 35 a) displays the average relative error per sensor (considering a combined base and subbase) for a total of four loading campaigns: TOM 1 (shortly after rehabilitation, hot), TOM 2 (shortly after rehabilitation, cold), TOM 3 (1 year after rehabilitation, hot) and TOM 6 (2 years after rehabilitation, hot). Figure 35 b) further breaks down this average relative error for each loading campaign into the results for different sensor locations. When data from the one and two year mark since rehabilitation is incorporated into the analysis, it is clearly evident that the agreement between the predicted deflections and those measured through geophones deteriorates over time as displayed in Figure 35, even though testing procedures remained the same. The increase in average error is common across all sections where measurements were made, but the results shown in Figure 35 b) demonstrate that this trend is caused by increased error in the HMA and subbase measurements, and not due to increased error in base measurements. The cause of this apparent loss of accuracy over time is unknown and should be investigated, though it is not believed to be due to significant deterioration of pavement layer properties since this the deflection basin parameter analysis (see Chapter 5.1) did not indicate such significant degradation at least after only two years of service. One plausible explanation is that the representative calibration constants provided by the manufacturer have changed over time due to cyclic heating and cooling during the hot Texas summers, since the transfer function of the geophone is likely sensitive to the spring constant, the hardness of the resins and plastics making up the case assemblies, and other factors. Unfortunately, once the geophone is embedded in the roadway, there is no feasible way to recalibrate it in order to account for these factors. This hypothesis is supported by the fact that the largest deterioration in accuracy was observed for the sensors located in the HMA since this layer is subjected to the largest temperature fluctuations. However, it is unknown why the reduction in accuracy was greater in the subbase than in the base layer. What can definitively be concluded based on this study is that deflection accuracy was consistently lost over time, which has concerning implications for the usefulness of geophones as part of a long-term field monitoring program when embedded in the pavement since they cannot reasonably be inspected or recalibrated once installed.

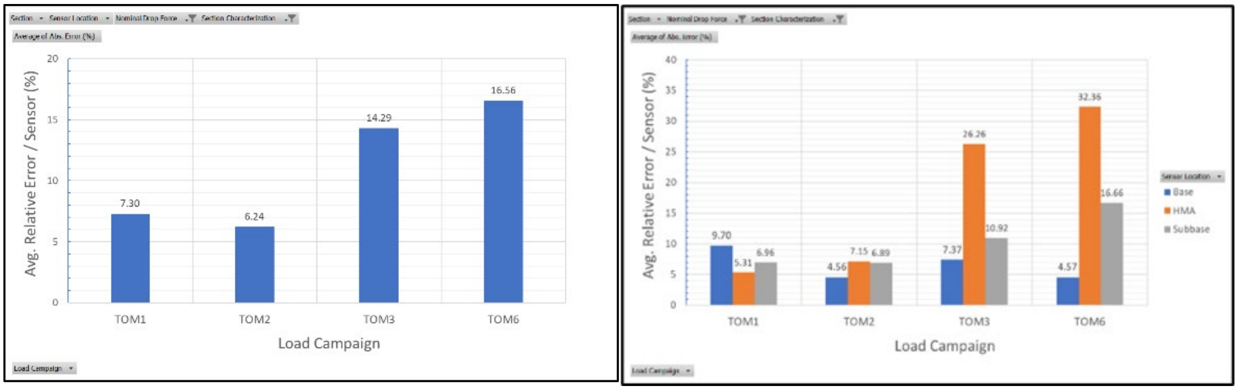

Figure 35: Effect of Time since Rehabilitation on Deflection Prediction Accuracy: a) Average Absolute Error per Sensor as a Function of Load Campaign, b) Results Further Broken Down by Sensor Location

Chapter 6: Conclusions

Raw output data from geophones embedded in an instrumented pavement section with six different geosynthetic reinforcements used as interlayers in the HMA were processed to determine deflections occurring at several depths within the pavement under FWD testing. This testing took place during loading campaigns that were conducted over the first two years of the rehabilitated pavement design life. The intent of the study was to use these measured deflections to assess the accuracy of elastostatic backcalculation, by comparing predicted deflections occurring within the pavement using backcalculated moduli and layered elastic theory to measured ones under similar loading.

This study has significant implications for the future use of geophones for field monitoring of pavements, and there are lessons that have been drawn regarding both the means of installation as well as the digital signal processing techniques used to obtain accurate deflections using geophones. Ultimately, key observations relate to implications regarding the accuracy of backcalculation based on a comparison of predicted and measured deflections within the pavement section.

Despite the common assumption that Geophones are a rugged and field-worthy sensor in comparison to others, Geophones are not immune from suffering damage or being compromised during or after installation. 19 percent of the sensors incorporated into the field program conducted in this study lost functionality within the first two years of pavement life. Redundancy and potential for data loss are factors that should be considered in any long-term field monitoring program. Installation methods likely play a significant role in performance over time, with a substantial amount of background noise being apparent in several of the 3D geophones, and other geophones losing their ability to record voltages altogether, likely due to damage to wiring or other vital components of the geophone structure. There is also evidence of reduced measurement accuracy over time, possibly due to cyclic heating and cooling of the geophone elements in the hot Texas climate causing changes to the transfer function or manufacturer’s provided calibration constants. Determining causes of these observed anomalies would require exhuming the geophones in these identified locations for further study.

Despite these issues, the geophones provided adequate deflection measurements when embedded in pavement, provided that the frequency response of the geophones and non-zero signal trends were accounted for prior to integration. In the first two loading campaigns (initial 3 months following sensor installation), and when a section characterized by a combined base and subbase were considered, the agreement between predicted and measured depth deflections was acceptable in all sections, with 75 percent of all observations having a relative error of less than 9 percent, and with the absolute error occurring within a range of -1.2 to +1.0 mils. However, the average absolute error per sensor increased significantly over time, with the largest errors observed during the last two loading campaigns included in the analysis. It is unknown if this effect can be primarily attributable to degradation of the pavement or to degradation in performance of the instrumentation. Continued monitoring and the results of future loading campaigns are expected to provide additional insight on this effect.

The agreement between predicted (theoretical) and measured deflections was typically better for sensors located in the base and subbase than for sensors located in the HMA, particularly for the last two loading campaigns analyzed in this study. Combining the characteristics of the base and subbase in a 3-layer system yielded a better agreement between predicted and measured deflections, even though deflection basin fitting during the backcalculation process was satisfactory for both characterizations. Designers and analysts should be wary of the possibility for non-uniqueness of solution in deflection basin fitting, particularly if pavement layers are being combined into a single layer for the purpose of analysis. If pavement layers need to be combined, they should consist of the materials with as close of a match as possible in engineering properties.

Deflection basin parameters based on load normalized and temperature corrected deflections provided a useful means of comparing performance of the different subsections over the first two years of the pavement life. However, with only two years after rehabilitation, it is still too early in the life of the pavement to draw final conclusions regarding trends and to predict the performance of the different sections in terms of rate of damage accumulation at later stages in the pavement lifecycle. However, the fact that a larger increase in SCI was observed in Section 7 between first and last loading campaigns compared to other sections, coupled with the poor spreadability performance with minimal observed changes in BDI or W7 leaves the structural performance of the HMA in question and makes Section 7 a potential section of concern. Due to the small number of drop locations analyzed, additional investigation is necessary to determine whether observations are similar at other locations in the outer lane of this test section, as well as to begin to ascertain the reasoning for this poor spreadability and SCI performance relative to the other sections. Additionally, the baseline spreadability of the Old HMA and overlay in the control section immediately following rehabilitation was highest but compared more closely with the spreadability of several of the reinforced sections two years following rehabilitation, which may provide early indication of a possible effect of geosynthetic reinforcement in slowing the degradation of pavement flexural rigidity. This potential effect should also continue to be investigated over the course of the overlay design life through nondestructive testing and and/or routine PCI surveys.

Overall, the comparison between predicted deflections at depth based on the analysis of conventional FWD data based on surficial information and measured deflections using geophones installed within the pavement section indicates good agreement between predicted and measured deflections, which supports the notion that conventional FWD backcalculation techniques using surface deflections can be used to define structural properties of pavement layers that can then be used as input in mechanistic-empirical design. However, the apparent accuracy of conventional backcalculation as assessed by geophones embedded in the pavement decreased significantly within the first two years of pavement life. Further study is necessary to determine whether the observed drop is due to degradation of the geophones themselves, or due to a real observed effect caused by deterioration of the pavement.

Appendix A: Python Code

```
# Frequency Response Method for Determination of Deflections using Geophone Voltage Output
"""
Created on Fri Aug 27, 2021

@author: Benjamin Weaver
"""

### PRIMARY FUNCTIONS ###

#Define Frequency Response Function of geophones as high-pass Butterworth Filter(D=0.707) based on geophone-
specific natl frequency and calibration constants
def g_frf(fn, fs, x, tc, geo):
  b,a=butter(2, fn, btype='high', fs=fs)
  w,h=freqz(b,a=a, worN=x*2*math.pi/fs)
  return pd.DataFrame(h*tc, columns=[geo])

#Define trend in output displacement signal by fitting 6th order polynomial based on determined fitting coeffic
ients
def trend(a, b, c, d, e, f, g, ts, name):
    return pd.DataFrame(a*ts**6+b*ts**5+c*ts**4+d*ts**3+e*ts**2+f*ts+g, columns=[name])



### Main Program Starts ###
file_path = '/content/gdrive/MyDrive/2_ASG_GP_Resp/Section5/8_2021-09-02_FWD_Test_on_TOM_layer_6/'
file_name = 'F5.11.csv'

#Create list of columns to read from CSV File
columns = [0]+list(np.arange(1,32,2))

# Read data from file
gph = pd.read_csv(file_path + file_name,
                  skiprows=[0,1,3],
                  usecols=columns,
                  )
# Rename Columns
gph.drop(gph.loc[:, 'GPH_WP_HM_2_V1':'GPH_M_HMA_5_V1'], axis=1, inplace=True)
gph.drop(gph.loc[:, 'GPH_WP_BC_0_H1':'GPH_WP_BC_0_H2'], axis=1, inplace=True)
gph.rename(columns={'Channel name': 'Time', 'GPH_WP_SB_0_V1':12725, 'GPH_WP_BC_0_V3':10373, 'GPH_WP_HM_0_V1':12
732}, inplace=True)
gph.drop(gph.loc[:, 'ASG_Ex_Volt':'ASG_LM'], axis=1, inplace=True)
gph.set_index('Time', inplace=True)

#Frequency Response Function Matrix for Test Section
geo=[12732, 10373, 12725]#geophone serial numbers for test section of interest
fs=1000 #sampling frequency, Hz
fn=[4.33, 4.28, 4.63] #natural frequency, Hz
tc=[27.58, 26.53, 27.31] #transduction constant, V/m/s
length=512 #volt_spectrum.shape[0]
df=(fs/2)/(length/2) #frequency bin size
x1=np.linspace(0, (fs/2)-df, length//2) #creates an array of frequencies up to folding frequency
x2=np.linspace(-(fs/2), -df, length//2) #creates array of negative frequencies
x=np.concatenate((x1, x2))
if 'frf' in globals():
  del frf
for g,nf,ct in zip(geo,fn,tc):
  temp=g_frf(nf,fs,x,ct, g)
  if 'frf' in globals():
    frf=pd.concat([frf,temp], axis=1)
  else:
    frf=temp

#define integration operator in Frequency Domain, (jw)
w=(2j*math.pi*x)
int_op=pd.DataFrame(w, columns={12732}) #creates the integration operator
int_op[10373]=int_op[12732]
int_op[12725]=int_op[12732]

#Get label of Channel with largest response
max_ch = gph.max().idxmax()

# Find local maxima
n=1000  # 1 second
gph_max = gph[max_ch].iloc[argrelextrema(gph[max_ch].values, np.greater_equal, order=n)[0]]
gph_max = gph_max[gph_max > gph_max.max()/10]
```

```python
###Signal Correction###

drop_vel=[]
drop_volt=[]
drop_disp=[]
volt_spectrum=[]
Actual_Volt_Spectrum=[]
disp_spectrum=[]
disp_time=[]
max_disp=[]

for i in range(len(gph_max.index)):
  drop_volt.append(gph.loc[gph_max.index[i]-0.05:gph_max.index[i]+.15])#defines drop voltage matrix for a single drop
  drop_volt[i]=pd.DataFrame(drop_volt[i])
  drop_volt[i]=drop_volt[i].sub(drop_volt[i].mean(axis=0), axis=1) #subtract mean from drop voltage signal
  df=pd.DataFrame(np.zeros((512-len(drop_volt[i]),3)), columns=drop_volt[i].columns) #creates dataframe of zeros to be appended to voltage signal
  drop_volt[i]=pd.concat([drop_volt[i],df],axis=0, ignore_index=True) #appends zero dataframe df to raw voltage signal
  volt_spectrum.append(drop_volt[i].apply(fft, axis=0, raw=True)) #defines voltage spectrum matrix for single drop
  Actual_Volt_Spectrum.append(volt_spectrum[i].div(frf)) #defines actual voltage spectrum matrix for single drop by dividing by frf matrix
  disp_spectrum.append(Actual_Volt_Spectrum[i].div(int_op)) #defines actual displacement spectrm matrix for single drop by dividing by integration operator
  disp_spectrum[i].loc[0]=[0, 0, 0] #sets first row of displacement spectrum to zero
  disp_time.append(disp_spectrum[i].apply(ifft, axis=0, raw=True)) #defies displacement_time matrix for single drop by ifft of disp spectrum
  disp_time[i]= disp_time[i]*39370.079 #converts disp_time matrix from meters to mils
  disp_time[i].index = np.linspace(0, 0.425, 512) #sets disp_time matrix index on scale from 0 to 0.425 seconds

  #define portion of disp_time series that should be equal to zero in dataframe temp3
  mask = (disp_time[i].index <= 0.04)
  mask2 = (disp_time[i].index >=0.2125)
  temp1=disp_time[i].loc[mask]
  temp2=disp_time[i].loc[mask2]
  temp3=pd.DataFrame(temp1.append(temp2))

  #fit 6th order polynomial to the curves where disp_time series should be zero
  a=[]
  b=[]
  c=[]
  d=[]
  e=[]
  f=[]
  g=[]
  ts=np.array(disp_time[i].index)
  name=np.array(disp_time[i].columns)
  for j in range(0, 3):
    xdata=np.array(temp3.index)
    ydata=temp3[temp3.columns[j]]
    #perform polyfit
    fit=np.polyfit(xdata, ydata, 6) #fits 6th order polynomial to time series data that shoudl be zero
    a.append(fit[0])
    b.append(fit[1])
    c.append(fit[2])
    d.append(fit[3])
    e.append(fit[4])
    f.append(fit[5])
    g.append(fit[6])
  if 'sig_trend' in globals():
    del sig_trend
  for name_i,a_i,b_i,c_i,d_i,e_i,f_i,g_i in zip(name, a, b, c, d, e, f, g):
    temp4=trend(a_i,b_i,c_i,d_i,e_i,f_i,g_i,ts,name_i)
    if 'sig_trend' in globals():
      sig_trend=pd.concat([sig_trend,temp4], axis=1)
    else:
      sig_trend=pd.DataFrame(temp4)
  sig_trend.index=np.linspace(0, 0.425, 512)

  disp_time[i]=disp_time[i].subtract(sig_trend) #subtracts nonlinear trend from displacement_time signal
  disp_time[i]=disp_time[i].apply(np.real, raw=True)
  max_disp.append(disp_time[i].max(axis=0))
  print(max_disp[i]) #Prints maximum ground deflection measured for each geophone, during each dro
```

Appendix B: Backcalculation Results

Loading Campaign	Section Characterization	Drop Force (lbs)	Nominal Drop Force (lbs)	Mean Pavement Temperature (F)	Section	Drop Location	HMA Thickness (in.)	Base Thickness (in.)	Subgrade Thickness	HMA Seed Moduli Range (ksi)	Base Seed Moduli Range (ksi)	Subgrade Most Likely Modulus (ksi)	HMA Modulus (ksi)	Base Modulus (ksi)	Subgrade Modulus (ksi)	Abs. Error / Sensor (%)
TOM 1	Combined Base and Subbase	6167	6000	120.84	1	1.10	9	15	Semi-infinite	50 - 375	10 - 200	5	193.9	40.9	24.2	0.79
TOM 1	Combined Base and Subbase	9213	9000	120.84	1	1.10	9	15	Semi-infinite	50 - 375	10 - 200	5	205.8	34	23.6	0.74
TOM 1	Combined Base and Subbase	12170	12000	120.84	1	1.10	9	15	Semi-infinite	50 - 375	10 - 200	5	209.6	29.6	22.4	0.89
TOM 1	Combined Base and Subbase	6134	6000	119.83	2	2.10	8.19	15	Semi-infinite	50 - 375	10 - 200	5	248.9	41	24.3	0.69
TOM 1	Combined Base and Subbase	9278	9000	119.83	2	2.10	8.19	15	Semi-infinite	50 - 375	10 - 200	5	276.2	41.9	23.1	0.77
TOM 1	Combined Base and Subbase	12236	12000	119.83	2	2.10	8.19	15	Semi-infinite	50 - 375	10 - 200	5	282.8	41.4	22.1	0.48
TOM 1	Combined Base and Subbase	6266	6000	125.57	3	3.10	8.46	15.5	Semi-infinite	50 - 375	10 - 200	5	355.7	37.5	25.2	2.01
TOM 1	Combined Base and Subbase	9311	9000	125.57	3	3.10	8.46	15.5	Semi-infinite	50 - 375	10 - 200	5	350.6	35.5	23.4	1.4
TOM 1	Combined Base and Subbase	12368	12000	125.57	3	3.10	8.46	15.5	Semi-infinite	50 - 375	10 - 200	5	361.4	32.6	22.8	1.11
TOM 1	Combined Base and Subbase	6244	6000	117.41	4	4.10	8.69	16	Semi-infinite	50 - 375	10 - 200	5	230.5	53.4	25.4	1.16
TOM 1	Combined Base and Subbase	9267	9000	117.41	4	4.10	8.69	16	Semi-infinite	50 - 375	10 - 200	5	251.2	46.6	23.9	0.76
TOM 1	Combined Base and Subbase	12203	12000	117.41	4	4.10	8.69	16	Semi-infinite	50 - 375	10 - 200	5	254.7	44.2	22.9	0.56
TOM 1	Combined Base and Subbase	6365	6000	113.6	5	5.10	8.53	16	Semi-infinite	50 - 375	10 - 200	5	277.8	63.8	33.7	3.79
TOM 1	Combined Base and Subbase	9366	9000	113.6	5	5.10	8.53	16	Semi-infinite	50 - 375	10 - 200	5	289.1	58.6	32.8	2.85
TOM 1	Combined Base and Subbase	12324	12000	113.6	5	5.10	8.53	16	Semi-infinite	50 - 375	10 - 200	5	301	57.7	31.1	2.32
TOM 1	Combined Base and Subbase	6299	6000	114.36	6	6.10	7.91	19	Semi-infinite	50 - 375	10 - 200	5	273.7	42.6	26	0.4
TOM 1	Combined Base and Subbase	9289	9000	114.36	6	6.10	7.91	19	Semi-infinite	50 - 375	10 - 200	5	294	38.7	24.8	0.51
TOM 1	Combined Base and Subbase	12269	12000	114.36	6	6.10	7.91	19	Semi-infinite	50 - 375	10 - 200	5	302.5	36.8	23.3	0.45
TOM 1	Combined Base and Subbase	6288	6000	120.27	7	7.10	7.56	19.5	Semi-infinite	50 - 375	10 - 200	5	215.4	50.4	27.1	0.31
TOM 1	Combined Base and Subbase	9355	9000	120.27	7	7.10	7.56	19.5	Semi-infinite	50 - 375	10 - 200	5	230.2	45.1	26.1	0.53
TOM 1	Combined Base and Subbase	12192	12000	120.27	7	7.10	7.56	19.5	Semi-infinite	50 - 375	10 - 200	5	256.7	41.8	24.5	0.8
TOM 2	Combined Base and Subbase	6233	6000	54.54	1	1.10	9	15	Semi-infinite	510-1330	10 - 200	5	1061.1	70.1	26.9	0.59
TOM 2	Combined Base and Subbase	9344	9000	54.54	1	1.10	9	15	Semi-infinite	510-1330	10 - 200	5	958.1	64.8	25.6	0.39
TOM 2	Combined Base and Subbase	12729	12000	54.54	1	1.10	9	15	Semi-infinite	510-1330	10 - 200	5	926.5	60	25.8	0.45
TOM 2	Combined Base and Subbase	6288	6000	40.54	2	2.10	8.19	15	Semi-infinite	510-1330	10 - 200	5	1003.4	36.9	30.5	2.36
TOM 2	Combined Base and Subbase	9432	9000	40.54	2	2.10	8.19	15	Semi-infinite	510-1330	10 - 200	5	891.2	50.4	25	0.79
TOM 2	Combined Base and Subbase	13003	12000	40.54	2	2.10	8.19	15	Semi-infinite	510-1330	10 - 200	5	972	49.1	25.3	0.93
TOM 2	Combined Base and Subbase	6354	6000	38	3	3.10	8.46	15.5	Semi-infinite	510-1330	10 - 200	5	899.1	70.8	26.3	1.82
TOM 2	Combined Base and Subbase	9410	9000	38	3	3.10	8.46	15.5	Semi-infinite	510-1330	10 - 200	5	946.3	71.6	24.4	1.03
TOM 2	Combined Base and Subbase	12926	12000	38	3	3.10	8.46	15.5	Semi-infinite	510-1330	10 - 200	5	990	64.6	24.9	1.08
TOM 2	Combined Base and Subbase	6397	6000	60.01	4	4.10	8.69	16	Semi-infinite	510-1330	10 - 200	5	1008.7	87.2	27	1.06
TOM 2	Combined Base and Subbase	9497	9000	60.01	4	4.10	8.69	16	Semi-infinite	510-1330	10 - 200	5	1330	51.2	27.1	2.75
TOM 2	Combined Base and Subbase	12926	12000	60.01	4	4.10	8.69	16	Semi-infinite	510-1330	10 - 200	5	1178.4	71.6	25.9	0.73
TOM 2	Combined Base and Subbase	6507	6000	58.43	5	5.10	8.53	16	Semi-infinite	510-1330	10 - 200	5	740.2	95.8	36.5	1.78
TOM 2	Combined Base and Subbase	9596	9000	58.43	5	5.10	8.53	16	Semi-infinite	510-1330	10 - 200	5	836.8	86.3	34.7	1.23
TOM 2	Combined Base and Subbase	13200	12000	58.43	5	5.10	8.53	16	Semi-infinite	510-1330	10 - 200	5	841.2	86.4	34.8	1.34
TOM 2	Combined Base and Subbase	6551	6000	50.85	6	6.10	7.91	19	Semi-infinite	510-1330	10 - 200	5	889.4	57.2	28.7	0.92
TOM 2	Combined Base and Subbase	9541	9000	50.85	6	6.10	7.91	19	Semi-infinite	510-1330	10 - 200	5	949.9	49.3	27.4	0.23
TOM 2	Combined Base and Subbase	13080	12000	50.85	6	6.10	7.91	19	Semi-infinite	510-1330	10 - 200	5	974.7	49.2	27.4	0.39
TOM 2	Combined Base and Subbase	6354	6000	48.61	7	7.10	7.56	19.5	Semi-infinite	510-1330	10 - 200	5	841.9	55.6	28.2	1.97
TOM 2	Combined Base and Subbase	9432	9000	48.61	7	7.10	7.56	19.5	Semi-infinite	510-1330	10 - 200	5	852.2	49.5	27.9	1.2
TOM 2	Combined Base and Subbase	12970	12000	48.61	7	7.10	7.56	19.5	Semi-infinite	510-1330	10 - 200	5	916.6	48.7	27.6	1.05
TOM3	Combined Base and Subbase	9322	9000	109.2	1	1.10	9	15	Semi-infinite	50 - 375	10 - 200	5	239.3	38.7	24.3	0.79
TOM3	Combined Base and Subbase	9311	9000	108.79	2	2.10	8.19	15	Semi-infinite	50 - 375	10 - 200	5	298.6	53.5	24	0.73
TOM3	Combined Base and Subbase	9421	9000	116.92	3	3.10	8.46	15.5	Semi-infinite	50 - 375	10 - 200	5	271.5	51.3	23.8	0.19
TOM3	Combined Base and Subbase	9388	9000	126.26	4	4.10	8.69	16	Semi-infinite	50 - 375	10 - 200	5	293.5	55.7	24.6	1.39
TOM3	Combined Base and Subbase	9454	9000	129.09	5	5.10	8.53	16	Semi-infinite	50 - 375	10 - 200	5	246.7	69.1	33.1	3.51
TOM3	Combined Base and Subbase	9388	9000	137.18	6	6.10	7.91	16	Semi-infinite	50 - 375	10 - 200	5	212.1	45.7	25.6	0.93
TOM3	Combined Base and Subbase	9454	9000	129.84	7	7.10	7.56	19.5	Semi-infinite	50 - 375	10 - 200	5	143	57.4	26.3	0.83
TOM6	Combined Base and Subbase	9837	9000	100.06	1	1.10	9	15	Semi-infinite	50 - 375	10 - 200	5	189	35.9	23.4	1.26
TOM6	Combined Base and Subbase	9870	9000	99.71	2	2.10	8.19	15	Semi-infinite	50 - 375	10 - 200	5	242.3	57.4	25.1	0.81
TOM6	Combined Base and Subbase	9837	9000	106.52	3	3.10	8.46	15.5	Semi-infinite	50 - 375	10 - 200	5	150.7	62.2	23.2	0.37
TOM6	Combined Base and Subbase	9881	9000	108.17	4	4.10	8.69	16	Semi-infinite	50 - 375	10 - 200	5	152.5	64	23.6	0.29
TOM6	Combined Base and Subbase	9859	9000	108.72	5	5.10	8.53	16	Semi-infinite	50 - 375	10 - 200	5	138	83.6	32.9	2.05
TOM6	Combined Base and Subbase	9815	9000	113.24	6	6.10	7.91	16	Semi-infinite	50 - 375	10 - 200	5	144.9	59	26	1.29
TOM6	Combined Base and Subbase	9771	9000	115.39	7	7.10	7.56	19.5	Semi-infinite	50 - 375	10 - 200	5	86.4	76	25.5	1.66
TOM 1	Combined Subbase and Subgrade	6167	6000	120.84	1	1.10	9	6	Semi-infinite	50 - 375	10 - 200	10	177.9	78.8	24.7	1.62
TOM 1	Combined Subbase and Subgrade	9213	9000	120.84	1	1.10	9	6	Semi-infinite	50 - 375	10 - 200	10	192	56.3	23.7	0.86
TOM 1	Combined Subbase and Subgrade	12170	12000	120.84	1	1.10	9	6	Semi-infinite	50 - 375	10 - 200	10	197.8	44.5	22.5	3.12
TOM 1	Combined Subbase and Subgrade	6134	6000	119.83	2	2.10	8.19	6	Semi-infinite	50 - 375	10 - 200	10	214.5	86.3	24.8	0.96
TOM 1	Combined Subbase and Subgrade	9278	9000	119.83	2	2.10	8.19	6	Semi-infinite	50 - 375	10 - 200	10	237.3	89.6	23.6	1.25
TOM 1	Combined Subbase and Subgrade	12236	12000	119.83	2	2.10	8.19	6	Semi-infinite	50 - 375	10 - 200	10	237.4	95.1	22.6	3
TOM 1	Combined Subbase and Subgrade	6266	6000	125.57	3	3.10	8.46	6.5	Semi-infinite	50 - 375	10 - 200	10	339.4	58	25.4	2.59
TOM 1	Combined Subbase and Subgrade	9311	9000	125.57	3	3.10	8.46	6.5	Semi-infinite	50 - 375	10 - 200	10	329.3	57.9	23.6	1.97
TOM 1	Combined Subbase and Subgrade	12368	12000	125.57	3	3.10	8.46	6.5	Semi-infinite	50 - 375	10 - 200	10	345.3	49.8	22.9	1.59
TOM 1	Combined Subbase and Subgrade	6244	6000	117.41	4	4.10	8.69	6	Semi-infinite	50 - 375	10 - 200	10	197	143	26.6	2.84
TOM 1	Combined Subbase and Subgrade	9267	9000	117.41	4	4.10	8.69	6	Semi-infinite	50 - 375	10 - 200	10	219.5	111.3	24.8	2.12
TOM 1	Combined Subbase and Subgrade	12203	12000	117.41	4	4.10	8.69	6	Semi-infinite	50 - 375	10 - 200	10	221.4	104.3	23.6	1.8
TOM 1	Combined Subbase and Subgrade	6365	6000	113.6	5	5.10	8.53	7	Semi-infinite	50 - 375	10 - 200	10	262.1	103.7	35.8	4.44
TOM 1	Combined Subbase and Subgrade	9366	9000	113.6	5	5.10	8.53	7	Semi-infinite	50 - 375	10 - 200	10	268.6	100.6	33.6	3.98
TOM 1	Combined Subbase and Subgrade	12324	12000	113.6	5	5.10	8.53	7	Semi-infinite	50 - 375	10 - 200	10	280.9	100.6	32	3.48
TOM 1	Combined Subbase and Subgrade	6299	6000	114.36	6	6.10	7.91	7	Semi-infinite	50 - 375	10 - 200	10	231.5	85.4	26.6	1.21
TOM 1	Combined Subbase and Subgrade	9289	9000	114.36	6	6.10	7.91	7	Semi-infinite	50 - 375	10 - 200	10	248.1	74.4	25.1	0.47
TOM 1	Combined Subbase and Subgrade	12269	12000	114.36	6	6.10	7.91	7	Semi-infinite	50 - 375	10 - 200	10	254.1	72.3	23.6	0.61
TOM 1	Combined Subbase and Subgrade	6288	6000	120.27	7	7.10	7.56	7.5	Semi-infinite	50 - 375	10 - 200	10	175.6	107.7	28.2	2.27
TOM 1	Combined Subbase and Subgrade	9355	9000	120.27	7	7.10	7.56	7.5	Semi-infinite	50 - 375	10 - 200	10	189.3	91.3	26.9	1.22
TOM 1	Combined Subbase and Subgrade	12192	12000	120.27	7	7.10	7.56	7.5	Semi-infinite	50 - 375	10 - 200	10	206.6	87.6	25.2	0.75
TOM 2	Combined Subbase and Subgrade	6233	6000	54.54	1	1.10	9	6	Semi-infinite	510-1330	10 - 200	10	963.7	200	27.9	1.12
TOM 2	Combined Subbase and Subgrade	9344	9000	54.54	1	1.10	9	6	Semi-infinite	510-1330	10 - 200	10	828.1	200	26.5	0.54
TOM 2	Combined Subbase and Subgrade	12729	12000	54.54	1	1.10	9	6	Semi-infinite	510-1330	10 - 200	10	777.3	190.7	26.5	0.44
TOM 2	Combined Subbase and Subgrade	6288	6000	40.54	2	2.10	8.19	6	Semi-infinite	510-1330	10 - 200	10	927.8	62.2	30.2	2.3
TOM 2	Combined Subbase and Subgrade	9432	9000	40.54	2	2.10	8.19	6	Semi-infinite	510-1330	10 - 200	10	715.6	155.8	25.5	0.28
TOM 2	Combined Subbase and Subgrade	13003	12000	40.54	2	2.10	8.19	6	Semi-infinite	510-1330	10 - 200	10	797.1	145.1	25.7	0.51
TOM 2	Combined Subbase and Subgrade	6354	6000	38	3	3.10	8.46	6.5	Semi-infinite	510-1330	10 - 200	10	771.1	200	27.5	1.45
TOM 2	Combined Subbase and Subgrade	9410	9000	38	3	3.10	8.46	6.5	Semi-infinite	510-1330	10 - 200	10	836.2	200	25.6	1.2
TOM 2	Combined Subbase and Subgrade	12926	12000	38	3	3.10	8.46	6.5	Semi-infinite	510-1330	10 - 200	10	806.4	200	25.8	0.76
TOM 2	Combined Subbase and Subgrade	6397	6000	60.01	4	4.10	8.69	6	Semi-infinite	510-1330	10 - 200	10	1100.4	200	29	2.43
TOM 2	Combined Subbase and Subgrade	9497	9000	60.01	4	4.10	8.69	6	Semi-infinite	510-1330	10 - 200	10	1330	200	27.9	2.86
TOM 2	Combined Subbase and Subgrade	12926	12000	60.01	4	4.10	8.69	6	Semi-infinite	510-1330	10 - 200	10	1330	112.3	27.8	2.19
TOM 2	Combined Subbase and Subgrade	6507	6000	58.43	5	5.10	8.53	7	Semi-infinite	510-1330	10 - 200	10	704.3	200	38.4	3.04
TOM 2	Combined Subbase and Subgrade	9596	9000	58.43	5	5.10	8.53	7	Semi-infinite	510-1330	10 - 200	10	748.1	200	36.3	2.22
TOM 2	Combined Subbase and Subgrade	13200	12000	58.43	5	5.10	8.53	7	Semi-infinite	510-1330	10 - 200	10	751.5	200	36.4	2.33
TOM 2	Combined Subbase and Subgrade	6551	6000	50.85	6	6.10	7.91	7	Semi-infinite	510-1330	10 - 200	10	765.6	142.8	29.9	1.7
TOM 2	Combined Subbase and Subgrade	9541	9000	50.85	6	6.10	7.91	7	Semi-infinite	510-1330	10 - 200	10	812.2	119.7	28.3	0.88
TOM 2	Combined Subbase and Subgrade	13080	12000	50.85	6	6.10	7.91	7	Semi-infinite	510-1330	10 - 200	10	843.4	117.5	28	0.83
TOM 2	Combined Subbase and Subgrade	6354	6000	48.61	7	7.10	7.56	7.5	Semi-infinite	510-1330	10 - 200	10	722.3	127.5	29.4	2.51
TOM 2	Combined Subbase and Subgrade	9432	9000	48.61	7	7.10	7.56	7.5	Semi-infinite	510-1330	10 - 200	10	737.7	106.2	28.7	1.54
TOM 2	Combined Subbase and Subgrade	12970	12000	48.61	7	7.10	7.56	7.5	Semi-infinite	510-1330	10 - 200	10	792.4	106.1	28.3	1.33
TOM3	Combined Subbase and Subgrade	9322	9000	109.2	1	1.10	9	6	Semi-infinite	50 - 375	10 - 200	10	218.4	73.2	24.7	1.01
TOM3	Combined Subbase and Subgrade	9311	9000	108.79	2	2.10	8.19	6	Semi-infinite	50 - 375	10 - 200	10	239.4	148.5	24.9	1.16
TOM3	Combined Subbase and Subgrade	9421	9000	116.92	3	3.10	8.46	6.5	Semi-infinite	50 - 375	10 - 200	10	227.9	123.5	24.6	1.44
TOM3	Combined Subbase and Subgrade	9388	9000	126.26	4	4.10	8.69	6	Semi-infinite	50 - 375	10 - 200	10	249.8	150.9	25.6	2.54
TOM3	Combined Subbase and Subgrade	9454	9000	129.09	5	5.10	8.53	7	Semi-infinite	50 - 375	10 - 200	10	226	130.9	34.5	4.76
TOM3	Combined Subbase and Subgrade	9388	9000	137.18	6	6.10	7.91	7	Semi-infinite	50 - 375	10 - 200	10	181.9	88.5	26.2	1.04
TOM3	Combined Subbase and Subgrade	9454	9000	129.84	7	7.10	7.56	7.5	Semi-infinite	50 - 375	10 - 200	10	158	110.7	27.7	1.99
TOM6	Combined Subbase and Subgrade	9837	9000	100.06	1	1.10	9	6	Semi-infinite	50 - 375	10 - 200	10	172.2	65.9	23.7	1.37
TOM6	Combined Subbase and Subgrade	9870	9000	99.71	2	2.10	8.19	6	Semi-infinite	50 - 375	10 - 200	10	192.3	179.8	26.3	0.99
TOM6	Combined Subbase and Subgrade	9837	9000	106.52	3	3.10	8.46	6.5	Semi-infinite	50 - 375	10 - 200	10	124.3	200	24.5	1.95
TOM6	Combined Subbase and Subgrade	9881	9000	108.17	4	4.10	8.69	6	Semi-infinite	50 - 375	10 - 200	10	133.9	200	25.3	2.5
TOM6	Combined Subbase and Subgrade	9859	9000	108.72	5	5.10	8.53	7	Semi-infinite	50 - 375	10 - 200	10	122.5	200	34.5	4.23
TOM6	Combined Subbase and Subgrade	9815	9000	113.24	6	6.10	7.91	7	Semi-infinite	50 - 375	10 - 200	10	117.4	153.5	27.1	0.98
TOM6	Combined Subbase and Subgrade	9771	9000	115.39	7	7.10	7.56	7.5	Semi-infinite	50 - 375	10 - 200	10	77.9	200	27.7	3.83

Appendix C: Predicted Versus Measured Deflections

Load Campaign	Date	Section Characterization	Section	Sensor Location	Nominal Drop Force (lbf)	Normalized Deflection (mils)	Predicted Deflection (mils)	Abs Error (mils)	Relative Error (%)
TOM1	10/15/2019	Combined Base and Subbase	1	HMA	6000	6.35	5.76	-0.58	9.19
TOM1	10/15/2019	Combined Base and Subbase	1	Base	6000	5.43	4.98	-0.45	8.28
TOM1	10/15/2019	Combined Base and Subbase	1	Subbase	6000	3.83	4.16	0.34	8.83
TOM1	10/15/2019	Combined Base and Subbase	1	HMA	9000	9.87	9.17	-0.71	7.15
TOM1	10/15/2019	Combined Base and Subbase	1	Base	9000	8.55	7.87	-0.68	7.93
TOM1	10/15/2019	Combined Base and Subbase	1	Subbase	9000	6.01	6.50	0.49	8.13
TOM1	10/15/2019	Combined Base and Subbase	1	HMA	12000	12.93	13.03	0.11	0.82
TOM1	10/15/2019	Combined Base and Subbase	1	Base	12000	12.18	11.15	-1.03	8.49
TOM1	10/15/2019	Combined Base and Subbase	1	Subbase	12000	8.64	9.15	0.51	5.88
TOM1	10/15/2019	Combined Base and Subbase	2	HMA	6000	6.09	5.73	-0.36	5.84
TOM1	10/15/2019	Combined Base and Subbase	2	Base	6000	5.41	4.90	-0.52	9.57
TOM1	10/15/2019	Combined Base and Subbase	2	Subbase	6000	4.17	4.11	-0.06	1.33
TOM1	10/15/2019	Combined Base and Subbase	2	HMA	9000	8.93	8.58	-0.35	3.92
TOM1	10/15/2019	Combined Base and Subbase	2	Base	9000	8.04	7.40	-0.65	8.05
TOM1	10/15/2019	Combined Base and Subbase	2	Subbase	9000	6.37	6.29	-0.08	1.25
TOM1	10/15/2019	Combined Base and Subbase	2	HMA	12000	12.14	11.69	-0.46	3.76
TOM1	10/15/2019	Combined Base and Subbase	2	Base	12000	11.18	10.11	-1.07	9.57
TOM1	10/15/2019	Combined Base and Subbase	2	Subbase	12000	8.78	8.64	-0.14	1.64
TOM1	10/15/2019	Combined Base and Subbase	3	HMA	6000		5.26		
TOM1	10/15/2019	Combined Base and Subbase	3	Base	6000	3.84	4.51	0.67	17.40
TOM1	10/15/2019	Combined Base and Subbase	3	Subbase	6000	3.49	3.80	0.30	8.63
TOM1	10/15/2019	Combined Base and Subbase	3	HMA	9000		8.34		
TOM1	10/15/2019	Combined Base and Subbase	3	Base	9000	6.03	7.17	1.13	18.76
TOM1	10/15/2019	Combined Base and Subbase	3	Subbase	9000	5.60	6.06	0.46	8.22
TOM1	10/15/2019	Combined Base and Subbase	3	HMA	12000		11.47		
TOM1	10/15/2019	Combined Base and Subbase	3	Base	12000	8.46	9.83	1.37	16.19
TOM1	10/15/2019	Combined Base and Subbase	3	Subbase	12000	7.93	8.29	0.36	4.57
TOM1	10/15/2019	Combined Base and Subbase	4	HMA	6000	5.74	5.05	-0.69	12.04
TOM1	10/15/2019	Combined Base and Subbase	4	Base	6000	4.91	4.42	-0.49	9.90
TOM1	10/15/2019	Combined Base and Subbase	4	Subbase	6000	3.81	3.76	-0.04	1.12
TOM1	10/15/2019	Combined Base and Subbase	4	HMA	9000	8.74	8.03	-0.72	8.21

TOM1	10/15/2019	Combined Base and Subbase	4	Base	9000	7.62	7.03	-0.59	7.81
TOM1	10/15/2019	Combined Base and Subbase	4	Subbase	9000	5.96	5.97	0.01	0.09
TOM1	10/15/2019	Combined Base and Subbase	4	HMA	12000	12.07	11.08	-0.99	8.17
TOM1	10/15/2019	Combined Base and Subbase	4	Base	12000	10.69	9.71	-0.98	9.16
TOM1	10/15/2019	Combined Base and Subbase	4	Subbase	12000	8.39	8.25	-0.14	1.61
TOM1	10/15/2019	Combined Base and Subbase	5	HMA	6000	4.44	4.18	-0.26	5.92
TOM1	10/15/2019	Combined Base and Subbase	5	Base	6000	3.86	3.60	-0.27	6.92
TOM1	10/15/2019	Combined Base and Subbase	5	Subbase	6000	3.20	3.02	-0.18	5.62
TOM1	10/15/2019	Combined Base and Subbase	5	HMA	9000	6.71	6.27	-0.44	6.56
TOM1	10/15/2019	Combined Base and Subbase	5	Base	9000	5.88	5.39	-0.49	8.30
TOM1	10/15/2019	Combined Base and Subbase	5	Subbase	9000	4.91	4.53	-0.38	7.80
TOM1	10/15/2019	Combined Base and Subbase	5	HMA	12000	9.06	8.55	-0.51	5.61
TOM1	10/15/2019	Combined Base and Subbase	5	Base	12000	8.04	7.39	-0.65	8.06
TOM1	10/15/2019	Combined Base and Subbase	5	Subbase	12000	6.80	6.24	-0.56	8.22
TOM1	10/15/2019	Combined Base and Subbase	6	HMA	6000	5.55	5.36	-0.19	3.51
TOM1	10/15/2019	Combined Base and Subbase	6	Base	6000	4.94	4.52	-0.41	8.38
TOM1	10/15/2019	Combined Base and Subbase	6	Subbase	6000	4.10	3.76	-0.34	8.20
TOM1	10/15/2019	Combined Base and Subbase	6	HMA	9000	8.51	8.38	-0.13	1.51
TOM1	10/15/2019	Combined Base and Subbase	6	Base	9000	7.64	7.08	-0.56	7.32
TOM1	10/15/2019	Combined Base and Subbase	6	Subbase	9000	6.31	5.89	-0.42	6.69
TOM1	10/15/2019	Combined Base and Subbase	6	HMA	12000	11.69	11.63	-0.06	0.48
TOM1	10/15/2019	Combined Base and Subbase	6	Base	12000	10.66	9.86	-0.80	7.49
TOM1	10/15/2019	Combined Base and Subbase	6	Subbase	12000	8.95	8.24	-0.71	7.92
TOM1	10/15/2019	Combined Base and Subbase	7	HMA	6000	5.77	5.25	-0.52	9.05
TOM1	10/15/2019	Combined Base and Subbase	7	Base	6000		4.43		
TOM1	10/15/2019	Combined Base and Subbase	7	Subbase	6000	4.47	3.67	-0.80	17.83
TOM1	10/15/2019	Combined Base and Subbase	7	HMA	9000	8.67	8.28	-0.39	4.52
TOM1	10/15/2019	Combined Base and Subbase	7	Base	9000		6.97		
TOM1	10/15/2019	Combined Base and Subbase	7	Subbase	9000	6.90	5.76	-1.14	16.53
TOM1	10/15/2019	Combined Base and Subbase	7	HMA	12000	11.99	11.47	-0.52	4.37
TOM1	10/15/2019	Combined Base and Subbase	7	Base	12000		9.69		
TOM1	10/15/2019	Combined Base and Subbase	7	Subbase	12000	9.57	8.04	-1.53	15.96
TOM1	10/15/2019	Combined Subbase and Subgrade	1	HMA	6000	6.35	5.66	-0.69	10.85
TOM1	10/15/2019	Combined Subbase and Subgrade	1	Base	6000	5.43	5.24	-0.19	3.56
TOM1	10/15/2019	Combined Subbase and Subgrade	1	Subbase	6000	3.83	4.20	0.37	9.73
TOM1	10/15/2019	Combined Subbase and Subgrade	1	HMA	9000	9.87	9.07	-0.80	8.13

TOM1	10/15/2019	Combined Subbase and Subgrade	1	Base	9000	8.55	8.24	-0.31	3.61
TOM1	10/15/2019	Combined Subbase and Subgrade	1	Subbase	9000	6.01	6.59	0.58	9.72
TOM1	10/15/2019	Combined Subbase and Subgrade	1	HMA	12000	12.97	12.90	-0.07	0.52
TOM1	10/15/2019	Combined Subbase and Subgrade	1	Base	12000	12.18	11.56	-0.62	5.12
TOM1	10/15/2019	Combined Subbase and Subgrade	1	Subbase	12000	8.64	9.26	0.62	7.13
TOM1	10/15/2019	Combined Subbase and Subgrade	2	HMA	6000	6.09	5.61	-0.48	7.88
TOM1	10/15/2019	Combined Subbase and Subgrade	2	Base	6000	5.41	5.17	-0.24	4.42
TOM1	10/15/2019	Combined Subbase and Subgrade	2	Subbase	6000	4.17	4.12	-0.05	1.21
TOM1	10/15/2019	Combined Subbase and Subgrade	2	HMA	9000	8.93	8.49	-0.44	4.90
TOM1	10/15/2019	Combined Subbase and Subgrade	2	Base	9000	8.04	7.88	-0.16	2.04
TOM1	10/15/2019	Combined Subbase and Subgrade	2	Subbase	9000	6.37	6.32	-0.05	0.77
TOM1	10/15/2019	Combined Subbase and Subgrade	2	HMA	12000	12.14	11.54	-0.60	4.94
TOM1	10/15/2019	Combined Subbase and Subgrade	2	Base	12000	11.18	10.78	-0.41	3.64
TOM1	10/15/2019	Combined Subbase and Subgrade	2	Subbase	12000	8.78	8.67	-0.11	1.27
TOM1	10/15/2019	Combined Subbase and Subgrade	3	HMA	6000		5.25		
TOM1	10/15/2019	Combined Subbase and Subgrade	3	Base	6000	3.84	4.73	0.89	23.10
TOM1	10/15/2019	Combined Subbase and Subgrade	3	Subbase	6000	3.49	3.84	0.35	9.88
TOM1	10/15/2019	Combined Subbase and Subgrade	3	HMA	9000		8.31		
TOM1	10/15/2019	Combined Subbase and Subgrade	3	Base	9000	6.03	7.52	1.49	24.67
TOM1	10/15/2019	Combined Subbase and Subgrade	3	Subbase	9000	5.60	6.13	0.53	9.40
TOM1	10/15/2019	Combined Subbase and Subgrade	3	HMA	12000		11.44		
TOM1	10/15/2019	Combined Subbase and Subgrade	3	Base	12000	8.46	10.28	1.82	21.45
TOM1	10/15/2019	Combined Subbase and Subgrade	3	Subbase	12000	7.93	8.39	0.46	5.83
TOM1	10/15/2019	Combined Subbase and Subgrade	4	HMA	6000	5.74	4.89	-0.85	14.80
TOM1	10/15/2019	Combined Subbase and Subgrade	4	Base	6000	4.91	4.67	-0.24	4.80
TOM1	10/15/2019	Combined Subbase and Subgrade	4	Subbase	6000	3.81	3.79	-0.02	0.51
TOM1	10/15/2019	Combined Subbase and Subgrade	4	HMA	9000	8.74	7.85	-0.89	10.17
TOM1	10/15/2019	Combined Subbase and Subgrade	4	Base	9000	7.62	7.43	-0.19	2.47
TOM1	10/15/2019	Combined Subbase and Subgrade	4	Subbase	9000	5.96	6.02	0.06	0.94
TOM1	10/15/2019	Combined Subbase and Subgrade	4	HMA	12000	12.07	10.92	-1.15	9.53
TOM1	10/15/2019	Combined Subbase and Subgrade	4	Base	12000	10.69	10.32	-0.37	3.43
TOM1	10/15/2019	Combined Subbase and Subgrade	4	Subbase	12000	8.39	8.37	-0.02	0.24
TOM1	10/15/2019	Combined Subbase and Subgrade	5	HMA	6000	4.44	3.95	-0.49	10.94
TOM1	10/15/2019	Combined Subbase and Subgrade	5	Base	6000	3.86	3.62	-0.24	6.26
TOM1	10/15/2019	Combined Subbase and Subgrade	5	Subbase	6000	3.20	2.92	-0.28	8.74
TOM1	10/15/2019	Combined Subbase and Subgrade	5	HMA	9000	6.71	6.38	-0.33	4.86

TOM1	10/15/2019	Combined Subbase and Subgrade	5	Base	9000	5.88	5.88	0.00	0.00
TOM1	10/15/2019	Combined Subbase and Subgrade	5	Subbase	9000	4.91	4.77	-0.14	2.84
TOM1	10/15/2019	Combined Subbase and Subgrade	5	HMA	12000	9.06	8.44	-0.61	6.79
TOM1	10/15/2019	Combined Subbase and Subgrade	5	Base	12000	8.04	7.78	-0.26	3.22
TOM1	10/15/2019	Combined Subbase and Subgrade	5	Subbase	12000	6.80	6.32	-0.48	7.09
TOM1	10/15/2019	Combined Subbase and Subgrade	6	HMA	6000	5.55	5.25	-0.30	5.49
TOM1	10/15/2019	Combined Subbase and Subgrade	6	Base	6000	4.94	4.82	-0.11	2.27
TOM1	10/15/2019	Combined Subbase and Subgrade	6	Subbase	6000	4.10	3.87	-0.22	5.45
TOM1	10/15/2019	Combined Subbase and Subgrade	6	HMA	9000	8.51	8.29	-0.22	2.61
TOM1	10/15/2019	Combined Subbase and Subgrade	6	Base	9000	7.64	7.58	-0.06	0.81
TOM1	10/15/2019	Combined Subbase and Subgrade	6	Subbase	9000	6.31	6.10	-0.21	3.39
TOM1	10/15/2019	Combined Subbase and Subgrade	6	HMA	12000	11.69	11.51	-0.18	1.50
TOM1	10/15/2019	Combined Subbase and Subgrade	6	Base	12000	10.66	10.55	-0.10	0.96
TOM1	10/15/2019	Combined Subbase and Subgrade	6	Subbase	12000	8.95	8.52	-0.42	4.71
TOM1	10/15/2019	Combined Subbase and Subgrade	7	HMA	6000	5.77	5.07	-0.70	12.16
TOM1	10/15/2019	Combined Subbase and Subgrade	7	Base	6000		4.73		
TOM1	10/15/2019	Combined Subbase and Subgrade	7	Subbase	6000	4.47	3.81	-0.66	14.80
TOM1	10/15/2019	Combined Subbase and Subgrade	7	HMA	9000	8.67	8.03	-0.65	7.44
TOM1	10/15/2019	Combined Subbase and Subgrade	7	Base	9000		7.42		
TOM1	10/15/2019	Combined Subbase and Subgrade	7	Subbase	9000	6.90	5.96	-0.94	13.57
TOM1	10/15/2019	Combined Subbase and Subgrade	7	HMA	12000	11.99	11.11	-0.88	7.37
TOM1	10/15/2019	Combined Subbase and Subgrade	7	Base	12000		10.28		
TOM1	10/15/2019	Combined Subbase and Subgrade	7	Subbase	12000	9.57	8.30	-1.26	13.22
TOM2	12/19/2020	Combined Base and Subbase	1	HMA	6000	3.42	3.30	-0.11	3.30
TOM2	12/19/2020	Combined Base and Subbase	1	Base	6000	3.24	3.03	-0.21	6.38
TOM2	12/19/2020	Combined Base and Subbase	1	Subbase	6000	2.58	2.74	0.15	5.94
TOM2	12/19/2020	Combined Base and Subbase	1	HMA	9000	5.30	5.30	0.00	0.07
TOM2	12/19/2020	Combined Base and Subbase	1	Base	9000	5.05	4.85	-0.20	3.87
TOM2	12/19/2020	Combined Base and Subbase	1	Subbase	9000	3.99	4.37	0.38	9.53
TOM2	12/19/2020	Combined Base and Subbase	1	HMA	12000	7.23	7.21	-0.03	0.37
TOM2	12/19/2020	Combined Base and Subbase	1	Base	12000	6.88	6.57	-0.31	4.45
TOM2	12/19/2020	Combined Base and Subbase	1	Subbase	12000	5.44	5.89	0.45	8.28
TOM2	12/19/2020	Combined Base and Subbase	2	HMA	6000	3.90	3.84	-0.06	1.58
TOM2	12/19/2020	Combined Base and Subbase	2	Base	6000	3.53	3.32	-0.21	5.91
TOM2	12/19/2020	Combined Base and Subbase	2	Subbase	6000	2.88	2.84	-0.04	1.44
TOM2	12/19/2020	Combined Base and Subbase	2	HMA	9000	5.97	6.13	0.17	2.79

TOM2	12/19/2020	Combined Base and Subbase	2	Base	9000	5.50	5.47	-0.02	0.44
TOM2	12/19/2020	Combined Base and Subbase	2	Subbase	9000	4.51	4.85	0.33	7.40
TOM2	12/19/2020	Combined Base and Subbase	2	HMA	12000	7.84	8.01	0.17	2.22
TOM2	12/19/2020	Combined Base and Subbase	2	Base	12000	7.31	7.15	-0.16	2.18
TOM2	12/19/2020	Combined Base and Subbase	2	Subbase	12000	6.08	6.34	0.25	4.19
TOM2	12/19/2020	Combined Base and Subbase	3	HMA	6000		3.64		
TOM2	12/19/2020	Combined Base and Subbase	3	Base	6000	3.27	3.27	0.01	0.22
TOM2	12/19/2020	Combined Base and Subbase	3	Subbase	6000	2.83	2.94	0.11	3.85
TOM2	12/19/2020	Combined Base and Subbase	3	HMA	9000		5.51		
TOM2	12/19/2020	Combined Base and Subbase	3	Base	9000	5.07	5.01	-0.06	1.15
TOM2	12/19/2020	Combined Base and Subbase	3	Subbase	9000	4.46	4.54	0.08	1.81
TOM2	12/19/2020	Combined Base and Subbase	3	HMA	12000		7.37		
TOM2	12/19/2020	Combined Base and Subbase	3	Base	12000	6.80	6.68	-0.13	1.88
TOM2	12/19/2020	Combined Base and Subbase	3	Subbase	12000	6.05	6.02	-0.04	0.58
TOM2	12/19/2020	Combined Base and Subbase	4	HMA	6000	2.83	3.20	0.37	13.09
TOM2	12/19/2020	Combined Base and Subbase	4	Base	6000	2.72	2.95	0.23	8.27
TOM2	12/19/2020	Combined Base and Subbase	4	Subbase	6000	2.38	2.67	0.29	12.08
TOM2	12/19/2020	Combined Base and Subbase	4	HMA	9000	4.37	5.08	0.70	16.05
TOM2	12/19/2020	Combined Base and Subbase	4	Base	9000	4.22	4.62	0.40	9.49
TOM2	12/19/2020	Combined Base and Subbase	4	Subbase	9000	3.69	4.12	0.43	11.80
TOM2	12/19/2020	Combined Base and Subbase	4	HMA	12000	5.88	6.65	0.76	12.98
TOM2	12/19/2020	Combined Base and Subbase	4	Base	12000	5.67	6.11	0.43	7.65
TOM2	12/19/2020	Combined Base and Subbase	4	Subbase	12000	5.00	5.53	0.54	10.72
TOM2	12/19/2020	Combined Base and Subbase	5	HMA	6000	3.05	2.85	-0.21	6.76
TOM2	12/19/2020	Combined Base and Subbase	5	Base	6000	2.79	2.55	-0.24	8.47
TOM2	12/19/2020	Combined Base and Subbase	5	Subbase	6000	2.34	2.25	-0.09	3.79
TOM2	12/19/2020	Combined Base and Subbase	5	HMA	9000	4.64	4.41	-0.23	5.02
TOM2	12/19/2020	Combined Base and Subbase	5	Base	9000	4.25	3.95	-0.29	6.88
TOM2	12/19/2020	Combined Base and Subbase	5	Subbase	9000	3.64	3.50	-0.13	3.71
TOM2	12/19/2020	Combined Base and Subbase	5	HMA	12000	6.15	5.86	-0.29	4.78
TOM2	12/19/2020	Combined Base and Subbase	5	Base	12000	5.64	5.26	-0.39	6.86
TOM2	12/19/2020	Combined Base and Subbase	5	Subbase	12000	4.86	4.66	-0.21	4.26
TOM2	12/19/2020	Combined Base and Subbase	6	HMA	6000	3.52	3.65	0.14	3.96
TOM2	12/19/2020	Combined Base and Subbase	6	Base	6000	3.42	3.22	-0.20	5.96
TOM2	12/19/2020	Combined Base and Subbase	6	Subbase	6000	2.92	2.81	-0.11	3.75
TOM2	12/19/2020	Combined Base and Subbase	6	HMA	9000	5.49	5.77	0.28	5.14

TOM2	12/19/2020	Combined Base and Subbase	6	Base	9000	5.37	5.07	-0.30	5.55
TOM2	12/19/2020	Combined Base and Subbase	6	Subbase	9000	4.60	4.43	-0.17	3.78
TOM2	12/19/2020	Combined Base and Subbase	6	HMA	12000	7.37	7.65	0.28	3.73
TOM2	12/19/2020	Combined Base and Subbase	6	Base	12000	7.23	6.73	-0.50	6.90
TOM2	12/19/2020	Combined Base and Subbase	6	Subbase	12000	6.22	5.88	-0.33	5.39
TOM2	12/19/2020	Combined Base and Subbase	7	HMA	6000	3.46	3.86	0.40	11.53
TOM2	12/19/2020	Combined Base and Subbase	7	Base	6000		3.38		
TOM2	12/19/2020	Combined Base and Subbase	7	Subbase	6000	3.27	2.94	-0.33	10.03
TOM2	12/19/2020	Combined Base and Subbase	7	HMA	9000	5.29	6.02	0.73	13.81
TOM2	12/19/2020	Combined Base and Subbase	7	Base	9000		5.25		
TOM2	12/19/2020	Combined Base and Subbase	7	Subbase	9000	5.05	4.54	-0.51	10.18
TOM2	12/19/2020	Combined Base and Subbase	7	HMA	12000	7.06	7.98	0.92	12.97
TOM2	12/19/2020	Combined Base and Subbase	7	Base	12000		6.97		
TOM2	12/19/2020	Combined Base and Subbase	7	Subbase	12000	6.84	6.05	-0.79	11.55
TOM3	9/16/2020	Combined Base and Subbase	1	HMA	9000	8.95	10.64	1.69	18.84
TOM3	9/16/2020	Combined Base and Subbase	1	Base	9000	7.64	8.41	0.77	10.11
TOM3	9/16/2020	Combined Base and Subbase	1	Subbase	9000	5.45	7.29	1.83	33.62
TOM3	9/16/2020	Combined Base and Subbase	2	HMA	9000		9.55		
TOM3	9/16/2020	Combined Base and Subbase	2	Base	9000		7.69		
TOM3	9/16/2020	Combined Base and Subbase	2	Subbase	9000	7.35	6.73	-0.62	8.41
TOM3	9/16/2020	Combined Base and Subbase	3	HMA	9000		9.80		
TOM3	9/16/2020	Combined Base and Subbase	3	Base	9000	7.01	7.78	0.77	11.05
TOM3	9/16/2020	Combined Base and Subbase	3	Subbase	9000	6.15	6.79	0.64	10.33
TOM3	9/16/2020	Combined Base and Subbase	4	HMA	9000		9.05		
TOM3	9/16/2020	Combined Base and Subbase	4	Base	9000		7.26		
TOM3	9/16/2020	Combined Base and Subbase	4	Subbase	9000		6.43		
TOM3	9/16/2020	Combined Base and Subbase	5	HMA	9000	6.47	8.16	1.69	26.11
TOM3	9/16/2020	Combined Base and Subbase	5	Base	9000	5.79	6.07	0.28	4.85
TOM3	9/16/2020	Combined Base and Subbase	5	Subbase	9000	4.92	5.25	0.33	6.76
TOM3	9/16/2020	Combined Base and Subbase	6	HMA	9000	8.95	10.83	1.88	21.01
TOM3	9/16/2020	Combined Base and Subbase	6	Base	9000	7.97	8.24	0.28	3.48
TOM3	9/16/2020	Combined Base and Subbase	6	Subbase	9000	6.55	6.96	0.41	6.26
TOM3	9/16/2020	Combined Base and Subbase	7	HMA	9000	8.33	11.58	3.25	39.08
TOM3	9/16/2020	Combined Base and Subbase	7	Base	9000		8.05		
TOM3	9/16/2020	Combined Base and Subbase	7	Subbase	9000	6.81	6.82	0.01	0.16
TOM3	9/16/2020	Combined Subbase and Subgrade	1	HMA	9000	8.95	10.59	1.64	18.34

TOM3	9/16/2020	Combined Subbase and Subgrade	1	Base	9000	7.64	8.26	0.63	8.20
TOM3	9/16/2020	Combined Subbase and Subgrade	1	Subbase	9000	5.45	7.63	2.17	39.82
TOM3	9/16/2020	Combined Subbase and Subgrade	2	HMA	9000		9.60		
TOM3	9/16/2020	Combined Subbase and Subgrade	2	Base	9000		7.53		
TOM3	9/16/2020	Combined Subbase and Subgrade	2	Subbase	9000	7.35	7.17	-0.17	2.36
TOM3	9/16/2020	Combined Subbase and Subgrade	3	HMA	9000		9.81		
TOM3	9/16/2020	Combined Subbase and Subgrade	3	Base	9000	7.01	7.63	0.62	8.84
TOM3	9/16/2020	Combined Subbase and Subgrade	3	Subbase	9000	6.15	7.22	1.07	17.35
TOM3	9/16/2020	Combined Subbase and Subgrade	4	HMA	9000		9.09		
TOM3	9/16/2020	Combined Subbase and Subgrade	4	Base	9000		7.16		
TOM3	9/16/2020	Combined Subbase and Subgrade	4	Subbase	9000		6.86		
TOM3	9/16/2020	Combined Subbase and Subgrade	5	HMA	9000	6.47	8.11	1.63	25.25
TOM3	9/16/2020	Combined Subbase and Subgrade	5	Base	9000	5.79	5.96	0.17	2.97
TOM3	9/16/2020	Combined Subbase and Subgrade	5	Subbase	9000	4.92	5.56	0.64	12.97
TOM3	9/16/2020	Combined Subbase and Subgrade	6	HMA	9000	8.95	10.96	2.01	22.43
TOM3	9/16/2020	Combined Subbase and Subgrade	6	Base	9000	7.97	8.20	0.24	2.96
TOM3	9/16/2020	Combined Subbase and Subgrade	6	Subbase	9000	6.55	7.57	1.03	15.68
TOM3	9/16/2020	Combined Subbase and Subgrade	7	HMA	9000	8.33	10.79	2.46	29.51
TOM3	9/16/2020	Combined Subbase and Subgrade	7	Base	9000		7.77		
TOM3	9/16/2020	Combined Subbase and Subgrade	7	Subbase	9000	6.81	7.28	0.47	6.93
TOM6	9/2/2021	Combined Base and Subbase	1	HMA	9000	9.47	11.98	2.51	26.54
TOM6	9/2/2021	Combined Base and Subbase	1	Base	9000	8.15	9.21	1.06	12.97
TOM6	9/2/2021	Combined Base and Subbase	1	Subbase	9000	5.65	7.92	2.27	40.26
TOM6	9/2/2021	Combined Base and Subbase	2	HMA	9000		9.85		
TOM6	9/2/2021	Combined Base and Subbase	2	Base	9000		7.62		
TOM6	9/2/2021	Combined Base and Subbase	2	Subbase	9000	5.52	6.65	1.13	20.50
TOM6	9/2/2021	Combined Base and Subbase	3	HMA	9000		11.49		
TOM6	9/2/2021	Combined Base and Subbase	3	Base	9000	7.98	8.16	0.18	2.31
TOM6	9/2/2021	Combined Base and Subbase	3	Subbase	9000	6.54	7.15	0.61	9.27
TOM6	9/2/2021	Combined Base and Subbase	4	HMA	9000		11.13		
TOM6	9/2/2021	Combined Base and Subbase	4	Base	9000		7.94		
TOM6	9/2/2021	Combined Base and Subbase	4	Subbase	9000		7.00		
TOM6	9/2/2021	Combined Base and Subbase	5	HMA	9000	7.08	9.73	2.64	37.30
TOM6	9/2/2021	Combined Base and Subbase	5	Base	9000	6.43	6.25	-0.18	2.75
TOM6	9/2/2021	Combined Base and Subbase	5	Subbase	9000	5.10	5.41	0.31	6.10
TOM6	9/2/2021	Combined Base and Subbase	6	HMA	9000	8.51	11.34	2.83	33.25

TOM6	9/2/2021	Combined Base and Subbase	6	Base	9000	7.83	7.85	0.02	0.24
TOM6	9/2/2021	Combined Base and Subbase	6	Subbase	9000	6.24	6.68	0.45	7.18
TOM6	9/2/2021	Combined Base and Subbase	7	HMA	9000	7.80			
TOM6	9/2/2021	Combined Base and Subbase	7	Base	9000	7.82			
TOM6	9/2/2021	Combined Base and Subbase	7	Subbase	9000	6.68			
TOM6	9/2/2021	Combined Subbase and Subgrade	1	HMA	9000	9.47	11.95	2.48	26.17
TOM6	9/2/2021	Combined Subbase and Subgrade	1	Base	9000	8.15	9.03	0.88	10.79
TOM6	9/2/2021	Combined Subbase and Subgrade	1	Subbase	9000	5.65	8.29	2.64	46.80
TOM6	9/2/2021	Combined Subbase and Subgrade	2	HMA	9000		9.75		
TOM6	9/2/2021	Combined Subbase and Subgrade	2	Base	9000		7.30		
TOM6	9/2/2021	Combined Subbase and Subgrade	2	Subbase	9000	5.52	7.01	1.50	27.11
TOM6	9/2/2021	Combined Subbase and Subgrade	3	HMA	9000		11.44		
TOM6	9/2/2021	Combined Subbase and Subgrade	3	Base	9000	7.98	7.80	-0.18	2.24
TOM6	9/2/2021	Combined Subbase and Subgrade	3	Subbase	9000	6.54	7.60	1.05	16.11
TOM6	9/2/2021	Combined Subbase and Subgrade	4	HMA	9000		11.06		
TOM6	9/2/2021	Combined Subbase and Subgrade	4	Base	9000		7.71		
TOM6	9/2/2021	Combined Subbase and Subgrade	4	Subbase	9000		7.50		
TOM6	9/2/2021	Combined Subbase and Subgrade	5	HMA	9000	7.08	9.78	2.69	38.02
TOM6	9/2/2021	Combined Subbase and Subgrade	5	Base	9000	6.43	6.10	-0.32	5.02
TOM6	9/2/2021	Combined Subbase and Subgrade	5	Subbase	9000	5.10	5.83	0.73	14.29
TOM6	9/2/2021	Combined Subbase and Subgrade	6	HMA	9000	8.51	11.56	3.05	35.87
TOM6	9/2/2021	Combined Subbase and Subgrade	6	Base	9000	7.83	7.72	-0.11	1.40
TOM6	9/2/2021	Combined Subbase and Subgrade	6	Subbase	9000	6.24	7.41	1.17	18.81
TOM6	9/2/2021	Combined Subbase and Subgrade	7	HMA	9000	7.80			
TOM6	9/2/2021	Combined Subbase and Subgrade	7	Base	9000	7.82			
TOM6	9/2/2021	Combined Subbase and Subgrade	7	Subbase	9000	6.68			
TOM2	12/19/2020	Combined Subbase and Subgrade	1	HMA	6000	3.42	3.30	-0.12	3.47
TOM2	12/19/2020	Combined Subbase and Subgrade	1	Base	6000	3.24	3.17	-0.07	2.07
TOM2	12/19/2020	Combined Subbase and Subgrade	1	Subbase	6000	2.58	2.72	0.14	5.24
TOM2	12/19/2020	Combined Subbase and Subgrade	1	HMA	9000	5.30	5.91	0.60	11.39
TOM2	12/19/2020	Combined Subbase and Subgrade	1	Base	9000	5.05	5.28	0.23	4.51
TOM2	12/19/2020	Combined Subbase and Subgrade	1	Subbase	9000	3.99	5.08	1.09	27.35
TOM2	12/19/2020	Combined Subbase and Subgrade	1	HMA	12000	7.23	8.06	0.83	11.47
TOM2	12/19/2020	Combined Subbase and Subgrade	1	Base	12000	6.88	7.17	0.29	4.18
TOM2	12/19/2020	Combined Subbase and Subgrade	1	Subbase	12000	5.44	6.89	1.45	26.74
TOM2	12/19/2020	Combined Subbase and Subgrade	2	HMA	6000	3.90	4.29	0.39	9.96

TOM2	12/19/2020	Combined Subbase and Subgrade	2	Base	6000	3.53	3.82	0.29	8.24
TOM2	12/19/2020	Combined Subbase and Subgrade	2	Subbase	6000	2.88	3.45	0.57	19.80
TOM2	12/19/2020	Combined Subbase and Subgrade	2	HMA	9000	5.97	6.89	0.92	15.46
TOM2	12/19/2020	Combined Subbase and Subgrade	2	Base	9000	5.50	6.09	0.59	10.76
TOM2	12/19/2020	Combined Subbase and Subgrade	2	Subbase	9000	4.51	5.77	1.26	27.88
TOM2	12/19/2020	Combined Subbase and Subgrade	2	HMA	12000	7.84	8.96	1.12	14.32
TOM2	12/19/2020	Combined Subbase and Subgrade	2	Base	12000	7.31	7.99	0.68	9.26
TOM2	12/19/2020	Combined Subbase and Subgrade	2	Subbase	12000	6.08	7.55	1.47	24.20
TOM2	12/19/2020	Combined Subbase and Subgrade	3	HMA	6000		4.01		
TOM2	12/19/2020	Combined Subbase and Subgrade	3	Base	6000	3.27	3.54	0.27	8.31
TOM2	12/19/2020	Combined Subbase and Subgrade	3	Subbase	6000	2.83	3.39	0.55	19.54
TOM2	12/19/2020	Combined Subbase and Subgrade	3	HMA	9000		6.14		
TOM2	12/19/2020	Combined Subbase and Subgrade	3	Base	9000	5.07	5.49	0.42	8.21
TOM2	12/19/2020	Combined Subbase and Subgrade	3	Subbase	9000	4.46	5.26	0.80	18.00
TOM2	12/19/2020	Combined Subbase and Subgrade	3	HMA	12000	7.45	8.22	0.77	10.35
TOM2	12/19/2020	Combined Subbase and Subgrade	3	Base	12000	6.80	7.32	0.52	7.66
TOM2	12/19/2020	Combined Subbase and Subgrade	3	Subbase	12000	6.05	7.02	0.97	16.02
TOM2	12/19/2020	Combined Subbase and Subgrade	4	HMA	6000	2.83	3.53	0.70	24.62
TOM2	12/19/2020	Combined Subbase and Subgrade	4	Base	6000	2.72	3.20	0.48	17.61
TOM2	12/19/2020	Combined Subbase and Subgrade	4	Subbase	6000	2.38	3.08	0.69	29.06
TOM2	12/19/2020	Combined Subbase and Subgrade	4	HMA	9000	4.37	5.16	0.79	18.03
TOM2	12/19/2020	Combined Subbase and Subgrade	4	Base	9000	4.22	4.74	0.52	12.31
TOM2	12/19/2020	Combined Subbase and Subgrade	4	Subbase	9000	3.69	4.56	0.87	23.66
TOM2	12/19/2020	Combined Subbase and Subgrade	4	HMA	12000	5.88	7.32	1.44	24.46
TOM2	12/19/2020	Combined Subbase and Subgrade	4	Base	12000	5.67	6.72	1.05	18.46
TOM2	12/19/2020	Combined Subbase and Subgrade	4	Subbase	12000	5.00	6.38	1.38	27.68
TOM2	12/19/2020	Combined Subbase and Subgrade	5	HMA	6000	3.05	3.33	0.27	8.95
TOM2	12/19/2020	Combined Subbase and Subgrade	5	Base	6000	2.79	2.83	0.04	1.54
TOM2	12/19/2020	Combined Subbase and Subgrade	5	Subbase	6000	2.34	2.68	0.34	14.43
TOM2	12/19/2020	Combined Subbase and Subgrade	5	HMA	9000	4.64	5.06	0.42	8.99
TOM2	12/19/2020	Combined Subbase and Subgrade	5	Base	9000	4.25	4.36	0.11	2.56
TOM2	12/19/2020	Combined Subbase and Subgrade	5	Subbase	9000	3.64	4.14	0.50	13.77
TOM2	12/19/2020	Combined Subbase and Subgrade	5	HMA	12000	6.15	6.72	0.57	9.27
TOM2	12/19/2020	Combined Subbase and Subgrade	5	Base	12000	5.64	5.79	0.15	2.61
TOM2	12/19/2020	Combined Subbase and Subgrade	5	Subbase	12000	4.86	5.50	0.64	13.15
TOM2	12/19/2020	Combined Subbase and Subgrade	6	HMA	6000	3.52	4.12	0.60	17.17

TOM2	12/19/2020	Combined Subbase and Subgrade	6	Base	6000	3.42	3.62	0.20	5.75
TOM2	12/19/2020	Combined Subbase and Subgrade	6	Subbase	6000	2.92	3.40	0.48	16.45
TOM2	12/19/2020	Combined Subbase and Subgrade	6	HMA	9000	5.49	6.45	0.96	17.57
TOM2	12/19/2020	Combined Subbase and Subgrade	6	Base	9000	5.37	5.71	0.34	6.42
TOM2	12/19/2020	Combined Subbase and Subgrade	6	Subbase	9000	4.60	5.35	0.75	16.32
TOM2	12/19/2020	Combined Subbase and Subgrade	6	HMA	12000	7.37	8.60	1.22	16.61
TOM2	12/19/2020	Combined Subbase and Subgrade	6	Base	12000	7.23	7.63	0.41	5.63
TOM2	12/19/2020	Combined Subbase and Subgrade	6	Subbase	12000	6.22	7.16	0.94	15.08
TOM2	12/19/2020	Combined Subbase and Subgrade	7	HMA	6000	3.46	4.36	0.90	26.04
TOM2	12/19/2020	Combined Subbase and Subgrade	7	Base	6000		3.81		
TOM2	12/19/2020	Combined Subbase and Subgrade	7	Subbase	6000	3.27	3.58	0.31	9.39
TOM2	12/19/2020	Combined Subbase and Subgrade	7	HMA	9000	5.29	6.79	1.51	28.48
TOM2	12/19/2020	Combined Subbase and Subgrade	7	Base	9000		5.97		
TOM2	12/19/2020	Combined Subbase and Subgrade	7	Subbase	9000	5.05	5.55	0.50	9.87
TOM2	12/19/2020	Combined Subbase and Subgrade	7	HMA	12000	7.06	8.96	1.90	26.95
TOM2	12/19/2020	Combined Subbase and Subgrade	7	Base	12000		7.92		
TOM2	12/19/2020	Combined Subbase and Subgrade	7	Subbase	12000	6.84	7.38	0.54	7.97

References

AASHTO T 307 (1999) "Standard Method of Test for Determining the Resilient Modulus of Soils and Aggregate Materials", *The American Association of State Highway and Transportation Officials*, Washington, DC.

Akram, T., Scullion, T., and Smith, R.E. (1994). "Comparing Laboratory and Backcalculated Layer Moduli on Instrumented Pavement Sections", *Nondestructive Testing of Pavements and Backcalculation of Moduli: Second Volume.* ASTM International. Pp 175-200.

American Association of State Highway and Transportation Officials. (2004) Guide for Mechanistic-Empirical Design of New and Rehabilitated Pavement Structures, Parts 1–4. NCHRP Project 1-37A Final Report. National Cooperative Highway Research Program, Washington, DC.

Appea, A., Flintsch, G.W. and Al-Qadi, I.L. (2002) "Backcalculation validation through field instrumentation", *Pavement Evaluation Conference,* Roanoke, Virginia, USA.

ASTM D7228 – 06a (2020) "Standard Test Method for Prediction of Asphalt-Bound Pavement Layer Temperatures" *American Society for Testing and Materials,* West Conshohocken, PA.

Bahrani, N., Blanc, J., Hornych, P. and Menant, F. (2020) "Alternate Method of Pavement Assessment Using Geophones and Accelerometers for Measuring the Pavement Response", *Infrastructures, 5,* no. 3: 25. https://doi.org/10.3390/infrastructures5030025.

Bentsen, R.A., Nazarian, S. and Harrison, J.A. (1989) "Reliability Testing of Seven Nondestructive Pavement Testing Devices", *Nondestructive Testing of Pavements and Backcalculation of Moduli, ASTM STP 1026,* A. J. Bush, III and G. Y. Baladi, Eds., American Society for Testing and Materials, Philadelphia, pp 41-58.

Brandt, A. and Brincker, R. (2014) "Integrating time signals in frequency domain – Comparison with time domain integration", *Measurement, 58,* pp 511-519.

Brincker, R., Lagö, T. L., Andersen, P. and Ventura, C. (2006) *Improving the Classical Geophone Sensor Element by Digital Correction.* Pinocchio Data Systems, Falkenber, Sweden.

Bush, A.J. (1987), *Development of a Pavement Evaluation Method for Low Volume Airfield Pavements,* Ph.D. Dissertation, University of Illinois, Urbana, ILL.

Chai, Y.E. (1990) *In Situ Verification of Layer Theory for Pavement Design and Rehabilitation.* Master's thesis. University of Texas at El Paso.

Chou, Y.J. and Lytton, R.L. (1991) "Accuracy and Consistency of Backcalculated Pavement Layer Moduli", *Transportation Research Record, 1293,* pp 72-85.

Duong, N., Blanc, J., Hornych, P., Menant, F., Lefeuvre, Y., and Bouveret, B. (2018) "Monitoring of pavement deflections using geophones", *International Journal of Pavement Engineering,* DOI: 10.1080/10298436.2018.1520994

Ellis, G. (2012) *Control system Design Guide: Using Your Computer to Understand and Diagnose Feedback Controllers (Fourth Edition),* Butterworth-Heinemann, https://doi.org/10.1016/B978-0-12-385920-4.15005-2

Fernando, E.G. and Liu, W. (2001) *User's Guide for the MODULUS Temperature Correction Program (MTCP).* Report No. FHWA/TX-01/1863-1. Texas Department of Transportation, Austin, TX.

Fu, G., Zhao, Y., Zhou, C., and Liu, W. (2020) "Determination of effective frequency range excited by falling weight deflectometer loading history for asphalt pavement. *Construction and Building Materials, 235*, 117792.

Graves, R.C. and Drnevich, V.P. (1991) "Calculating Pavement Deflections with Velocity Transducers", *Transportation Research Record, 1293,* pp 12-23.

Guzina, B.B. and Osburn, R. (2002) "An Effective Tool for Enhancing the Static Backcalculation of Pavement Moduli", *81st Annual Meeting of Transportation Research Board,* Washington, D.C., January 2002.

Horak, E., and Emery, S. (2006). "Falling Weight Deflectometer Bowl Parameters as analysis tool for pavement structural evaluations", *22nd Australian Road Research Board (ARRB) International Conference*. Brisbane, Australia.

Joshi, R.V. (2010) *Field Performance of Geogrid Reinforced Low-Volume Pavements,* Master's Thesis, University of Texas at Austin.

Liu, W. and Scullion, T. (2001) *MODULUS 6.0 for Windows: User's Manual,* Report No. FHWA/TX-02/1869-3. Texas Department of Transportation, Austin, TX.

Liu, W. and Scullion, T. (2011) *Flexible Pavement Design System FPS 21: User's Manual.* Texas Department of Transporation, Austin, TX.

Magnuson, A.H. (1988) *Dynamic Analysis of Falling-Weight Deflectometer Data.* Report No. TX-89/1175-1. Texas State Department of Highways and Public Transportation, Austin, TX.

Michalak, C.H. and Scullion, T. (1995) *MODULUS 5.0: User's Manual.* Report No. TX-96/1787-1. Texas Department of Transportation, Austin, TX.

Nazarian, S. and Bush, A.J. (1989) "Determination of Deflection of Pavement Systems using Velocity Transducers", *Transportation Research Record, 1227,* pp 147-158.

Nazarian, S. and Chai, Y.E. (1992) "Comparison of Theoretical and In Situ Behaviors of a Flexible Pavement Section", *Transportation Research Record, 1377,* pp 172-182.

Rohde, G.T. and Scullion, T. (1990) *Modulus 4.0: Expansion and Validation of the MODULUS Backcalculation System,* Report No. FHWA/TX/91/1123-3. Texas State Department of Highways and Public Transportation, Austin, TX.

Sankaranarayanan (2021), personal communication.

Sargand, S.M., Vega-Posada, C.A., Arboleda-Monsalve, L.G. (2013) "Long term performance of existing asphalt concrete pavement sections", *Revista Facultad de Ingenieria Journal* 66: 56-69.

Schmalzer, P.N. (2006) *LTTP Manual for Falling Weight Deflectometer Measurements, Version 4.1*. Report No. FHWA/HRT/06/132. Federal Highway Administration, Office of Infrastructure Research and Development, McLean, VA.

Scullion, T., Briggs, R.C. and Lytton, R.L. (1989) "Using the Multidepth Deflectometer to Verify Modulus Backcalculation Procedures," *Nondestructive Testing of Pavements and Backcalculation of Moduli, ASTM STP 1026,* A. J. Bush III and G. Y. Baladi, Eds., American Society for Testing and Materials, Philadelphia, pp 90-101.

Scullion, T., Uzan, J. and Paredes, M. (1990) "MODULUS: A Microcomputer-Based Backcalculation System", *Transportation Research Record, 1260,* pp 180-191.

Smith, S.W. (1997) *The Scientist and Engineer's Guide to Digital Signal Processing,* California Technical Publishing, USA.

Tandon, V. and Nazarian, S. (1990) *Comprehensive Evaluation of Sensors Used for Pavement Monitoring.* Report No. 913-1F. Texas State Department of Highways and Public Transportation, Austin, TX